A Racetrack Memory Based on Exchange Bias

Ioan Polenciuc

PhD

University of York

Physics

November 2016

Abstract

This thesis describes preliminary studies for a new type of computer memory, racetrack memory. Racetrack memory was initially proposed by scientists at IBM. Data in racetrack memory is stored in domains within ferromagnetic nanowires which are separated by domain walls. The data is moved in the wires by moving the domain walls. Control over the movement of domain walls was initially attempted via use of notches cut into the wires, but these were not only expensive and difficult to fabricate but also proved to be unreliable.

The method for pinning domain walls described in this thesis uses antiferromagnetic wires grown perpendicular to ferromagnetic wires so that exchange bias is induced at the crossing points. Exchange bias occurs when an antiferromagnet is in contact with a ferromagnet. When the structure is cooled in an applied field from near the Néel temperature of the antiferromagnet, the hysteresis loop shifts along the field axis resulting in pinning of the ferromagnetic layer.

Multiple ferromagnetic materials were considered for the ferromagnetic layer. Initially unpinned ferromagnetic films were grown and characterised. Exchange biased films were then grown in configurations where the antiferromagnetic layer was either under or above the ferromagnetic layer but showed no major differences in the exchange bias.

Ferromagnetic wires were patterned on Si substrates using e-beam and photolithography. Coercivity of the wires was measured along the length of the wires. Exchange biased wires in both top and bottom pin configurations were fabricated afterwards using the same methods and characterised using the same technique as the unbiased wires. The comparison between the biased and unbiased wires showed that domain walls can be pinned in nanowires using exchange bias. The top bias configuration showed a maximum value for pinning of about 55 Oe which is comparable to that initially reported in notched systems.

Contents

List of Figures

List of Tables

Acknowledgement

I would like to dedicate this thesis to my grandfather and grandmother as without their love, patience, help and guidance I would have never made it so far in life. I would also like to thank my family for their support and help, with special thanks to my father, mother and brother, as well as my uncles Gabi and Ana-Maria.

I could only wish to have had the ears to listen to all the precious information my supervisors Prof. Kevin O'Grady, Prof. Atsufumi Hirohata and Dr. Gonzalo Vallejo-Fernandez have thrown at me during the years.

A huge thank you goes to Teodor and Sergiu who have travelled on similar paths in their careers and who have been by my side in all the good and bad moments. Adi and Razvan, I can never thank you enough for being like brothers to me and the best friends anyone can ask for. Tadas, thank you! You are something else. You have taught me many important things they do not teach you in schools and been a true friend.

To my fellow office students, it has been a pleasure! Thank you all for the good and bad times, Kelvin, Ben, John, Will, Joe, Jason, Chris, Rob and all the rest who I forgot to mention by name. Susan, you took an interest in all our lives and always made sure we have sweets for the holidays so I would like to use this occasion to thank you!

Declaration

I declare that the work presented in this thesis is based purely on my own research, unless otherwise stated, and has not been submitted for a degree in either this or any other university.

1. Introduction

This thesis presents proof of concept for a new type of computer memory, racetrack memory [1,2]. Racetrack memory has great potential to change the architecture of computers as it promises to match and exceed current hard drive storage capacities of 1 Tb/in^2 [3] and perform at frequencies matching those of current random access memories of 1-3 GHz, as well as being non-volatile [4] leading to a much simpler architecture for computers.

Computers nowadays use different types of memories for different purposes. At the time this thesis was written the result of the compromise between storage capacity and cost was the hard disk drive but this came at a great cost in speed performance. The majority of the digital data nowadays (the internet) is stored on hard disks in storage farms and in personal computers. However, hard disks are intrinsically slow (≤6 Gb/s) because the disks can rotate at only up to 15,000 RPM [5] for what are power consumption, mechanical stability and heating at the air bearing surface reasons. Another reason why it takes up to 10 ms to read a bit of data is the movement of the read/write head. In addition, in hard disks where the head is not in contact with the media this also creates reliability issues due to “head crashes” which induce data loss. Also, in the 10 ms the processor can make up to 20 million operations [4].

Another compromise between storage capacity, speed and cost is the static or dynamic random access memory which operates at frequencies of the order of 2 GHz. The read/write times are of the order of 100 ns but the price per MB is at least 200 times larger than in a hard disk drive. The greatest disadvantage of this type of random access memory is that they are volatile and a loss of power would mean a loss of data.

Flash memory is used in portable electronic devices but they are slow (≤120 Mb/s) and have limited lifetimes of typically 10,000 write operations because of memory cell degradation when writing data, although it has been shown that it can withstand up to 100,000,000 cycles [6]. Data in flash memory is rewritten periodically in order to ensure even wear of the bits and operating systems actually ignore degraded bits.

Flash memory stores data in flash transistors. Traditional transistors switch off with the power and they are unsuitable for non-volatile memory. Flash transistors are like FET transistors but have two gates instead of one separated by an insulating oxide layer. They are called floating and control gates and are shown in figure 1.1. By applying a voltage to the "wordline" the transistor is in an open state and it allows electrons to flow from source to drain. Some electrons tunnel through the insulating layer polarising the floating gate. Because of the presence of the insulating layer the gate will remain polarised after power is switched off making this type of transistor useable as a non-volatile memory.

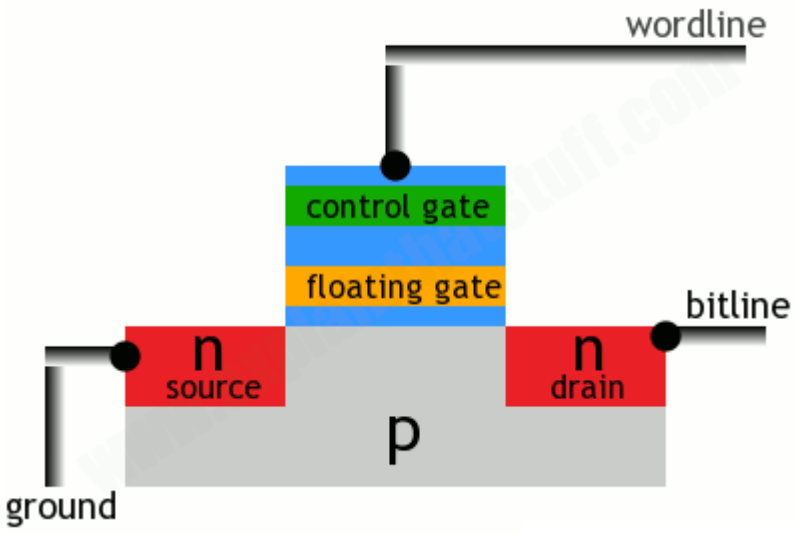

Figure 1.1 Schematic diagram of a flash transistor [7].

Because the cost of flash memory is low it is still used for applications where data is not changed often and is suitable for portable devices where weight and battery life have a higher priority than performance. A schematic diagram of the computer memory hierarchy is shown in figure 1.2.

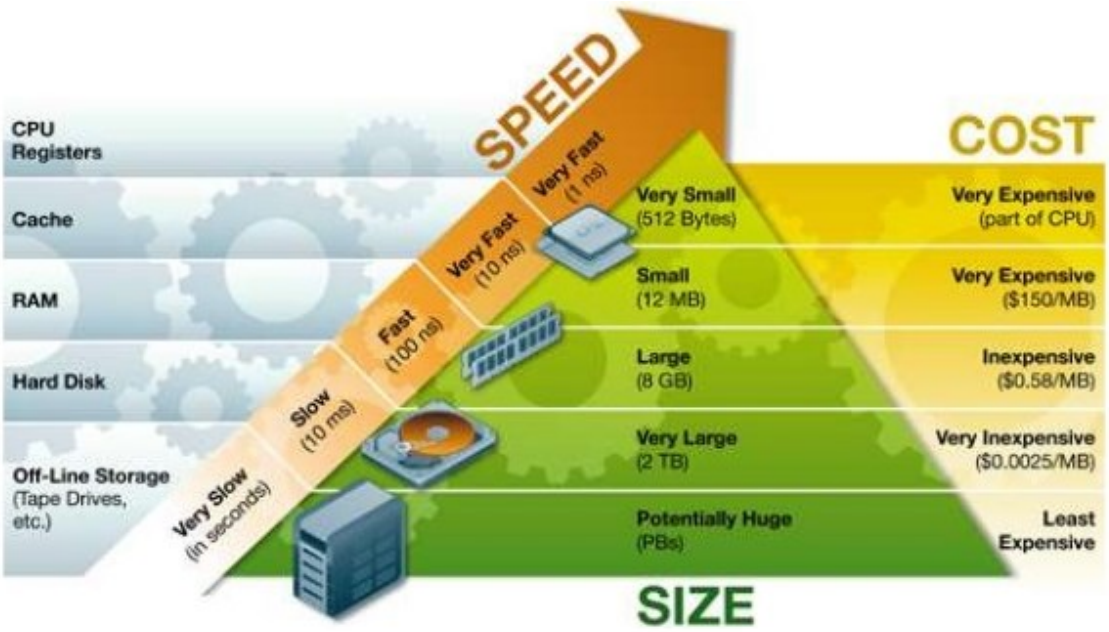

Figure 1.2 Computer memory hierarchy [8].

Bits in racetrack memory consist of magnetised regions in nanowires. Unlike in hard disks where the bits move past the read/write head via disk rotation, in racetrack memory the bits move inside the nanowires. One of the advantages this brings is that the read/write heads can be part of the structure of the recording media removing the necessity of an air bearing surface and all the issues this comes with in conventional hard disks. Because the movement of the bits is no longer mechanical, access times are reduced. This is due to the read/write head not being required to reposition along data tracks on the media and by eliminating the time until a certain bit on the disk passes under the head. A schematic diagram of Parkin's first racetrack memory concept is shown in figure 1.3.

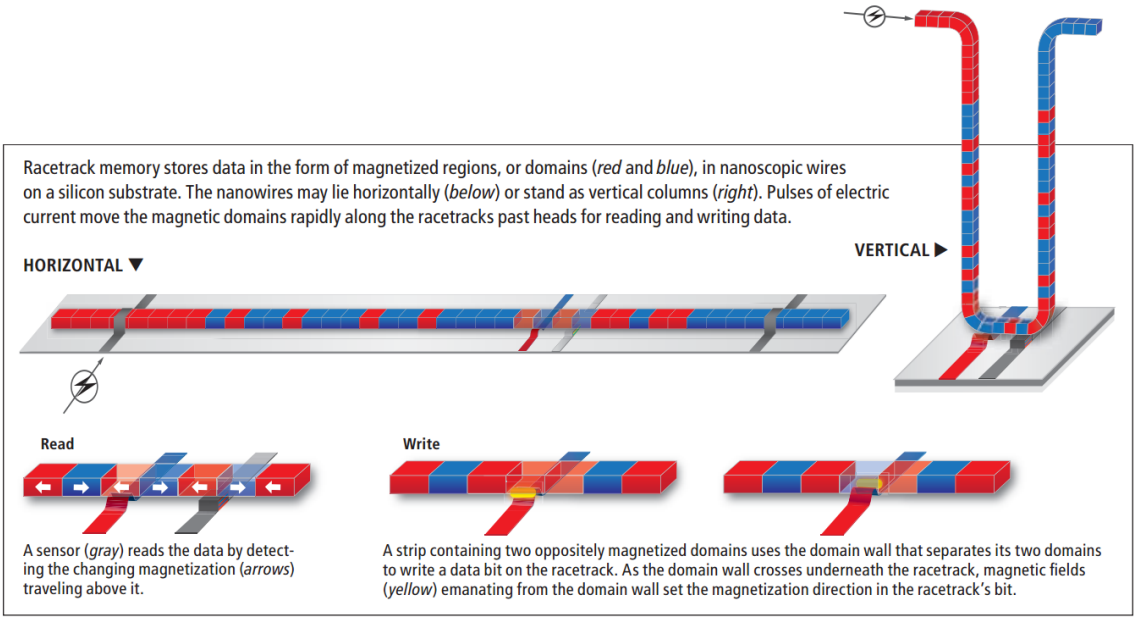

Figure 1.3 Racetrack memory as envisioned by Stuart Parkin in 2D and 3D configurations [4].

Horizontal and vertical configurations were initially suggested, but studies were carried out only on the horizontal racetrack memory. The vertical configuration has a complex structure and is not only difficult to fabricate, but the demagnetising fields at the corners may make it unusable. The bits were proposed to be moved inside the racetrack via magnetic fields [2] or via electric current [1,9]. The first issue to arise is reliability because bits may move with different velocities and they could recombine and data could be lost. This is why the movement of the bits needs to be controlled very well and was initially suggested that notches cut into the wire could stop bits from moving chaotically. This is where the first prototypes failed and this is what motivates the subject of the work presented in this thesis, a controllable method of pinning the bits in racetrack memory. A more in-depth discussion on racetrack memory can be found in chapter 2.

The method for pinning bits, or domain walls which are the regions separating the bits which is presented in this thesis makes use of a discovery made in 1956 by Meiklejohn and Bean [10]. They realised that

when cooling Co particles which had a CoO shell in a strong field down to 77 K the measured hysteresis loop was seen to shift and exhibited an increase in coercivity. This was due to the ferromagnetic core of the particles (Co) coupled to the antiferromagnetic shell (CoO). Initially, exchange bias was of fundamental interest [10-16]. However, Giant Magneto Resistance (GMR) which was discovered separately by Grünberg and Fert in 1988 [17-19] made use of exchange bias and since became of technological interest. As of 1998 it is used in hard disk read heads for pinning the ferromagnetic reference layer [20]. The first result of Meiklejohn and Bean is shown in figure 1.4.

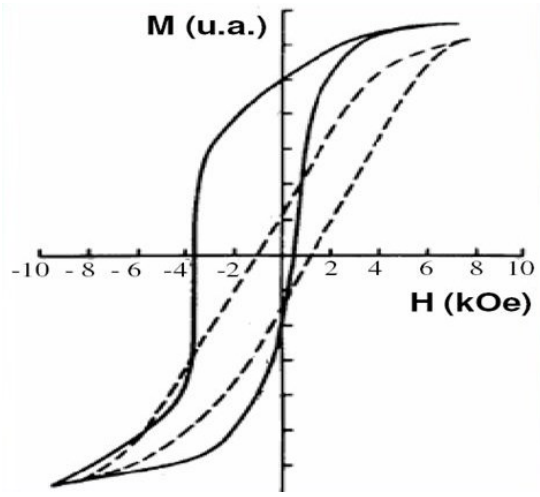

Figure 1.4 The original result of Meiklejohn and Bean showing the hysteresis loop for the Co particles before (dashed line) and after cooling in field to 77 K (solid line) [10].

Another contender for doing both the job of the hard disk drive and of the conventional random access memory is the magnetic random access memory or MRAM. This was initially conceived as a means to store data for military applications because it could not be damaged by electromagnetic radiation which was an issue for memories which stored data via electric charge. MRAM uses the magnetic dipole moment of electrons instead of the electric charges conventionally used by DRAM (dynamic RAM). An important advantage of MRAM in comparison to conventional random access memories is that it is non-volatile and

because of this it could significantly improve the starting time of computers as there will be no need for data to be booted. In 2011, when solutions for racetrack memory were sought, MRAM chips had a density of 88 Gb/in^2 and access times of 10 ns with a very low energy consumption of only 0.16 fJ/bit and it could operate at room temperature [21] whereas conventional DDR4 RAM dissipates approximately 40 pJ/bit [22].

The aim of the project presented in this thesis is to show an alternative method for pinning domain walls in racetrack memory which has a greater degree of control over the strength of the pin. Notches require additional processes for fabricating which make the fabrication more expensive and time consuming and they have shown reliability issues [1]. Exchange bias domain wall pins were fabricated and the strength of the pins and their reliability was investigated. Control of pinning strength was shown to depend on the size of the pin, exchange bias stack configuration and direction of the exchange bias.

1.2 Units

The cgs units are used for the results and all equations shown in this study. These units are widely used in the majority of the applied magnetism community. Most of the work by research groups in the field and magnetic recording industry are also presented in cgs units.

2. Racetrack Memory

2.1. Solid State Magnetic Memories

With the advancement of technology, storage requirements have increased in size and diversity. Whether it was because man needed data storage in outer space or down on Earth, data storage is under constant development. A full historical description of the progress of data storage or even magnetic storage alone can be found in the literature [3,23,24].

The first hard-disk drive (HDD) was invented in 1956. At the time the hard disk could store 5 MB of data and access it in 600 ms. Nowadays, HDDs can store TBs and have access times of the order of 1 ms. The size of hard drives has also decreased drastically from tens of 24 inch disks written on both sides to single 2.5 inch disks written on only one side [24].

Although the storage capacities of HDDs keep growing, their access speeds are slowly reaching their maximum limit because of the moving parts. The alternative is a solid-state drive (SSD), with no moving parts and non-volatile memory. SSDs have many advantages over HDDs like less energy consumption, less heat dissipation and are much quieter. Most of the SSD drives use NAND non-volatile flash memory or, the more advanced ones, use DRAM with back-up power [25,26].

Because of the great progress and exploitation of giant magnetoresistance (GMR) the first MRAM (magnetic random access memory) products were shipped in 2006 [27]. GMR will be discussed in further detail in section 2.2. Since 2006 when it was first introduced on the market, MRAM has evolved considerably becoming a potent

candidate for replacing both hard drives and RAM memories in computers [28]. A schematic diagram of an early longitudinal MRAM chip is shown in figure 2.1 [29]. There are many ideas in order to increase the performances of these devices. The one idea that needs mentioning is replacing the free layer with a track containing multiple free layers so that a unit cell will store more than one bit [30,31]. This idea is derived from another type of solid state memory, the racetrack memory (RM) which will be further discussed in the following sections.

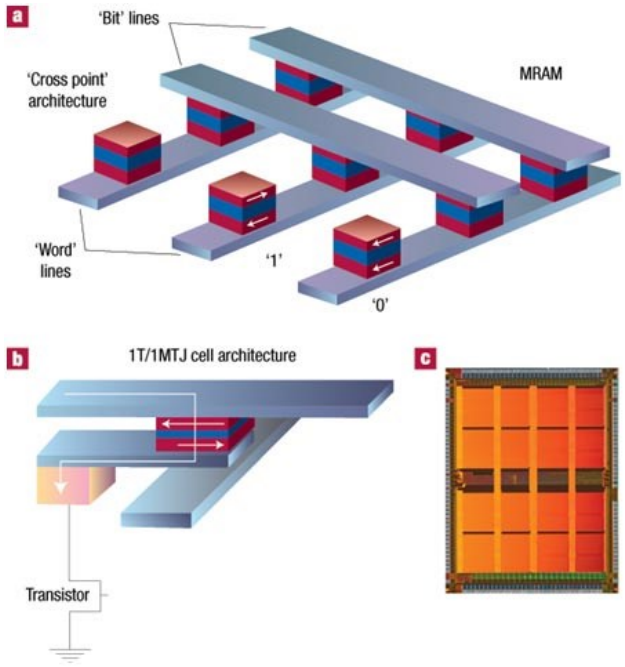

Figure 2.1 Schematic of MRAM cells (a,b) and chip [29].

2.2. GMR and TMR

In 2007 the Nobel Prize in Physics was awarded to professors Peter Grünberg [18] and Albert Fert [19] for the discovery of giant magnetoresistance (GMR). GMR is due to the spin-dependent scattering of the current carrying electrons in the host material. In ferromagnetic transition metals, spin-dependent scattering occurs because of the

number of unoccupied states in the d bands. This reduces the mean free path of the electrons. Also, a different density of states arises at the Fermi surface which leads to different scattering probabilities of spin-up and spin-down electrons, the scattering probability being greatest for the minority electrons. The spin-up and spin-down electrons can then be considered as two independent channels, according to Mott's two-current model [32].

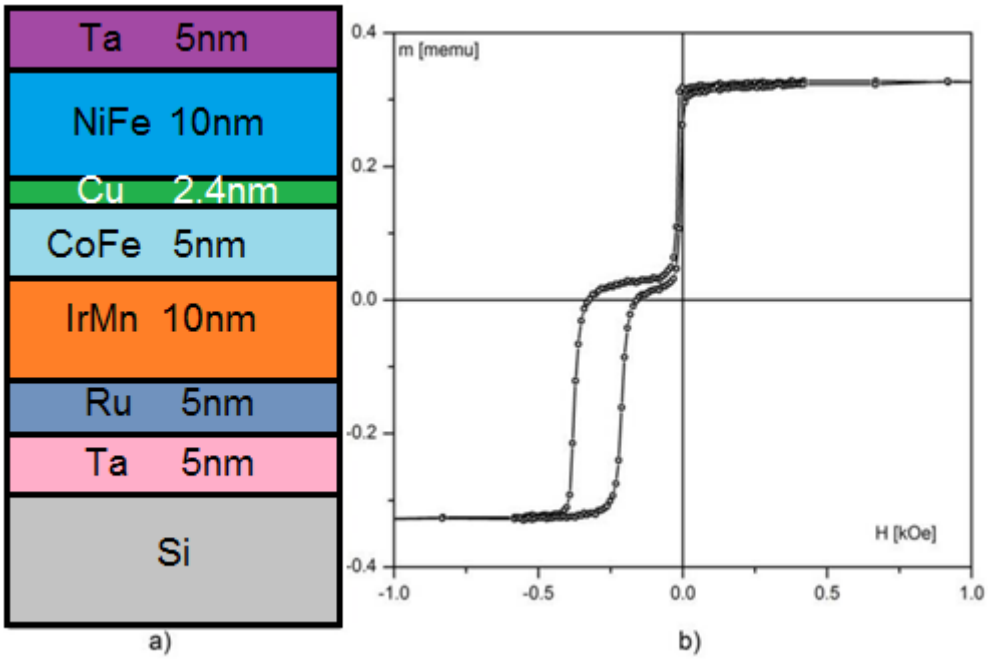

Figure 2.2 Schematic of a spin valve (a) with the corresponding hysteresis loop (b) [33].

The simplest structure where GMR can be observed is a trilayer consisting of a layer of a nonmagnetic metal sandwiched between two magnetic layers. A schematic diagram of such a stack is shown in figure 2.2 along with the characteristic layer thicknesses. It is of great importance that the electrons preserve the spin polarisation while they pass through the spacer layer hence the thickness of the spacer layer should be smaller than or of the order of the mean free path, typically 1-3 nm [34].

The GMR stack can be easily modelled using a resistor network as displayed in figure 2.3 [17]. In the first case the spin-down electrons are scattered by the F layers allowing for a low resistance in the path of the spin-up electrons. As a consequence, the current passing the junction will be spin-up polarised. In the second case the first layer scatters the spin-down electrons and the second layer scatters the ones with spin-down, both spin-up and spin-down electrons exhibiting high resistance through the structure. The variation of the resistance from the parallel state to the antiparallel state is given by equation 2.1. GMR is the state when the magnetisation of the F layers are oriented opposite to each other.

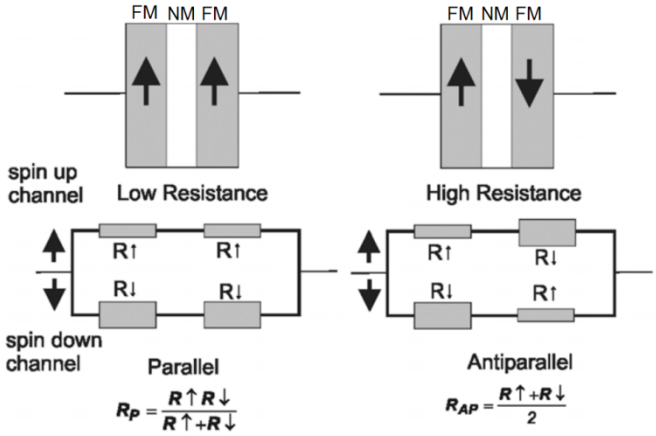

Figure 2.3 Schematic representation of a GMR stack and the equivalent resistor network [17].

$$\frac{\Delta R}{R} = \frac{R_{AP} - R_P}{R_P} = \frac{(R\downarrow - R\uparrow)^2}{4R\downarrow R\uparrow} \tag{2.1}$$

The relative orientation of the magnetisation in the two F layers depends on the purpose of the spin-valve. The change in resistance or the GMR ratio is proportional to the dot product of the magnetisation vectors of the two layers, given by equation 2.2.

$$\frac{\Delta R}{R} \propto \overrightarrow{M_1} \cdot \overrightarrow{M_2} \tag{2.2}$$

Since the relative variation of the resistance also depends on the cosine of the angle between the magnetisation vectors, the optimum relative orientation for the magnetisation vectors is perpendicular to each other. This is because the slope of the cosine function varies approximately linearly at 90°, so the variation in resistance is approximately linear.

There are several ways of controlling the relative orientation of the F layers for obtaining a GMR effect. The AF coupling between the F layers is dependent on the separation between them due to the exchange coupling discussed in section 4.2. The tuning of the F layer separation was shown by Parkin [35] and is discussed in section 4.2.2. Another possibility is to use hard and soft magnetic materials. When both are saturated, their alignment will be parallel, but as the magnetic field is reversed the softer material will switch at a lower field allowing for antiparallel alignment. A third option is to exchange bias one of the layers (figure 2.2). Exchange bias occurs when a F is in intimate contact with an AF. When field cooled nominally from near the Néel temperature of the AF the hysteresis loop shifts on the field axis, pinning the F layer [13]. This effect is discussed in chapter 4. Due to one layer coupling with an F layer, a large switching field for the two layers is possible. The GMR structure obtained by pinning one of the layers with exchange bias has led to the development of the spin valve (figure 2.2).

Various combinations of materials are suitable for obtaining suitable GMR ratios of more than 10% [34,36]. The first studies of Grünberg and Fert were done on Fe(12 nm)/Cr(1 nm)/Fe(12 nm) and three Fe/Cr multilayers, respectively [18,19]. Both of the results were obtained on GaAs substrates but with different orientations. As mentioned previously, spin-dependent scattering is due to the band structure. Moreover, it is dependent on the match of the band

structures at the ferromagnet/nonferromagnet interface. For instance, the Fe/Cr system used by Grünberg and Fert has good band matching for the spin-down and a poor match for the spin-up band [17]. Systems of Co/Cu or Ni/Cu have a mirror match to the one in Fe/Cr. A GMR ratio of $\Delta R/R = 65\%$ was reported by Parkin in Cu/Co multilayers at room temperature in 1991 [35].

A similar effect to GMR can be obtained if instead of a nonmagnetic interlayer an insulator is used. Classical electron transport cannot occur through the layer, but if its thickness is engineered to a few atomic layers then quantum mechanical tunnelling can occur [37-39]. GMR stimulated the interest in magnetoresistance so greater interest was exhibited in tunnelling magnetoresistance (TMR). TMR reported values of $\Delta R/R = 14\%$ but at low temperatures at its beginning [37] but has reached values of 200% [40,41]. This was achieved by a high degree of crystallinity of an epitaxially grown MgO barrier. The main application of TMR is within read heads of hard drives and it was introduced in products in 2004. This has improved the areal density of hard disks by 400% from 25 to 100 Gbit/in^2. This was achieved by using an Al_2O_3 barrier and more recently up to 1 Tbit/in^2 with the use of MgO barriers [42] with typical TMR ratios of 100% and RA≈1 Ωμm^2 [34,36].

2.3. Background of Racetrack Memory

Hard drives have been the “go to” solution for storing data for more than 50 years. During this time the size of a bit has decreased by 9 orders of magnitude. The bit on a hard drive is nowadays so small (20 nm) that fundamental limits are being reached in all aspects of locating, reading and writing a bit. Improvements in hard drive technologies have slowed down considerably in recent years leaving room for the

development of other technologies like MRAM and racetrack memory (RM).

RM is a solid-state spintronic device. One unique feature of RM is its capability to be developed in three dimensions, unlike hard drives and MRAM [43] which are 2D. The principle of racetrack memory is illustrated in figure 2.4. Data is stored in a series of domain walls (DWs) in 20 nm thick $Ni_{81}Fe_{19}$ nanowires that are 200 nm wide and between 6 and 15 μm long [44]. Its operation is based on the fact that the DWs can be moved through the nanowire by the passage of a current. Spin angular momentum is transferred by the moving charges that are the current from the conduction electrons to the magnetic moments of the DW. The transfer results in DW displacement. This has been shown by Parkin *et al.* in soft permalloy nanowires [45]. The angular momentum transfer has been reported to be almost perfect [46]. It is 'almost' perfect because some of the angular momentum is lost within the lattice through damping.

Spin polarisation in permalloy is approximately 70% [47]. It is determined by the scattering of the conduction electrons with regards to their spin. The DWs move in the same direction as the electrons, so opposite to the direction of the current. For densities of 10^8 A/cm^2 the velocities of the DWs reach 100 m/s [45]. The experiments presented in Parkin's 2008 paper also reported that the DWs in the permalloy wires change their size due to the torques transferred by the electrons and the lack of crystalline anisotropy of the material making it very difficult to control. Parkin's permalloy nanowires represented the first version of racetrack memory.

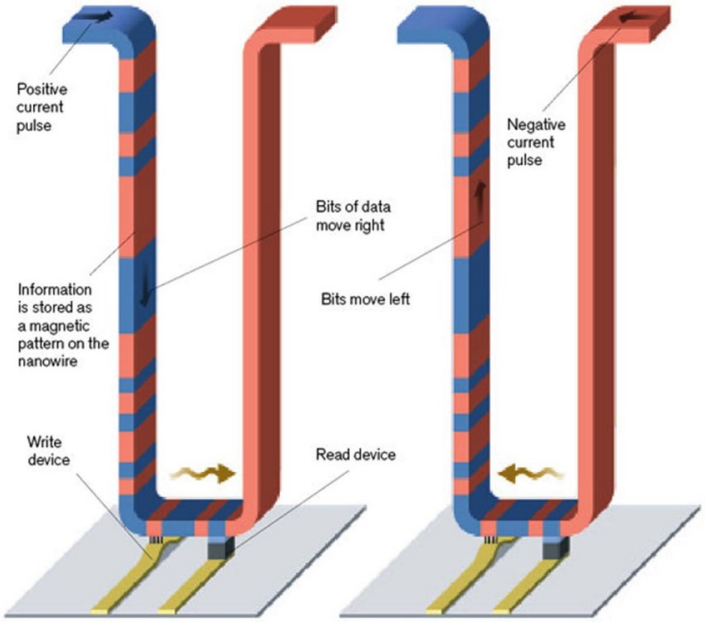

Figure 2.4 Schematic diagram of a proposed racetrack memory [44].

The second version of RM addressed the issue of the DWs changing their size (360 nm wide, 3.2 μm domains) when electrons transferred the torque to the DW. The wires were fabricated from a multilayer of $[Co(0.3\ nm)/Ni(0.9\ nm)]_4/Co(0.3\ nm)$ which enhanced the perpendicular anisotropy [48,49]. The DWs were much narrower (340-360 nm) than in the longitudinal case, they did not stretch but they moved with a similar velocity and in the same direction as in the previous version.

The third version of RM appeared in 2011. Miron *et al* reported that DWs can move much faster in ultrathin cobalt layers deposited on a platinum layer [50]. The wires were 500 nm wide and were a multilayer of $Pt(3\ nm)/Co(0.6\ nm)/AlO_x(2\ nm)$. The DWs moved in the direction of the current and it was due to very complex mechanisms derived from the spin-orbit coupling (the Dzialoshinskii-Moriya interaction or DMI). For similar current densities to those used in the previous versions (10^8 A/cm^2) the DWs had velocities up to 350 m/s. Another difference between this version and the ones before is that the

movement of DWs occurs due to a chiral spin torque, unlike volume spin torques [50,51].

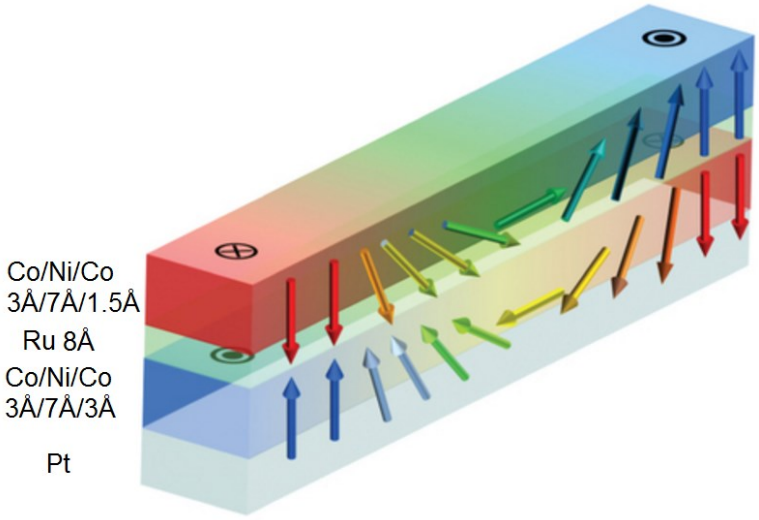

Figure 2.5 Schematic illustrations of spin configurations in SAF racetrack memory [52].

Racetrack Memory 4.0, as it was named by Parkin, is the latest version of RM. It was reported that in RM 4.0 DWs travel with velocities of 750 m/s, three times faster than the previous version (~350 m/s) [52]. For racetrack memory to have high density, the DWs need to be closely packed, but their fringing fields limit the achievable density due to dipolar coupling. The fringing fields are eliminated by using a synthetic AF structure consisting of two Co/Ni/Co trilayers separated by an ultrathin AF-coupling spacing layer (8 Å Ru) as shown in figure 2.5. "The synthetic antiferromagnet is formed from two perpendicularly magnetized sub-racetracks that are antiferromagnetically coupled via an ultrathin ruthenium layer" [43]. The velocity of 750 m/s was achieved in wires consisting of layers of Co(0.3 nm)/Ni(0.7 nm)/Co(0.15 nm)/ Ru(0.8 nm)/Co(0.3 nm)/Ni(0.7 nm)/Co(0.15 nm).

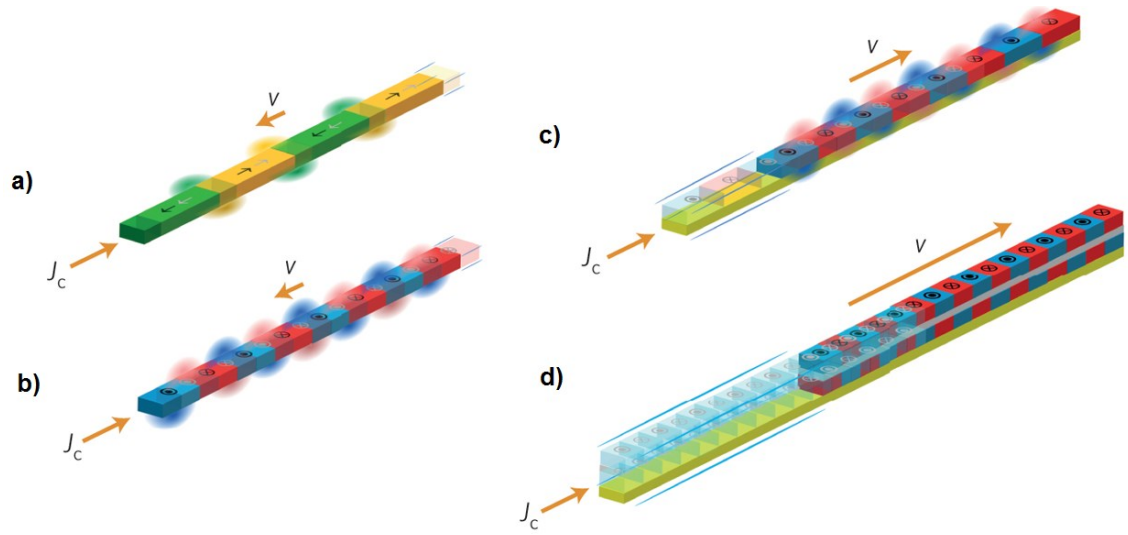

Figure 2.6 Racetrack memory a) v1.0 – longitudinal; b) v2.0 – perpendicular; c) v3.0 – ultrathin Co; d) v4.0 – synthetic antiferromagnet [43].

The two sub-racetracks mirror each other due to the coupling and give a net magnetization of the entire racetrack very close to zero. By tuning the thickness of the spacer layer the coupling between the two sub-lattices can be set to be ferromagnetic. It has been reported that the DWs in the antiferromagnetically coupled sub-racetracks move five times more efficiently than in the case when the coupling is ferromagnetic [52]. The same report showed that the velocity of the DWs increases the closer the net magnetisation is to zero.

Having a zero net magnetisation means the DWs can be packed closer together. The DWs also need less power to be moved. These are due to a stabilisation of the domain wall structures and to the exchange coupling torque which is proportional to the AF coupling between the two F layers [52]. The DWs are stabilised this way by forcing them to interact with the DWs in the mirrored racetrack, reducing interactions between neighbouring DWs in the same racetrack. This makes RM a viable contender for hard drives as a storage solution. If a single racetrack contained 100 DWs (or 100 bits), then the density of RM would be 100 times larger than that of MRAM. Having no moving parts

it does not suffer wear and there are no mechanisms to fail. A more detailed discussion on the principles behind RM are given below.

2.3. Basis of Racetrack Memory

Racetrack memory can be viewed as a single track from a hard drive which is extracted from the HDD platter and uncurled into a straight wire. In a HDD the bits travel underneath the read/write head due to the physical rotation of the platter. In RM the bits travel through the wire, eliminating any mechanical movement. In a HDD the bits are certain regions on the magnetic platter and they cannot intermix. For the RM the bits are DWs and because they travel through the wire and are not fixed, certain delimitations need to be introduced in the wire so that the DWs do not recombine and alter the data. To do so notches were introduced at equal intervals so that the space between two notches could only accommodate one bit. The review which presented this memory concept in 2008 also showed that when trying to move a DW over a notch, for the same energy, the DW sometimes moved to the next notch, sometimes skipped a notch and sometimes did not move at all [2].

Racetrack memory requires a track at least twice as long as the wire which can accommodate all the information to be stored. This is because the reading and writing requirements of the memory. In order to read or write data in racetrack memory the DWs need to be pushed over the read/write head, as suggested in figure 2.7. The DWs are pushed through the wires using nanosecond current pulses using spin transfer torque (STT). If the wire it passes through is magnetic and small enough, the current becomes spin polarised. When the polarised

electrons reach the DW, spin angular momentum is transferred and the resulting torque acts to move the DW. DW propagation using STT was first shown by Yamaguchi *et al* [53].

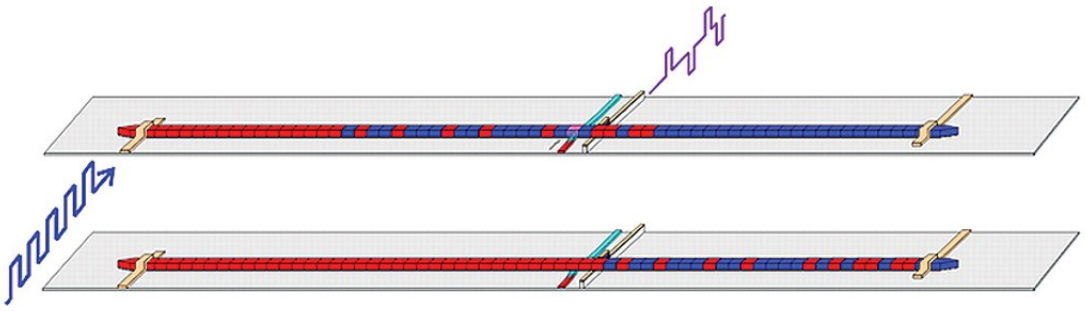

Figure 2.7 Racetrack memory with read and write elements [2].

Reading and writing of the bits in the RM is much simpler than in a HDD because of the lack of mechanical movement. This means that the read/write elements can be in contact with the RM and not floating on an air bearing surface like in a HDD. The DWs can be read using a spin valve, which is very similar to those used in HDDs [54].

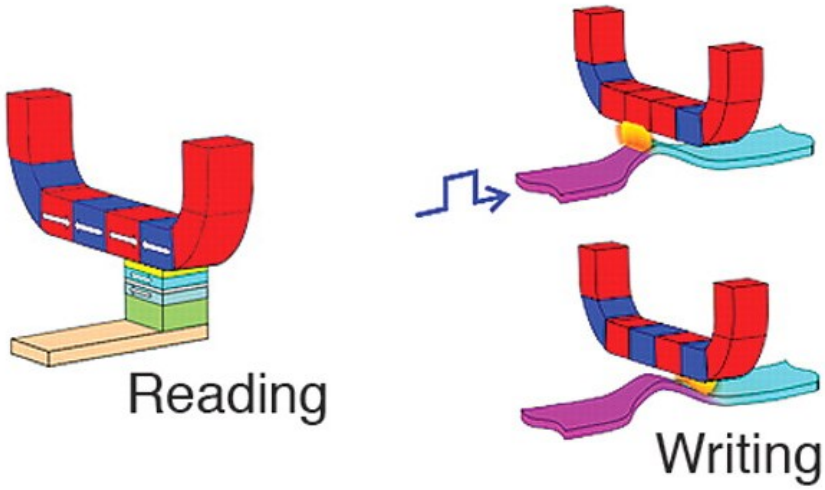

Figure 2.8 Schematic diagram of reading and writing elements for RM [2].

The writing of DWs allows for more flexibility. Fields from nearby metallic wires can be used to write new DWs, or they can be injected in the wires from nanoelements using the same STT, or they can be

written by the fringing field of another DW. Figure 2.8 shows a spin valve in contact with the racetrack for reading and a DW being written by the fringing field of another moving DW.

2.4. Exchange Bias Domain Wall Pins

A RM track is a shift register based on a nanowire. It relies on the propagation of DWs in the track for storing data. Different data states are indicated by the position of the DWs in the track, so the movement and positioning of the DWs needs to be very reliable. For RM to be functional it is important that the DWs have very well defined positions. This was attempted by geometrical factors, notches cut into the wires [2], steps created in the substrate [9], combs [55] etc. all methods to pin DWs in a certain position. Most of these methods were unreliable [1,2].

An alternative method has been suggested by Hirohata *et al* [56]. This method for pinning DWs consists of creating an exchange bias interaction between a ferromagnetic and an antiferromagnetic material. This should create a permanent pinning site with desirable strengths between 50 and 150 Oe. The pinning sites would be regions on the F wire where exchange bias was induced via the deposition of an AF. Figure 2.9 suggests a method of obtaining pinning sites by depositing AF wires perpendicular to the F nanowires [56].

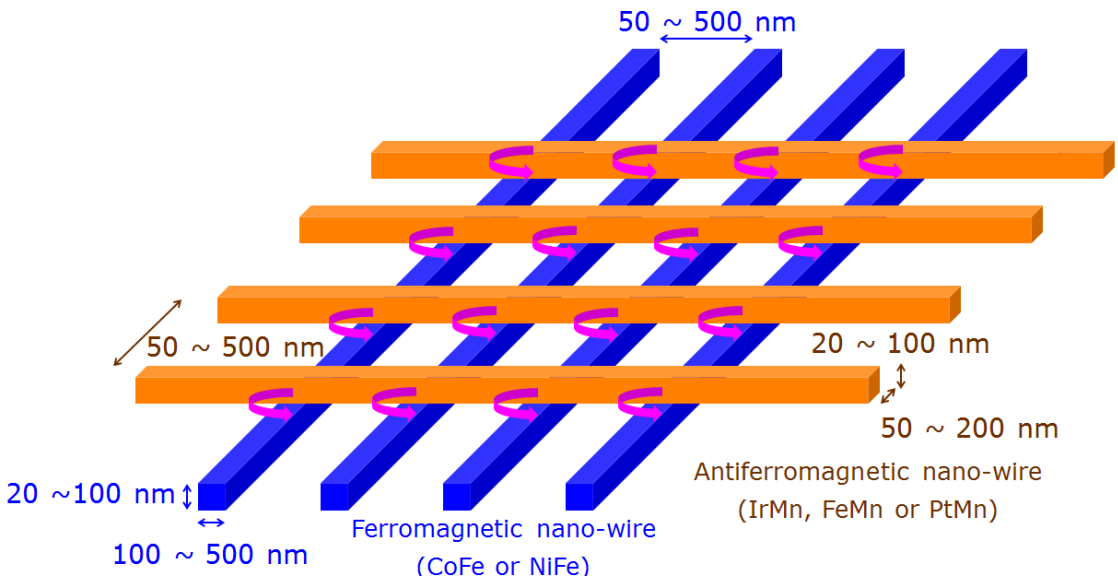

Figure 2.9 Schematic of an array of F wires (blue) perpendicular to an array of AF wires (orange).

Unlike a notch or other geometrical induced pinning sites, the exchange bias sites can be controlled via different means. The pinning strength should depend on the AF material anisotropy, the size of the pin and the thickness of the F wire. The size of the pin is the wire width. Aley et al. has shown that the anisotropy can be controlled via exchange bias [57]. This method offers a great degree of control over the pinning sites and is much easier to fabricate than other aforementioned methods.

3. Ferromagnetic Thin Films and Elements

3.1. Structure of Thin Films

Thin films are essential for solid state technology. By reducing film thickness towards the nanometre scale the microstructure of the material becomes dominant in defining its physical properties. The most important properties of magnetic thin films are the grain size, the grain size distribution, the crystallographic texture and the surface/interface roughness [57]. Thin films are combined to form multilayer structures for various applications, one of which is exchange bias, where a ferromagnetic thin film is in intimate contact with an antiferromagnetic thin film. Exchange bias is discussed in depth in chapter 4.

There are various means of growing thin films, including evaporation, molecular beam epitaxy (MBE) or sputtering. These methods are described in section 5.1. The films used in this work were grown using a particular design of sputtering machine (HiTUS) which is described in detail in section 5.1.2. HiTUS produces granular films with typical grain sizes between 4-20 nm [57]. For ferromagnetic thin films this corresponds to grains being single domains. This is important for magnetic recording applications as the single domain particles may have a large remanence and coercivity and are bistable. Growth in the HiTUS is columnar therefore the morphology is controlled by the seed layer. Hence, different layers have different impacts on the properties of the thin films [58].

3.2. Anisotropy in Thin Films

Magnetic anisotropy is one of the main factors which determine the shape of the *M-H* curve (the hysteresis loop). This dictates that the properties of a magnetic material varies with and depends on the

direction in which they are measured. There are two types of factors which influence the total anisotropy of a magnetic sample: intrinsic factors which depend on the arrangement of the atoms (crystalline anisotropy) and extrinsic factors which can be sample shape or stress that can be induced in the sample via different means (annealing, deformation, irradiation etc.).

Shape anisotropy is due to the geometry of the sample. Free poles at the surface of the sample create a demagnetising field $\boldsymbol{H_D}$ which opposes its magnetisation $\boldsymbol{M}$.

$$\boldsymbol{H_D} = -N_D \boldsymbol{M} \tag{3.1}$$

where N_D is the demagnetising factor. For example the demagnetising factor for a sphere is $N_D=4\pi$. The density of the films is unknown, however an approximate value can be estimated because of the coupling exhibited. This may very well lie around the value of 90% because of the film being polycrystalline. Polycrystalline films are not 100% dense because of the grain boundaries [59]. If the density was much lower than 90% the grains would be exchange decoupled. Film density also depends on the grain size and the grain size distribution as for smaller grains a higher proportion of the film is grain boundaries reducing the overall film density.

Samples exhibit changes in their dimensions when placed in magnetic fields. This effect is called magnetostriction. Atoms rearrange in order to minimise self-energy, changing the length of the sample along the direction of the applied field. This effect is reciprocal to the application of tensile stress which on a magnetic sample may change its magnetisation without an applied field. However, shape and stress anisotropy are not dominant in the films used in this work, the only significant contribution arising from the magnetocrystalline anisotropy.

As its name suggests, magnetocrystalline anisotropy has its origins in the crystal structure of the material. For an in-depth understanding on how applying a magnetic field along different crystal axes influences the magnetic response of a sample, a single crystal disk is cut parallel to a {110} plane as shown in figure 3.1. The disk will have diameters along the <100>, <110> and <111> directions. *M-H* curve measurements for the directions are shown in figure 3.2 for iron.

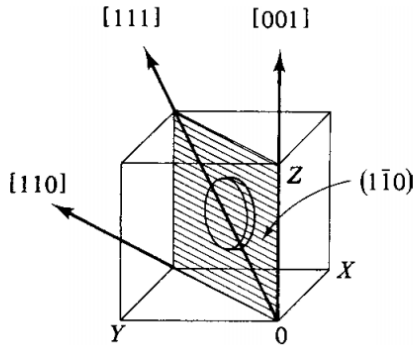

Figure 3.1 Schematic of a disk in the {110} plane of a BCC crystal [60] .

For the <100> direction saturation is achieved with fields lower than 100 Oe hence the name of "easy axis". In the <111> direction the sample requires a field larger than 500 Oe to saturate so this direction is called the "hard axis". The exchange interaction described in section 4.2.1 determines the parallel or antiparallel alignment of spins. This is a very strong interaction but is isotropic. The variation of the interaction is the same in all directions but atom spacing is different with each crystallographic direction so it gives a corresponding relationship for each axis.

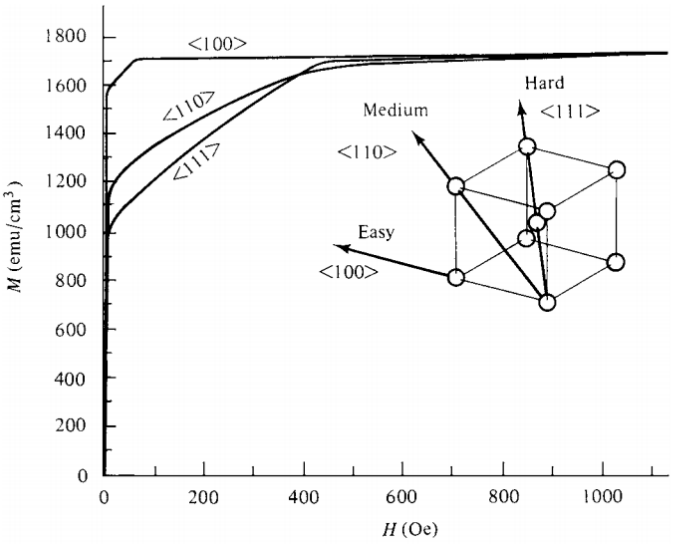

Figure 3.2 Magnetization curves along different directions in an Fe crystal [60].

The orbit-lattice coupling is very strong which leads to the quenching of the orbital magnetic moments so the orientations of the orbits are fixed. The spin is coupled to the orbital angular momentum and large fields are required to rotate the spin. The anisotropy energy which is the energy required to rotate the magnetization away from the easy axis is actually the energy required to overcome the spin-orbit coupling.

The anisotropy energy for cubic crystal structures such as CoFe and IrMn which have been used in this study can be expressed as a series expansion of anisotropy constants dependent on the material and direction cosines α_1, α_2, α_3 of M_S with respect to the crystal axes

$$E_K/V = K_0 + K_1(\alpha_1{}^2\alpha_2{}^2 + \alpha_2{}^2\alpha_3{}^2 + \alpha_3{}^2\alpha_1{}^2) + K_2(\alpha_1\alpha_2\alpha_3) + \cdots \quad (3.2)$$

where K_0, K_1, K_2... are anisotropy constants for a given material of volume V at a known temperature and are measured in ergs/cc. If a uniaxial crystal such as hcp Co has only one easy axis then the expression for E_K has the following form

$$E_K/V = K_0 + K_1 sin^2\theta + K_2 sin^4\theta + \cdots \quad (3.3)$$

Where θ is the angle between the c- axis and M_S. Because of the $\sin^2$ and $\sin^4$ dependence the value $E_K/V \approx K_0$. According to Jung *et al.* [58,61] sputtered CoFe has an anisotropy constant of 2.7×10^4 ergs/cc, considerably smaller than the anisotropy constant for IrMn determined with the York protocol of the order of 10^7 ergs/cc [13].

3.3. Interactions in Thin Films

3.3.1. Direct Exchange

It is expected that the alignment of a magnetic moment in a material will depend on the applied magnetic field, but it is also dependent on the orientation of its neighbouring spins. For two atoms which are close to each other the electron clouds intersect and thus share electrons. If the spins of the two atoms are $\mathbf{S_1}\hbar$ and $\mathbf{S_2}\hbar$ then the potential energy between them is

$$U = -2J_{ex}\boldsymbol{S_1}\cdot\boldsymbol{S_2} = -2J_{ex}S_1S_2cos\theta_{1,2} \qquad (3.4)$$

J_{ex} is a quantum mechanical phenomenon and it has no classical equivalent but it has the effect of a force trying to align the spin parallel or antiparallel. J_{ex} is called the exchange integral and it was first introduced by Heisenberg [62]. This effect is the same as in the explanation of why two hydrogen atoms may come together to form a stable molecule. For a pair of hydrogen atoms situated at a certain distance apart the net electrostatic forces can be calculated using Coulomb's law (attractive forces between electrons and protons – repulsive forces between the electrons and between the protons). However, these are not the only forces acting on the pair of atoms.

A non-classical force is introduced which is dependent on the relative spin orientation of the electrons. A resulting attractive force acts upon the system if the spins are antiparallel and for a certain distance

of separation between the atoms the total energy is reduced for smaller or larger distances. If the spins are parallel then the two atoms repel each other. This is a consequence of the Pauli Exclusion Principle and so the two hydrogen atoms can come so close together that the electrons can occupy the same region of space and have the same energy if their spins are antiparallel. If the spins are parallel the two electrons will tend to stay far apart. Consequently Heisenberg has deduced the same ferromagnetic behaviour as postulated by Weiss.

The Heisenberg model of ferromagnetism considers the quantum mechanical exchange interactions between two neighbouring electrons with overlapping wave functions. Heisenberg introduced the spin of the electron in the wave functions. The resulting energy integral showed that the relative orientations of the spins of two interacting electrons can be changed only by changing the spatial distribution of charge. When two wave functions overlap then the Pauli Exclusion Principle applies to the region of overlap which then leads to a correlation between the spins of the two electrons resulting in a magnetically ordered state.

If J_{ex} is positive the energy in equation 3.4 will have a minimum value only when the spins are parallel so a positive value of the exchange integral is a requirement for ferromagnetic behaviour. The exchange integral varies with the separation between spins. The Bethe-Slater curve in figure 3.3 shows the variation of the exchange integral with the ratio of the atomic radius (r_a) normalised to the 3d subshell (r_{3d}). Together with the relative magnitudes of the elements marked it explains their magnetic properties, such as the Curie temperature T_C.

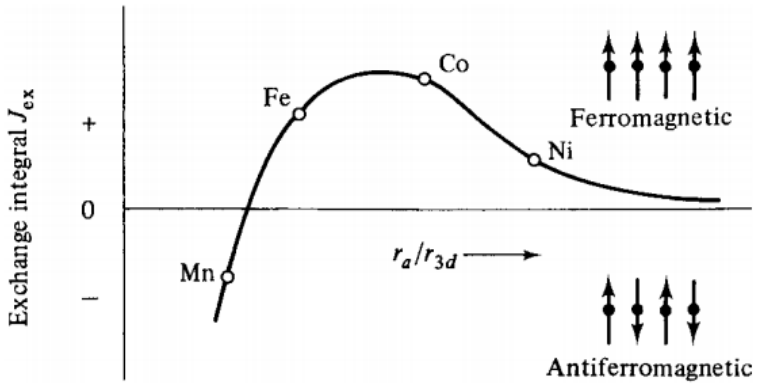

Figure 3.3 The Bethe-Slater curve [60].

For the transition elements the electrons responsible for the net magnetic moment are in the 3d subshell. In the ferromagnetic materials (cobalt, iron, nickel), these electrons come close together and the ratio r_a/r_{3d} is reduced giving J_{ex} a positive value. If brought closer together, J_{ex} becomes negative causing spins to align antiparallel and so explaining the antiferromagnetic behaviour of chromium and manganese below their Néel temperature T_N.

3.3.2. Indirect Exchange

The exchange integral decays rapidly if the atomic separation is large so direct exchange cannot explain ferromagnetism in rare earth metals. This is due to the considerable smaller overlap between the 4f wave functions as the radius of the 4f orbitals is much smaller compared to the interatomic separation [63]. Exchange interactions between atomic spins may not require direct overlap of the orbitals containing the electrons responsible for the magnetic behaviour of elements. The interactions can be mediated by the electrons in the conduction band of the surrounding material. This concept was initially

developed by Ruderman, Kittel, Kasuya and Yosida from where the acronym RKKY derives [64].

For indirect exchange, one atom polarizes the electrons which pass the spin orientation to the next atom. If an impurity is introduced in the material its effect is cancelled due to the spin polarization in concentric rings around the impurity. This interaction can propagate across grain boundaries or defects in materials and influence the orientation of the spin of the next similar atom. Parkin investigated the coupling between ferromagnetic layers by introducing interlayers of nonmagnetic materials of different thicknesses [35]. The sign and strength of the interaction between the ferromagnetic layers oscillated between parallel and antiparallel orientation of spins with the distance between the magnetic moments.

Figure 3.4 shows oscillations in the saturation field of Co-spacer multilayers when the thickness of the spacer layer is varied. The oscillation period ranges between 9 and 11 Å. Apart from Cr all the transition metals give a period for the oscillations of about 10 Å. The strength of the indirect exchange coupling was found to increase from the *5d* to the *4d* to the *3d* metals [35].

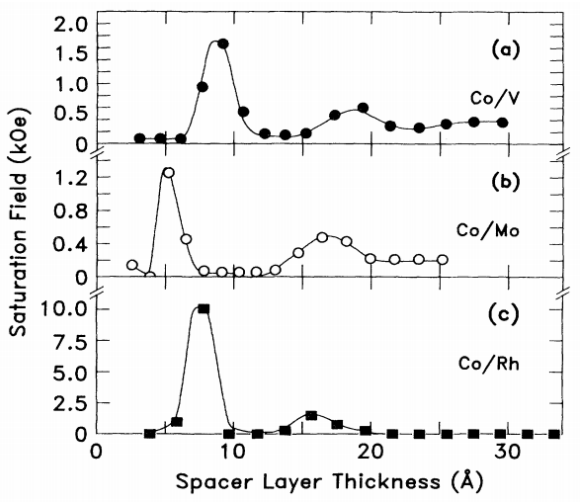

Figure 3.4 Dependence of saturation field in spacer layer thickness in Co/V, Co/Mo and Co/Rh multilayers [35].

3.3.3. Intergranular Coupling

The net behaviour of a sample is given by a combination of the interactions and their contributions and strength dictate the mechanism of magnetization reversal. Two magnetic materials brought close to each other will interact through their dipole fields. The dipolar interaction has a long range but is much weaker than the exchange interaction. For two magnetic dipoles, m_1 and m_2, situated at a large distance the potential energy between them decays with $1/r^3$, where r is the distance between the two poles:

$$U \propto \frac{m_1 m_2}{r^3} \tag{3.5}$$

If the distance is reduced then the potential energy decays by $1/r^2$ and the interaction is much stronger. The exchange interaction however varies in strength in an oscillatory manner and with distance and decreases in amplitude with $1/r^6$. The exchange interaction dominates at short distances and it can be disturbed by defects or grain

boundaries while the dipolar interaction is much longer range and occurs in all materials.

The net behaviour of a granular sample is not only given by the summation of the properties of the grains. The magnetostatic and exchange interactions between the grains also make a significant contribution. The variation of parameters (grain size, easy axis alignment, magnetisation) from one grain to another leads to a distribution of interaction strengths.

The alignment of atomic moments within a grain is dictated by direct exchange, but grain to grain coupling due to direct exchange is rare. The RKKY interaction however can couple through grain boundaries and defects. This is the case for the sputtered polycrystalline CoFe material used in this work. The intergranular exchange coupling is given by

$$h_g = \frac{A_{grain}}{K c_g^2} \tag{3.6}$$

where K is the crystalline anisotropy, c_g is the centre to centre spacing of neighbouring grains and A_{grain} is an effective exchange energy constant measuring the coupling between neighbouring grains [65].

Superexchange is responsible for the antiferromagnetic behaviour of transition metal oxides. This however is not the case for IrMn which is a metallic antiferromagnet. In longitudinal disk media formed from CoPtCr, the Cr was found to segregate to the grain boundaries [66]. The Cr formed an antiferromagnetic alloy, CoCr, which decoupled the grains and had a direct impact reducing noise for recording media. This was an indication that antiferromagnetic grains do not couple. According to Zhu [67] intergranular coupling is dependent on grain magnetisation but the local magnetisation in an AF material is zero. This also means that no conduction electrons can be polarised so that the RKKY

interaction cannot cause indirect exchange. The TEM image in figure 3.5 is also proof that direct exchange does not occur in IrMn films because neighbouring grains almost never have the same crystallographic orientation and the atomic spacing at the grain boundaries is different to that in the bulk material.

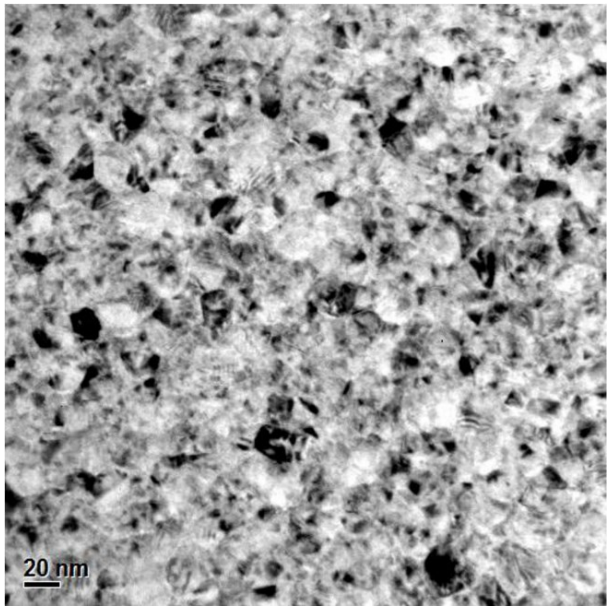

Figure 3.5 TEM image of an IrMn sample.

The hysteresis behaviour in CoFe is governed by magnetostatic and exchange interactions while the grains in IrMn are non-interacting which means they can be compared to a Stoner Wohlfarth system [68].

3.4. Domain Structures in Thin Films

Magnetic domains are regions within a magnetic material which are uniformly magnetised. The areas which separate the domains in which the magnetisation gradually changes its direction are called domain walls (DWs). Domains originate due to the competing energy terms, such as stray fields, anisotropy, shape, size of the sample etc.

Exchange forces explained the magnetic behaviour of certain materials and alloys. The domain concepts were introduced in order to explain why, for example, a piece of iron can be easily found in a demagnetised state. It was Weiss who proposed that ferromagnetic materials in the demagnetised state consist of domains ordered in such a way that the net magnetisation of the sample is zero [69]. Hence, when a F body is magnetised it is switched from a multi-domain to a mono domain state, as shown in figure 3.6.

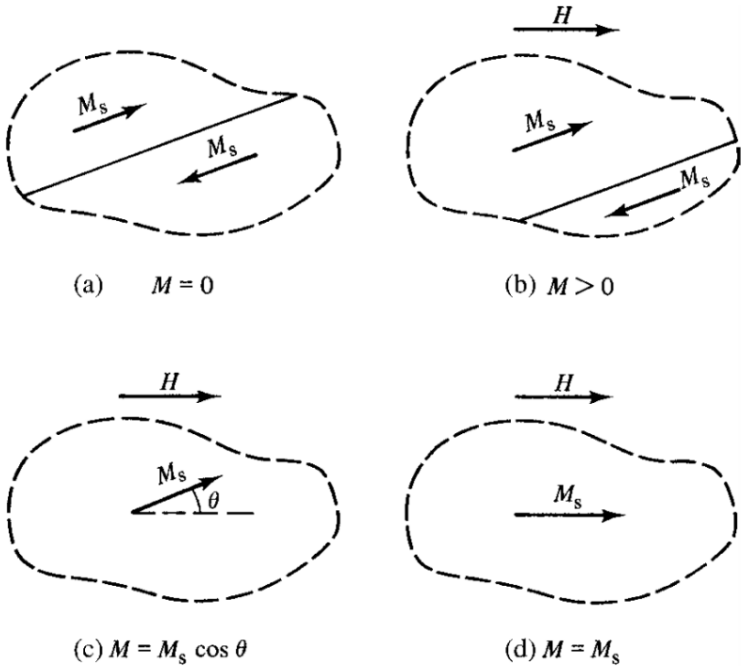

Figure 3.6 Schematic of domain structures during the magnetisation process [60].

Figure 3.6a shows the F sample in a demagnetised state (***M***=0). For simplicity two domains are considered. The two domains are separated by a domain wall. Formation, destruction and movement of domain walls are the processes through which the magnetisation process is controlled. When a non-saturating field ***H*** is applied the domain wall is moved so that ***M***>0 (figure 3.6b). When the magnitude of the applied field is increased the domain wall moves through the sample until the sample becomes single domain (figure 3.6c). Further

increasing the magnitude of ***H*** results in rotation of the final domains in order to align to the applied field and the sample reaches saturation (figure 3.6d).

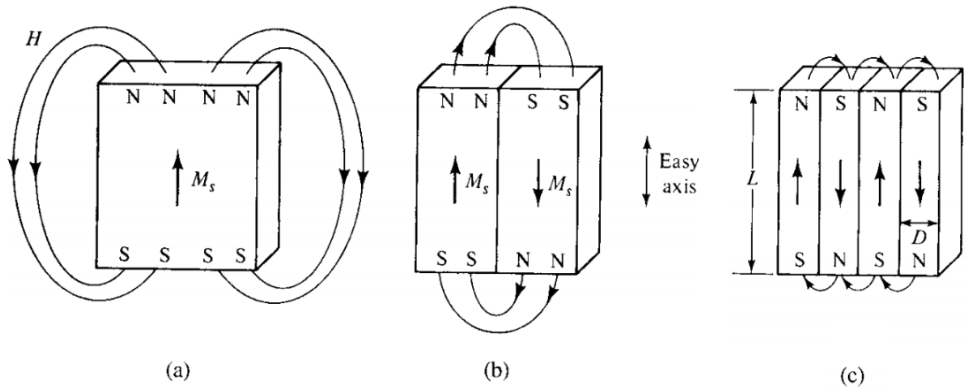

Figure 3.7 Division of a crystal into domains [60].

Domains are created in order to minimise the magnetostatic energy. The magnetostatic energy is large because single domain samples exhibit a large demagnetising field H_D. This is shown in figure 3.7. The energy per unit area on the top surface of the crystal shown in figure 3.7 is given by

$$E_{ms} = \frac{2}{3}\pi M_s^2 D_T \tag{3.7}$$

where D_T is the thickness of the domain. So by splitting into multiple domains the magnetostatic energy is reduced and by splitting into even more domains, magnetostatic energy is reduced even more. However, by creating multiple domains, multiple domain walls are created, but domain walls cannot be infinitely small. The size of domain walls is limited by the exchange energy expressed in equation 3.8. In order to reduce the energy of the domain wall, the spins do not change their orientation abruptly, but switch with small angles over a series of atoms. This is given by

$$E_{ex} = 2A_{es}\cos\left(\frac{d\theta}{dx}\right) \tag{3.8}$$

where $A_{es} = (n_A J_{ex} S_i S_j / L_p)$ is the exchange stiffness where n_A is the number of atoms per unit cell and L_p is the lattice parameter. Equation 3.8 shows that in order to minimise E_{ex} the DW should be as thick as possible. However, the anisotropy energy reduces the DW thickness by limiting the number of atoms away from the easy axis. For two neighbouring domains with opposite magnetisations in an Fe crystal the change occurs over 120 atoms, giving an angle between spins of 1.5°. This type of domain wall is called a 180° DW and it is shown in figure 3.8.

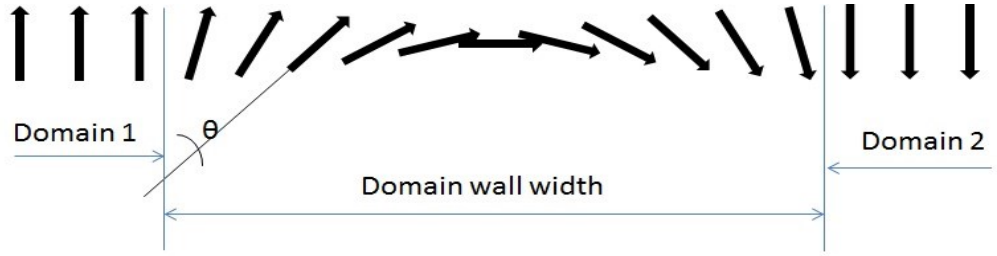

Figure 3.8 Schematic structure of a 180° domain wall [60].

Complex DWs arise due to competing exchange energy, magnetostatic energy and magnetocrystalline anisotropy. These parameters dictate domain size and DW width. Polycrystalline thin films are no exception from this because of the exchange between grains with different easy axis orientation [63].

4. Exchange Bias

4.1. Magnetic Multilayers

Magnetic thin films, nanostructures and multilayers are of great importance as they provide the framework for modern technologies such as hard drives, magnetic random access memories etc. The state-of-the-art technology has already reached layer thicknesses in applications of less than 0.5 nm – only one atom thick – slowly evolving in what is atomic engineering. Magnetism at this scale is well understood but the association of different layers which may be a combination of magnetic and non-magnetic materials leads to a broad spectrum of behaviour: perpendicular anisotropy [70], magnetoresistance [18] or magneto-optical effects [71].

Usually for magnetic thin films, the easy axis of magnetization lies in the plane of the film. The preferred direction of magnetisation can be set, for instance to lie perpendicular to the plane of the film, by using Co layers with non-magnetic interlayers such as Pt, Au, Pd, Ru. The dominance of the perpendicular anisotropy can be tuned by varying the thickness of the non-magnetic interlayers [35]. Modern day hard drives use materials with natural perpendicular anisotropy for their recording media.

Another very important technology driving applications of magnetic multilayers is the read process in hard drives. This is performed by the read head which consists of a spin-valve sensor. The spin-valve is formed by two ferromagnetic layers separated by a non-magnetic layer. The non-magnetic interlayer can be conductive in which case the spin-valve is a giant magnetoresistance (GMR) sensor or an insulator in which case the spin-valve is a tunnelling magnetoresistance sensor (TMR). The relative orientation of the magnetization in the two

ferromagnetic layers and hence the magnetoresistance is dependent on the stray fields from the recording medium. In order to obtain the maximum signal from the hard disk one of the ferromagnetic layers in the spin-valve is given a fixed orientation by being exchange coupled to an adjacent antiferromagnetic layer as suggested by Grünberg [72] in his Nobel Prize winning work:

$$\frac{\Delta R}{R} \propto \boldsymbol{M_1} \cdot \boldsymbol{M_2} \tag{4.1}$$

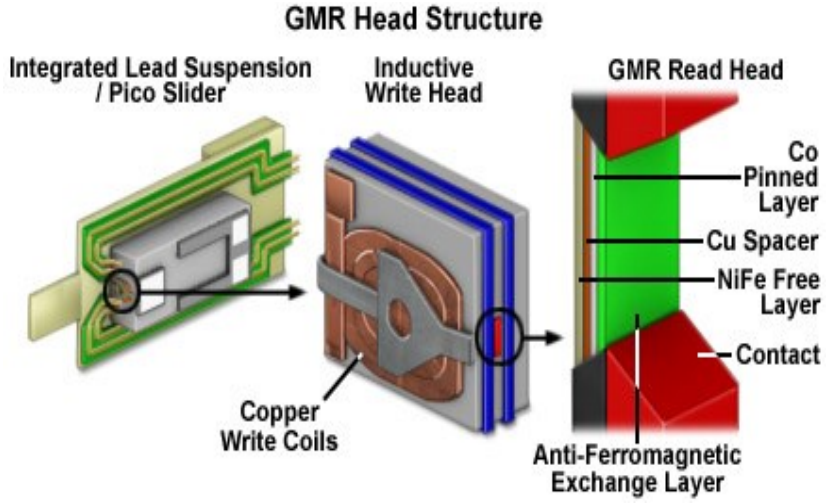

Figure 4.1 Schematic diagram of a GMR recording head.

Magnetic multilayers are used everywhere from sensors to data storage hence their significant importance and broad field for fundamental study. Their behaviour is due to the competing interactions at the atomic level. Any system tends to a minimum in energy so for magnetic thin films exchange interactions try to keep the magnetic moments aligned in a rigorous manner – parallel or antiparallel – whereas anisotropy effects compete with preference to certain crystallographic axes. This leads to breaks in the order induced by the exchange interactions or formation of domain walls. These concepts will be discussed in the following sections.

4.2. Magnetic Anisotropy

4.2.1. Antiferromagnetic Anisotropy

The ordering in antiferromagnetic materials is dictated by direct exchange. The Bethe-Slater curve shows that the orientation of the exchange integral is dictated by the separation of the magnetic shells. It is defined by the difference between the *3d* band and the atomic separation. If the difference is within 1.1-1.5 Å then the behaviour is ferromagnetic. For differences smaller than 1.1 Å the exchange integral J_{ex} changes sign and promotes antiferromagnetic or ferrimagnetic alignment of the spins.

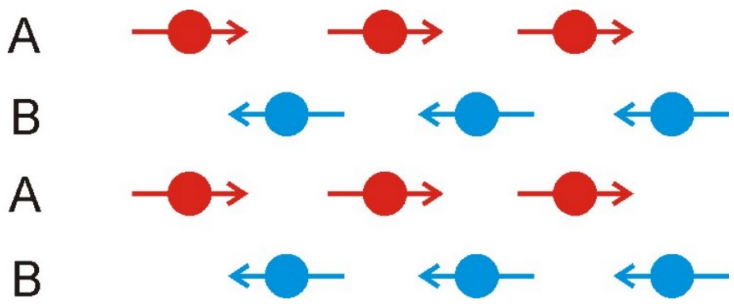

Figure 4.2 Antiferromagnetic spin structure schematic with A and B sublattices [73].

Figure 4.2 shows a schematic for the spin alignment of an antiferromagnetic material with two sublattices A and B. The interaction felt by an ion in the A sublattice can be split in two components, one from the neighbouring A ions and another one from the B ions. All ions in one sublattice will order parallel to each other while adjacent sublattices will have antiparallel alignment. The condition for a material to be antiferromagnetic is to have the same number of A and B ions. If this condition is not fulfilled then the material is ferrimagnetic.

There are two antiferromagnetic crystallographic structures for $IrMn_3$, γ-$IrMn_3$ and $L1_2$-$IrMn_3$ [74,75]. Neutron diffraction was performed

only on the latter one and was shown to have a trigonal structure. The Mn spins are parallel to the {111} plane and lie in the <112> direction as shown in figure 4.3.

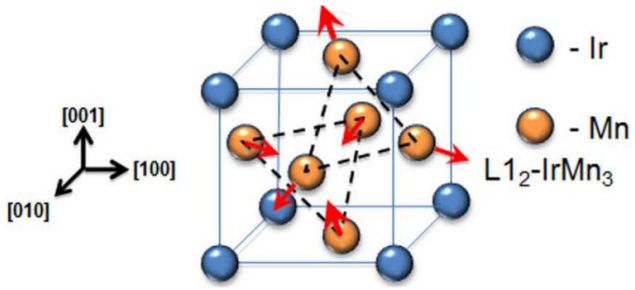

Figure 4.3 Crystal structure of L12- $IrMn_3$ [73].

Antiferromagnetic materials usually require neutron diffraction to characterise them making them difficult to evaluate. It has been shown that exchange bias in the case of IrMn depends on the content of iridium reaching a maximum peak when the iridium has a concentration in the range 22-32% [76]. In the case of the deposition system used in this work the maximum exchange bias was shown to lie in the range 13-22% iridium. This is representative of an $IrMn_4$ alloy [77] and not $IrMn_3$ as was believed previously [76].

IrMn is a sheet antiferromagnet where the Mn atoms having the high magnetic moment lie on a plane which is one of the (111) diagonal planes of the crystal cell. Because of the magnetocrystalline nature of the anisotropy in antiferromagnets generally the anisotropy constant is unvarying, but defects in the crystal lattice can lead to a distribution of anisotropy constants (K_{AF}). The high degree of crystallinity of the IrMn can be seen in figure 4.4. The magnetocrystalline origin leads to a temperature dependence [78] which can be expressed in the form:

$$K_{AF}(T) = K_{AF}(0)(1 - \frac{T}{T_N}) \qquad (4.2)$$

where T_N is the Néel temperature of the antiferromagnetic material. Even if the crystal structure of the antiferromagnet is cubic (IrMn) the anisotropy is uniaxial due to the spin orientation along the body diagonal plane. In polycrystalline films with grain sizes <20 nm, each grain contains a single antiferromagnetic domain. This leads to a Stoner-Wohlfarth type reversal where the energy barrier to reversal is given by [13]

$$\Delta E = K_{AF} V (1 - \frac{H^*}{H_K^*})^2 \tag{4.3}$$

where H^* is the exchange field acting on the antiferromagnet from the ferromagnetic layer and H_K^* is a pseudo anisotropy field representing the resistance of the anisotropy of the antiferromagnet to its orientation being reversed.

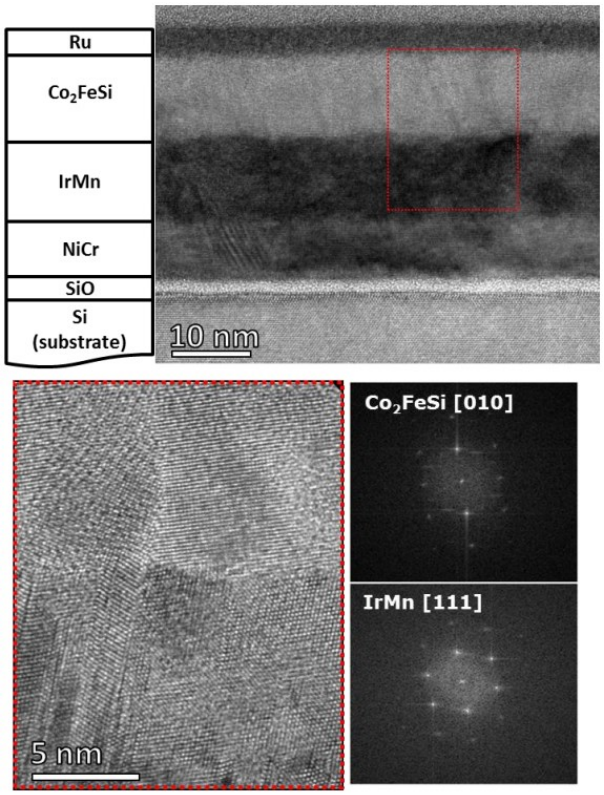

Figure 4.4 Cross section HRTEM images of a Co_2FeSi sample exchange biased with IrMn [79].

4.2.2. Exchange Anisotropy

Exchange anisotropy is due to the exchange interaction discussed in 3.3. The spins of the ferromagnet are coupled to the spins of the antiferromagnet across the interface. This creates a uniaxial anisotropy for the coercivity and a unidirectional anisotropy for the exchange field, indicated by a characteristic shift on the field axis of the hysteresis loop [80].

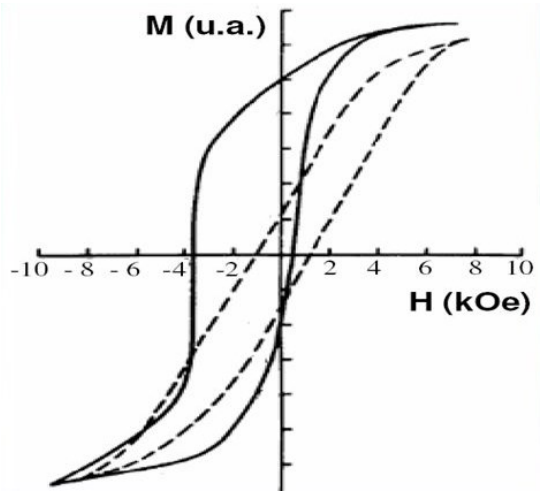

Figure 4.5 The original results of Meiklejohn and Bean for Co/CoO particles [10].

Exchange anisotropy was discovered in 1956 by Meiklejohn and Bean [10]. They were studying the coercivity in elongated 20 nm single domain Co particles. Part of the fabrication process of these particles was an oxidation step after which the particles had a CoO shell around the ferromagnetic core. Above the Néel temperature T_N the particles were paramagnetic. After field cooling in a 10 kOe field magnetic measurements were performed at 77 K and showed a shifted hysteresis loop along the field axis. The shift was due to the coupling of the ferromagnetic Co core to the antiferromagnetic CoO shell. The loop shift H_{ex} is called exchange bias.

Figure 4.6 shows the spin diagram at the interface between the Co particles and their CoO shell. After the fabrication process, the spins in the single domain Co particles are aligned parallel to each other and the spins in the CoO have random orientations. After heating the sample above 292 K, which is the Néel temperature of the CoO, and cooling in an applied magnetic field, the spins in the CoO align antiparallel and have an antiferromagnetic behaviour. The strong coupling at the interface acts to align the nearby Co spins. This results in a smaller field required to align the spins in a positive field (H>0) and a larger field in the opposite direction in order to overcome the coupling.

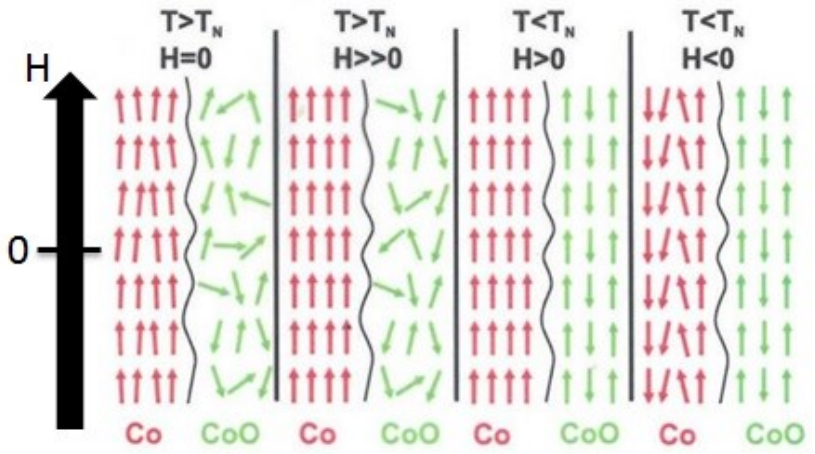

Figure 4.6 Schematic diagram for Co/CoO spins at the interface.

The CoO suffers a transition from paramagnetic to antiferromagnetic ordering when cooling below the Néel temperature of the CoO. The unidirectional anisotropy requires a larger negative field to reverse the magnetisation than otherwise necessary. Even if exchange bias was discovered in particles, the exchange anisotropy can be induced in films at the interface between the ferromagnetic and antiferromagnetic layers.

4.2.3. Texture Effects in Polycrystalline Antiferromagnetic Materials

The anisotropy of individual particles will average out in a sample containing particles with random orientations of their easy axes. If, for any reason, the grains have an overall preferred orientation then the material has a crystallographic texture. Texture is induced in a material via the forming process: rolling a sheet, pressing a powder or creating wires [60].

In this study the materials used were BCC CoFe and FCC IrMn. Traditionally, IrMn is deposited on seed layers which then determine the crystallographic orientation of the (111) planes. In order to determine the anisotropy constant, the measurement [81] and analysis [82] procedures of the York Protocol were followed. The origin of anisotropy in IrMn is magnetocrystalline. The thermal stability is controlled via the anisotropy constant K_{AF} giving rise to the energy barrier $\Delta E = K_{AF}V$. Hence the control of the texture and K_{AF} allow for the optimum thickness of IrMn to be selected for any application.

Thin films are influenced by seed layers. Their properties are dictated by the surface roughness, grain size and lattice parameters of the underlayer or seed layer. These factors give control over the anisotropy of the sample. It has been found that in the case of IrMn a strong (111) texture results in a high exchange field [83]. A correlation between strong (111) in-plane texture and the anisotropy of IrMn deposited by HiTUS (5.1.2) has been found [84]. The texture can be controlled via the use of seed layers and X-ray diffraction studies showed strong (111) texture in particular for NiCr seed layers of 6 nm thickness [85]. The anisotropy of IrMn also shows a dependence on composition [86] and inclusion of impurities [87]. Since the anisotropy of IrMn controls its thermal stability, the ability to control the

crystallinity of IrMn allowed for significant reductions in the thickness of the antiferromagnetic layer in sensor applications and hence the dimensions of the devices were reduced [13].

4.3. The York Model of Exchange Bias

4.3.1. Energy Barriers

Hysteresis in magnetic materials is due to the existence of a non-equilibrium state which derives from crystal imperfections which act as domain wall pins. The magnetocrystalline anisotropy in single domain particles prohibits the nucleation of domain walls which also results in magnetic hysteresis. The magnetocrystalline anisotropy resists moment rotation in single domain particles. Ferromagnets with high magnetocrystalline anisotropy exhibit larger hysteresis due to magnetic moments preferring to lie in certain crystallographic axes. Both these effects, the domain wall pins and the anisotropy, force the magnetic moments to overcome an energy barrier to switch their orientation.

According to Brown, the magnetic moment in a single domain particle "wobbles" around an equilibrium position [88]. The probability of the moment to reverse its orientation arises when the thermal energy $k_B T$ overcomes the anisotropy energy barrier. The reversal of the magnetisation of a grain at finite temperatures has a relaxation time given by the Néel-Arhenius law [89]

$$\tau^{-1} = f_0 exp\left(-\frac{\Delta E}{k_B T}\right) \tag{4.4}$$

where τ is the time in which the magnetisation decays to $1/e$ of its initial value. The frequency f_0 is the attempt frequency and it represents the number of times per second the magnetic moment tries to overcome

the energy barrier and reverse. It ranges between 10^9 and 10^{12} Hz [90]. If a relaxation time of 100 s is assumed then $\Delta E=25k_BT$. The requirements for magnetic recording are to store information for 10 years which results in a much higher required energy barrier of $40k_BT$.

A simplified case is assumed in order to derive an expression for the energy barrier for reversal of the magnetisation. In a system consisting of single domain particles with the easy axes perfectly aligned with an applied field, the *M-H* curve, or the hysteresis loop, will exhibit perfect squareness. The total energy is the sum of the anisotropy and the Zeeman energies

$$E_{total} = KVsin^2\theta - m_sHVcos\theta \quad (4.5)$$

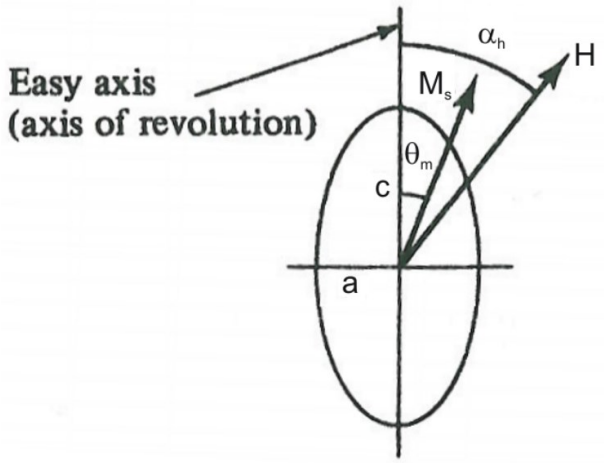

Figure 4.7 Schematic of a single domain particle [60].

where θ is the angle between the easy direction and the applied field H. Two equilibrium cases are distinguished when the energy reaches a minimum value at θ=0° and θ=180°, respectively. In order to switch from one equilibrium position to the other a switching field is required. The energy barrier will be the difference between the maximum and the minimum energy and it is this barrier that the switching field needs to overcome. For a single domain particle the energy barrier ΔE is

$$\Delta E = KV\left(1 - \frac{H}{H_K}\right)^2 \quad (4.6)$$

where H_K is the anisotropy field. The anisotropy field defines the maximum possible coercivity of the system. Equation 4.8 also shows the dependence of the energy barrier on particle volume V and anisotropy constant K. This is for a single particle but in real systems a distribution of particle volumes and anisotropies exist. The particle size distribution is further discussed in section 4.3.4. The distribution of energy barriers $f(\Delta E)$ allows an explanation of a number of phenomena in ferromagnetism.

4.3.2. Time Dependence

The time dependence of magnetisation is known as the magnetic viscosity of the material. The magnetic viscosity introduces a delay in the response of the magnetisation to an applied field trying to switch it. Street and Woolley showed that the magnetisation M changes linearly with the natural log of the time elapsed since the field has been changed [90]

$$M(t) = const. + S\ln\left(\frac{t}{t_0}\right) \quad (4.7)$$

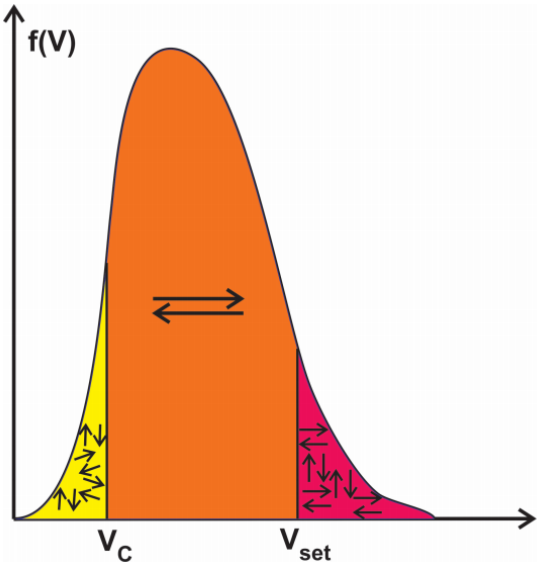

Figure 4.8 Schematic diagram of the AF grain volume distribution with the threshold volumes V_C and V_{SET} [73].

where t_0 is a constant and S is the magnetic viscosity coefficient. The magnetic viscosity coefficient is the rate of change of magnetisation with ln*(t)*. It is positive if the field is increasing its strength. When $\Delta E > 25k_BT$ the magnetic viscosity coefficient remains constant over long periods of time [91]

$$S(H) = \frac{dM}{d(\ln t)} = 2M_s k_B T f(\Delta E)_{\Delta E_C} \tag{4.8}$$

where T is temperature, M_S is the saturation magnetisation of the ferromagnet and ΔE_C is the critical energy barrier being overcome. In an antiferromagnet the net magnetisation is zero so the order of the antiferromagnet is chosen as an analogous for the magnetisation in a ferromagnet hence

$$S = \frac{dP}{d(\ln t)} = 2P_s k_B T f(\Delta E)_{\Delta E_C} \tag{4.9}$$

where P_S is the saturation value of the order of the antiferromagnet. For an antiferromagnetic grain in a polycrystalline thin film the energy barrier depends on the volume of the grain [68] so a distribution in grain sizes generates a distribution of energy barriers. It has been

shown that the linear dependency on ln(t) is a special case when f(ΔE(t)) is constant over the time of the measurement and thus true for when the distribution is wide [92-94]. For exchange bias the logarithmic time dependence has been shown by Hughes [95].

4.3.3. The Setting Process

The setting process is that through which order is induced in the antiferromagnet layer. An ordered antiferromagnet will be referred to as "set". For the samples used in this work the antiferromagnetic grains were set by heating below the Néel temperature so that the sample structures did not get damaged. The antiferromagnetic grains are aligned by the exchange field from the adjacent ferromagnetic layer and thermal activation, hence this process is time dependent.

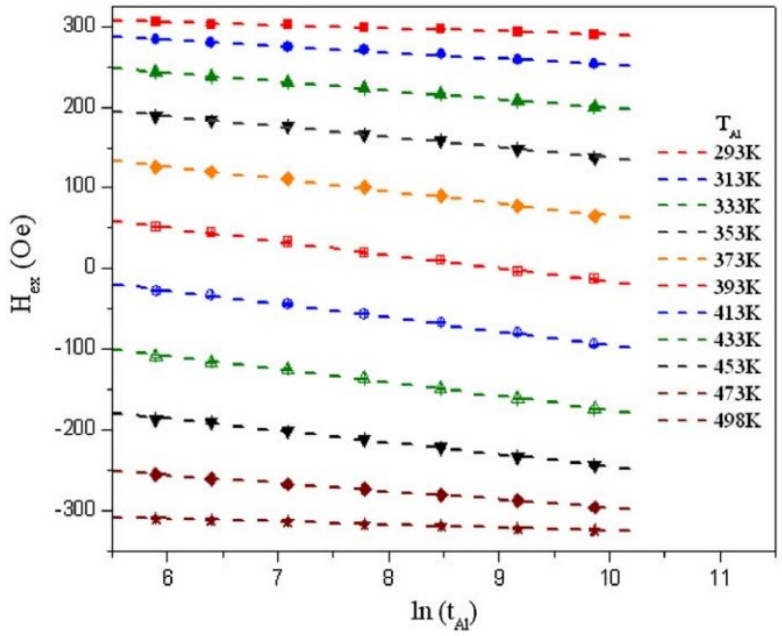

Figure 4.9 Time dependence of H_{EX} with ln(t) [95].

The exchange bias was measured as a function of the setting time for temperatures in the range 293 K-498 K by Vallejo-Fernandez *et al*

[96]. The linear dependence between H_{EX} and ln*(t)* was observed as shown in figure 4.9. The resulting exchange bias was a result of the increase of the temperatures at which the field setting was performed. Because the notation T_{SET} is for the highest possible temperature at which the field setting can be performed the notation T_{AL} was used instead.

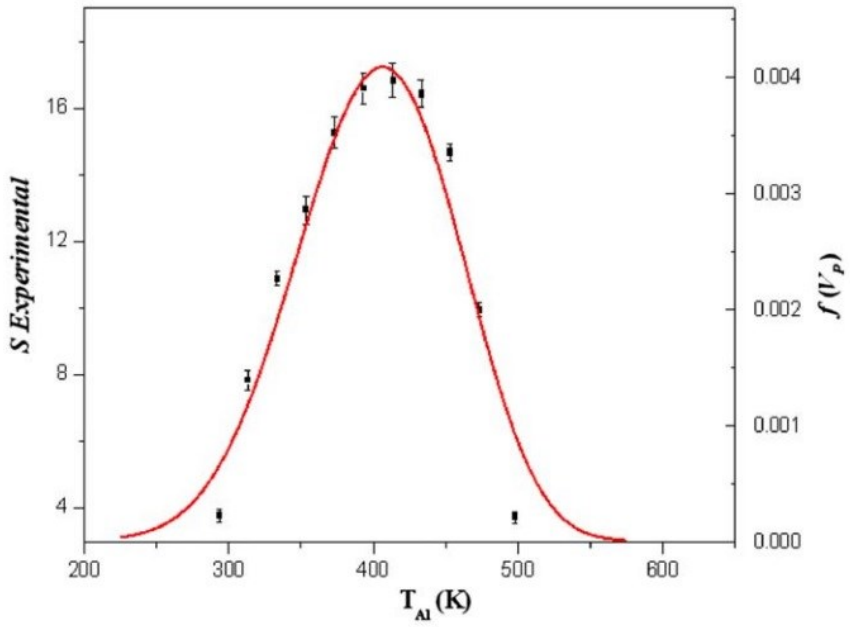

Figure 4.10 Magnetic viscosity S as a function of T_{AL} [95].

Figure 4.10 shows the magnetic viscosity *S* calculated from the gradients of the linear fits in figure 4.9:

$$S(T, H^*) = 2P_S k_B T K f(V_{AL}) \qquad (4.10)$$

where V_{AL} is the volume of the grain which overcomes the energy barrier at a given temperature. The volume distribution was calculated from TEM studies. Figure 4.10 shows the magnetic viscosity as a function of setting temperature. It was expected that deviations should occur at the extremes of the temperature range. This was due to the small number of grains at the extremes of the grain size distribution, thus giving larger uncertainties in the value of *S*. The excellent fit is a confirmation of the York Model and that *K* is effectively constant.

There is more information that can be extracted from the fact that there is a distribution of grain volumes and that the process is time dependent. Firstly it is known that smaller grains are thermally unstable. Secondly, because of setting the sample below the Néel temperature, there are grains with large volumes that cannot be set. Hence, V_C is the smallest grain which can be set and V_{SET} is the maximum grain volume than can be aligned. The exchange bias is then proportional to the fraction of the grains lying between these two limits. Equation 4.11 shows the relationship between the exchange bias and the volume distribution shown in figure 4.12.

$$H_{EX}(T_{ms}) \propto \int_{V_C}^{V_{SET}} V f(V) dV \tag{4.11}$$

The fit to the model indicates that the anisotropy must be uniform. TEM studies confirm the uniformity of the anisotropy showing a remarkable crystallinity of the IrMn. This is due to the growth conditions of the HiTUS sputtering system (Section 5.1.2) where the sample substrate is at a large distance from the target allowing for slow sputtering rates where the incident particles migrate to the lowest energy position.

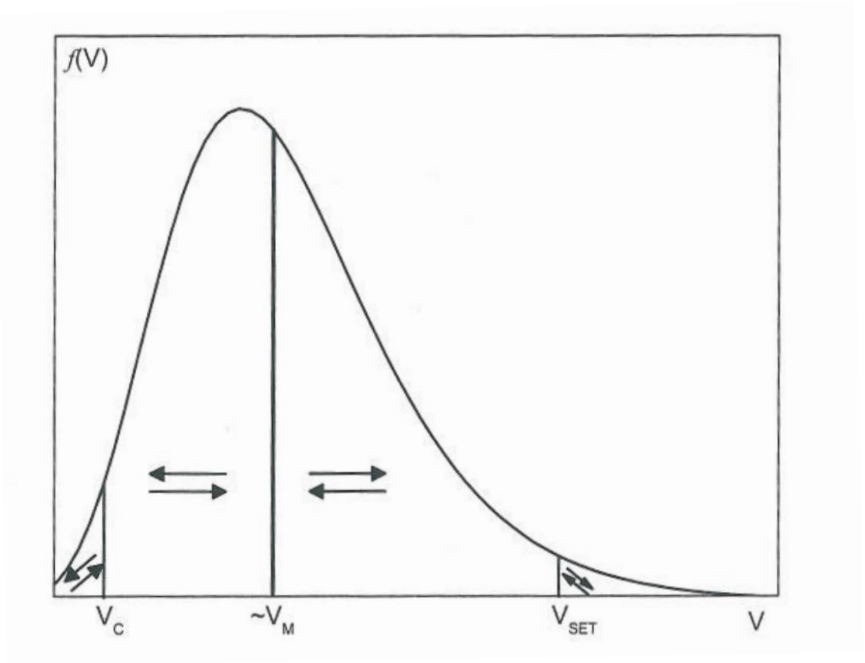

Figure 4.11 The grain volume distribution at the blocking temperature showing the critical volumes and median grain volume.

From the Néel-Arhenius law discussed in section 4.3.1, and knowing the relaxation time for an antiferromagnetic grain, the critical volumes can be deduced by rearranging the equation. V_{SET} is the largest grain volume which can be set in the time t_{SET} at temperature T_{SET}. If the grain volume V is larger than V_{SET} ($V > V_{SET}$) then the grain cannot be set by thermal activation due to having too large an anisotropy energy. Such grains do not contribute to the exchange bias and are oriented at random.

$$V_{SET} = \frac{k_B T_{SET} \ln(f_0 t_{SET})}{K_{AF}(T_{SET})} \tag{4.12}$$

Grains that are too small, $V < V_C$, will be thermally unstable and will not contribute to the exchange bias. Their critical volume is given by

$$V_C = \frac{k_B T_{meas} \ln(f_0 t_{meas})}{K_{AF}(T_{meas})} \tag{4.13}$$

where t_{meas} is the measurement time and T_{meas} is the temperature of the measurement.

4.3.4. Grain Volume Distributions

The grain diameter distribution in sputtered polycrystalline films is log-normal due to the nature of the growth [97]. The standard deviation of ln*(D)* is between 0.2 and 0.6. The volume distribution is more asymmetric than the diameter distribution which means that the number of very large grains is very small. Since $V = \pi D^2 t_{AF}/4$ and $\sigma_{\ln(V)} = 2\sigma_{\ln(D)}$ then the standard deviation for the volume distribution lies between 0.6 and 1.5.

For the York Model the grain size distribution is obtained from grain size measurements using TEM images of the sputtered films. TEM grids are processed in the deposition system at the same time with the samples for the magnetic measurements. The value of exchange bias is obtained from the distribution function

$$H_{EX}(T) \propto \int_{V_C}^{V_{SET}} V dV \tag{4.14}$$

Integrating over the log-normal grain volume distribution gives a sigmoidal curve for the blocking temperature for different grain sizes.

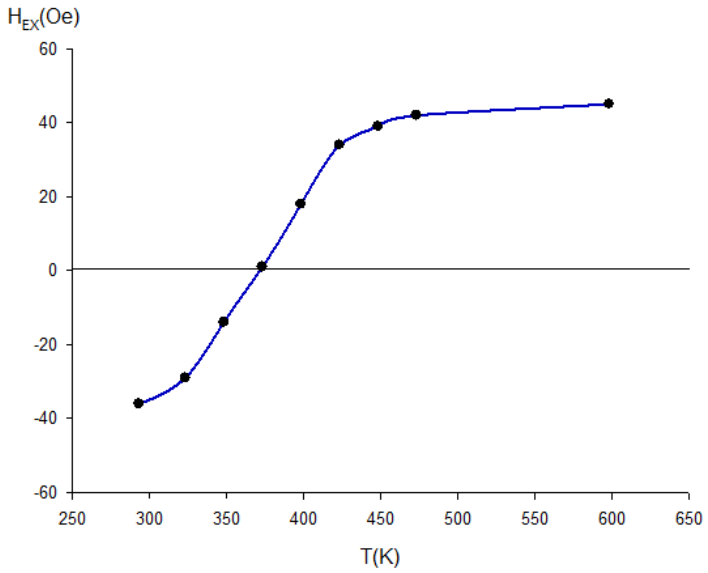

Figure 4.12 Blocking curve measurement for a CoFe(20)/IrMn(5) film.

4.3.5. The Blocking Temperature

Fulcomer and Charap showed that thermal fluctuations can lead to switching of the antiferromagnetic grains similar to superparamagnetism in small ferromagnetic particles [68]. Further to the discussions in sections 4.3.3 and 4.3.4, antiferromagnetic grains can behave in three ways. They can be unstable, blocked or unset grains. This classification of the grains is done relative to the timescale of the measurement so that small grains have low energy barriers and thermal energy can reverse them during the measurement. Slightly larger grains are blocked and they retain their orientation during the measurement. Unset grains have the largest energy barriers of the three and the probability of them switching is way beyond the duration of the measurement. In polycrystalline films the grains come in a distribution of sizes so all three behaviours are present.

Before the York Protocol, blocking curves were measured at higher and higher temperatures until the exchange bias was zero. With the information from the York Model the temperature at which the

exchange bias became zero in the conventional measurements was in fact the blocking temperature of the grain with the largest energy barrier. Hence, this type of measurement was influenced by the logarithmic time dependence of the changes in the antiferromagnet. Measurements made using the York Protocol are carried out at the temperature of no activation, T_{NA}, a characteristic temperature for the system where no thermal activation occurs. The method for measuring T_{NA} is presented in section 6.2.3.

As a consequence of the York Model, the average blocking temperature $<T_B>$ in the York Protocol is the temperature at which equal portions of the antiferromagnet are ordered in opposite directions so that the exchange bias is zero. From the mean blocking temperature the mean volume $<V>$ of the thermally activated particles can be deduced. A comparison between the conventional measurement and measurements done via the York Protocol is shown in figure 4.13 [13].

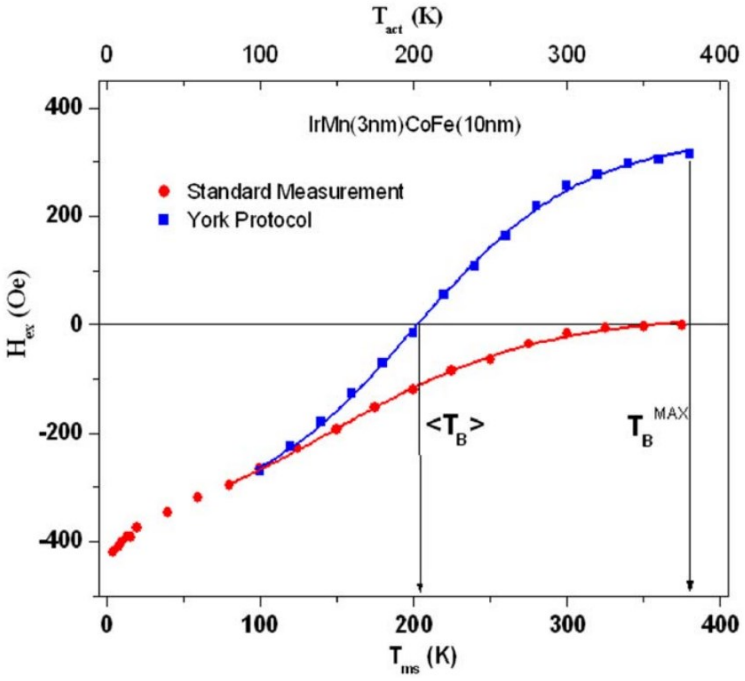

Figure 4.13 Comparison of conventional and York Protocol blocking temperature[13].

The York Protocol is a measurement procedure for obtaining reproducible results independent of the timescale of the experiment and it was implemented by Fernandez-Outon *et al* [81]. The first step in this procedure is to set the antiferromagnet (section 4.3.3). To do so, a temperature is chosen at which the majority of the grains will be unstable. Since only the majority of the grains are unstable, a fraction of the grains will not become unstable and it is these grains which will remain unset. Attempts to increase the temperature may result in layer interdiffusion destroying the films or might reach the limitations of the cryostat in the magnetometer. This is also the reason why the blocking temperature curve in figure 4.13 is not saturated.

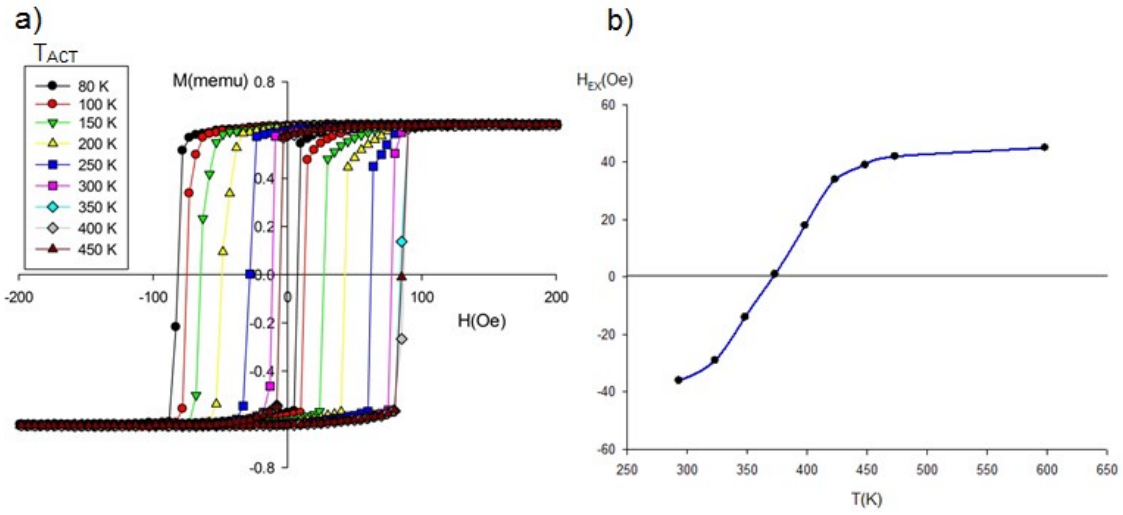

Figure 4.14 a)Thermal activation measurement according to the York Protocol for a CoFe(20)/IrMn(5) film and b) the associated blocking curve.

At the mean blocking temperature, the exchange bias is zero. The measurements associated with the blocking curve in figure 4.13 are shown in figure 4.14. As the temperature increases the hysteresis loops shift on the field axis as the thermal activation temperature increases. Once past zero the exchange bias will increase until all the grains are set in the opposite direction to the one they were initially set. Equal

fractions of the antiferromagnet volume are oriented in opposing directions when the exchange bias is zero.

4.3.6. The Anisotropy Constant

The blocking temperature curve obtained via the York Protocol can be used to obtain a value for the anisotropy constant [82]. The grain size distribution is aligned in one direction after setting at a temperature T_{SET} for a time t_{SET}. The ferromagnetic layer is then saturated in the opposite direction and, with the field still applied, the sample is held at a temperature T_{ACT} for a period t_{ACT}. This will result in switching part of the antiferromagnet in the opposite direction. The largest grain switched will then give the value for the exchange bias. Equation 4.15 is a mathematical expression of the previous statements.

$$H_{EX}(T_{ACT}) \propto C^* \left[\int_0^{V_{ACT}} f(\Delta E) d(\Delta E) - \int_{V_{ACT}}^{V_{SET}} f(\Delta E) d(\Delta E) \right] \qquad (4.15)$$

where C^* is the interfacial coupling constant. The procedure is repeated for higher and higher activation temperatures T_{ACT} until all the initially set grains are reversed. Sweeping the temperature T_{ACT} from T_{NA} to T_{SET} inevitably T_{ACT} will reach the value of $<T_B>$. This occurs when the grains being activated have the median grain volume V_m. At this point H_{EX} is zero so the interfacial effects C^* cancel so equation 4.15 becomes

$$H_{EX}(\langle T_B \rangle) \propto C^* \left[\int_0^{\langle T_B \rangle} f(T_B) d(T_B) - \int_{\langle T_B \rangle}^{\infty} f(T_B) d(T_B) \right] \qquad (4.16)$$

Given that $KV = \ln(tf_0)kT_B$, the anisotropy constant is then given by

$$K_{AF}(\langle T_B \rangle) = \frac{\ln(tf_0)\, k\langle T_B \rangle}{V_m \left[1 - \frac{H^*}{H_K^*}\right]^2} \qquad (4.17)$$

If the ferromagnetic layer is thin, then the exchange field H^* is small so the term H^*/H_K^* can be neglected [98] so the anisotropy constant becomes:

$$K_{AF}(\langle T_B \rangle) = \ln(tf_0)\, k\langle T_B \rangle / V_m \tag{4.18}$$

The mean grain volume is

$$V_m = D_L^2 \pi t_{AF}/4 \tag{4.19}$$

where D_L is the mean lateral grain diameter and t_{AF} is the thickness of the antiferromagnet. From equations 4.17 and 4.18 the grain volume being activated can be calculated for a given temperature

$$V_{ACT} = \frac{k_B T_{ACT} \ln(f_0 t_{ACT})}{K_{AF}(T_{ACT})} \tag{4.20}$$

If T_{ACT} is replaced by T_{NA} and T_{SET} then the values for the critical volumes V_C and V_{SET} can be calculated. Integrating the grain volume distribution between these limits gives the exchange bias at any temperature.

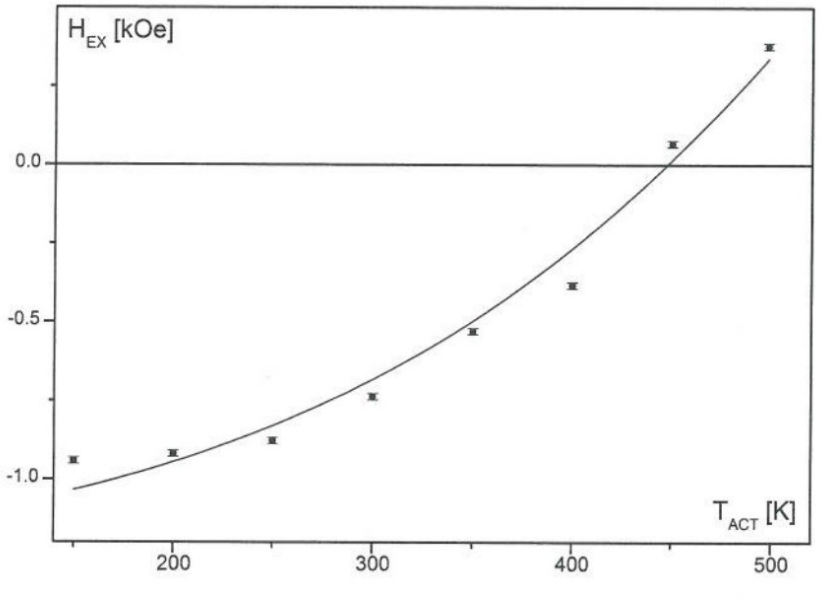

Figure 4.15 Example of a thermal activation measurement with the fitted line calculated from K_{AF}.

Excellent agreement is found between theory and experiment by fitting equation 4.21 to measured values for H_{EX}. The excellent fit is shown for the blocking curve in figure 4.15. The sample has a mean grain size of 3.6 nm and an anisotropy constant at the blocking temperature of K_{AF}=2.18×10^7 ergs/cc. The mean blocking temperature is $<T_B>$=448 K.

$$H_{EX}(T) \propto \int_0^{V_{ACT}} f(V)dV - \int_{V_{ACT}}^{V_{SET}} f(\Delta V)d(\Delta V) \qquad (4.21)$$

4.3.7. Grain Size and Film Thickness Dependence

Before the York Model, many measurements were reported that the exchange bias increases [99] or decreases [100] with increasing the antiferromagnetic layer thickness. In order to explain the behaviour of exchange bias systems with the variation of the antiferromagnetic layer thickness and grain size, an experiment has been carried out by Vallejo-Fernandez *et al.* [101]. The samples consisted of a ferromagnetic CoFe layer and an antiferromagnetic IrMn layer. For the same CoFe thickness, six different samples were grown with different IrMn thicknesses. In addition, four grain size distributions were studied for three thicknesses of IrMn. The two critical volumes were calculated from the anisotropy measurement described in 4.3.3. Figure 4.16 shows the grain volume distributions and the different fractions of the distributions in the window between the two critical volumes.

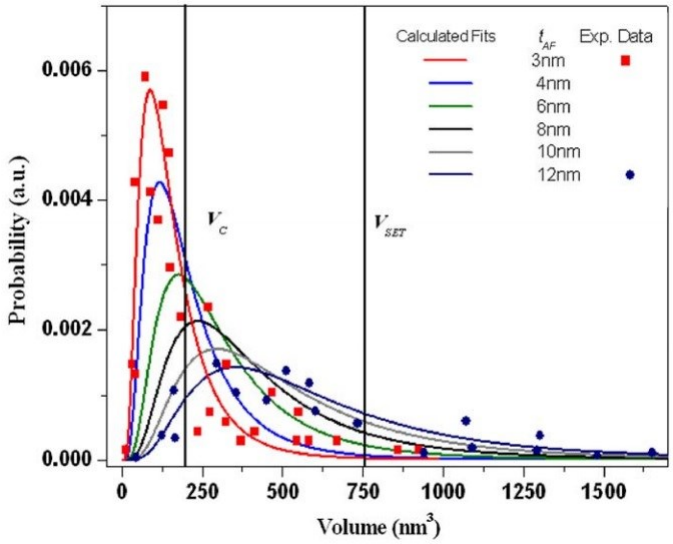

Figure 4.16 Grain volume distributions for varying antiferromagnetic thicknesses [101].

Figure 4.17 shows that the exchange bias can decrease or increase with grain size depending on the thickness of the antiferromagnetic layer. As shown, for antiferromagnet thicknesses in the range 4-6 nm, the value of the measured exchange bias increases with grain diameter. For a thicker antiferromagnet (12 nm) the exchange bias goes through a maximum.

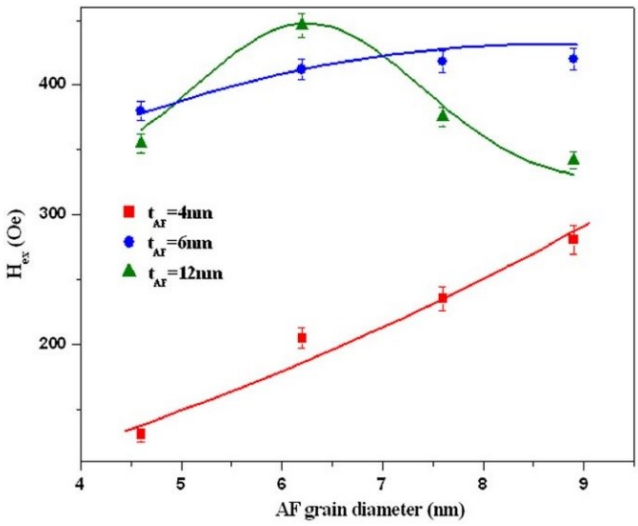

Figure 4.17 Variation of the exchange bias with antiferromagnetic grain diameter [101].

The magnitude of the exchange bias is dictated by the fraction of grains which are in the window shown in figure 4.16. As the anisotropy is constant at the temperature of the measurement then the exchange bias can be expressed as

$$H_{EX} \propto \int_{V_C}^{V_{SET}} f(V)dV \tag{4.22}$$

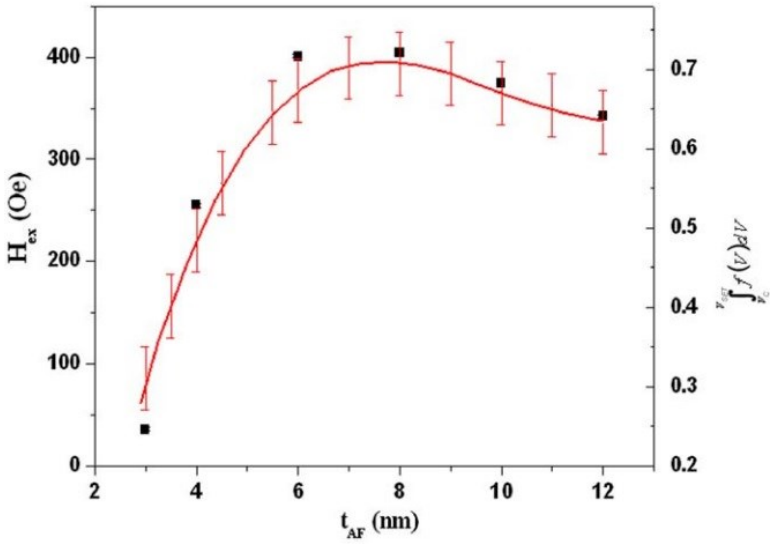

Figure 4.18 Variation of the exchange bias with the thickness of the antiferromagnetic layer and the line of best fit [101].

Figure 4.18 shows the variation of the exchange bias with the thickness of the antiferromagnetic layer. The solid line is the theoretical fit of the data points calculated with equation 4.22. For thicknesses below 6nm a large fraction of the grains are thermally unstable so they do not contribute to the exchange bias. The measured exchange bias will continue to increase with increasing the thickness of the antiferromagnetic layer until the largest possible fraction of the grains is within the interval set by the two critical volumes. If the thickness of the antiferromagnet is increased further the anisotropy barrier KV increases past the point where grains can be set resulting in a reduced number of grains contributing to the exchange bias. Hence, a decrease in the

measured exchange bias is observed. The York Model explains both the grain volume and antiferromagnetic thickness dependence of the exchange bias.

5. Sample Fabrication

5.1. Methods of Thin Film Deposition

Different means exist for depositing thin films in order to control their properties around the nanometre scale. These techniques include evaporation, molecular beam epitaxy or sputtering. The reason sputtering has been chosen for fabricating samples for this work is that sputtering gives better control over magnetic properties than the other techniques. Molecular beam epitaxy (MBE) and pulsed laser deposition (PLD) are two widely spread techniques for material deposition but are not as suitable for magnetic materials as is sputtering [102].

MBE produces single crystal films which require ultra-high vacuum conditions (UHV) and have low deposition rates. Because the films are single crystal the magnetization reversal is governed by the motion of domain walls hence any imperfection in the film (substrate roughness, dislocations) will lead to uncontrollable pinning of the domain walls. PLD has much higher sputtering rates than sputtering and MBE and the deposited materials keep the same stoichiometry as the target (alloy, oxides etc.). The great disadvantage of PLD is the very wide size distribution of the grains which leads to ample non-uniformities in film roughness.

Ion Beam Deposition (IBD) is somewhat similar to MBE but the electron gun is replaced with an ion source. A first consequence is that the deposition cannot take place in an UHV environment as a working gas needs to be inserted in the deposition chamber limiting the pressure to 10^{-5}-10^{-4} mbar. Sputtering is a form of IBD which occurs when a target is bombarded with high energy ions. This leads to values of the deposition rates between those of MBE and PLD (1-10 nm/s). Films

resulting from sputtering are atomically flat and are of high purity polycrystalline materials. This method is widely used in industrial applications and was therefore used for the preparation of the samples produced in this work [57].

5.1.1. Sputter Deposition

Several types of sputtering systems are used for the deposition of thin films. The first system developed was DC diode sputtering. In this system a DC voltage of several kilovolts is applied across a pair of planar electrodes. The deposition chamber contains an Ar^+ atmosphere at a pressure of ~0.1 mbar which leads to the initiation of a glow discharge. The plasma facing side of the cathode is covered with the target material whilst the back of the cathode is water cooled. The Ar ions generated in the glow discharge are accelerated towards the cathode causing sputtering of the target material and deposition onto the substrates which are placed on the anodes [103].

If in the DC sputtering system the metallic target is replaced with an insulator then the discharge cannot maintain itself due to an accumulation of a surface charge of positive ions. The glow discharge can be maintained if the power supply is changed to AC. In an AC diode sputtering system the cathode current density i_s is given by

$$i_s \cong CdV/dt \tag{5.1}$$

where C is the capacitance between the discharge plasma and the target and dV/dt is the time variation of the target surface potential. This shows that by increasing the frequency of the applied voltage a larger cathode current is obtained. The value of frequency used in practice is 13.56 MHz which is why this method is called RF sputtering [103]. It is important to note that the RF electric field increases the

collision probability between the secondary electrons and gas molecules allowing for a decrease in the Ar pressure down to 10^{-3} mbar.

The desire for low pressure sputter deposition led to the development of magnetron sputtering. It was found that cathode sputtering can be enhanced with the use of a strong transverse magnetic field in the range 3-10kOe. The enhancement is due to an increase of the ion density and energy at the cathode surface by an order of magnitude which also leads to an increase in the deposition rate. The increase in the ion density is due to electrons in the plasma spiralling around the magnetic field lines leading to further ionisation events. Ar pressures of 10^{-5}-10^{-3} mbar are required to initiate a glow discharge [103].

The lower pressure meant that the sputtered atoms could travel across the discharge without collision, giving a deposition rate R_{dep} of

$$R_{dep} \cong kW_0/t \tag{5.2}$$

where W_0 is the amount of sputtered particles, $k=1$ or $k=r_a/r_c$ depending on use of a planar or a cylindrical system respectively and r_a and r_c are the anode and cathode radii. The deposition rate of 1-10 nm/s and the possibility of depositing at low pressure has made magnetron sputtering to be the deposition method of choice for industry [103].

However magnetron sputtering has its limitations. If the sputtered target is magnetic then the field lines of the magnetron are confined within the target which leads to the necessity of very thin targets when sputtering from magnetic materials.

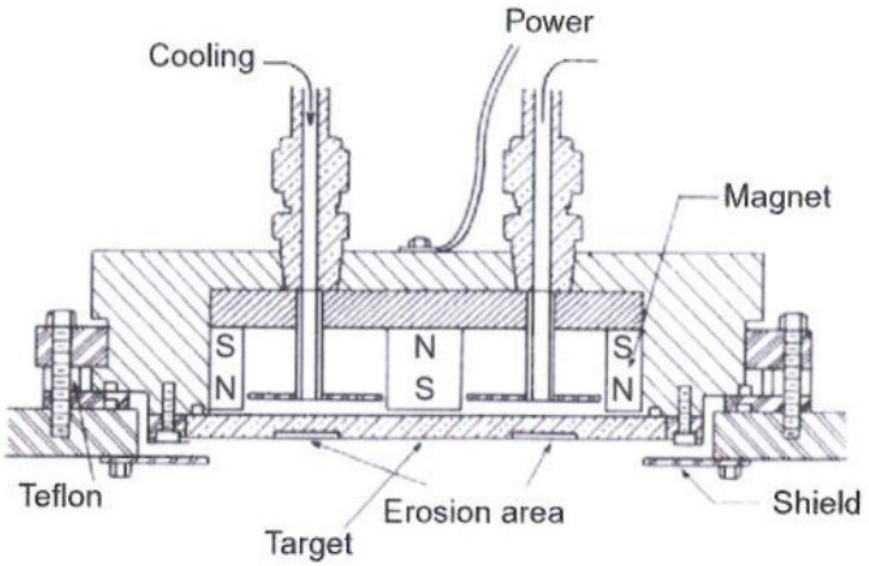

Figure 5.1 Schematic diagram of commercialised magnetron cathodes as produced by Canon Anelva [101].

Another disadvantage is that the glow discharge is concentrated around the high magnetic field region from the cathode magnets. This leads to the creation of a circular discharge and uneven etching of the target. The non-uniform etching of the target material is often referred to as a "racetrack" and limits the lifespan of the target [103]. Hence complex magnet configurations are required to overcome this issue. For this work a system called **Hi**gh **T**arget **U**tilisation **S**puttering has been used, which is a permutation of the magnetron system and will be described in more detail in the next section. Figure 5.2 shows a HiTUS target (a) next to a magnetron target (b).

Figure 5.2 Image of a a) HiTUS target and b) magnetron target.

5.1.2. High Target Utilisation Sputtering (HiTUS) Deposition

There are a number of sputtering technologies used by industry but the most widely used is magnetron sputtering. In magnetron systems the requirement is that the material targets should be placed on the cathode in the region where the plasma is generated. Also the plasma is focused onto the target in a ring shape via a magnetic field which leads to an inefficient use of the target. If the plasma were generated remotely then the sputtering conditions and parameters could be varied regardless of the target composition [57].

HiTUS is an abbreviation and stands for "**Hi**gh **T**arget **U**tilisation **S**puttering" [104]. In HiTUS the plasma is generated in a side arm of the deposition chamber. A three turn radio-frequency antenna surrounds the side arm and ionises the working gas (*Ar*) with a 13.56 MHz RF field. An electromagnet coaxial with the RF antenna applies a 50 Oe field which launches the ions from the antenna region towards the deposition chamber and is called the launch electromagnet. The electrons have enough energy in their chiral motion about the launching electromagnetic field to produce a cascade generation

process, hence creating a “tube” of plasma. The tube of plasma is steered onto the targets by a steering electromagnet placed under the targets which produces a field of about 500 Oe [57].

The HiTUS system does not require a bias voltage for generating the plasma. However the energy of the ions in the plasma is not sufficient to produce sputtering. In order to sputter and control the sputtering process a DC bias of -1 to -1000 V is applied to the target. The field generated accelerates the Ar^{+} towards the target providing them with sufficient energy for sputtering to occur. The plasma density is not affected by the variations in the bias voltage. The plasma density (10^{12} to 10^{14} ions/m^3) can be varied independently of the bias voltage by varying the RF power (up to 2.5 kW) and the working gas pressure (1.3×10^{-3} to 4×10^{-2} mbar). This gives precise control over the deposition rate via the bias voltage for a given plasma density [105]. A schematic of the system is shown in figure 5.3.

The geometry of the system allows for a multitude of substrates and target materials to be used. The distance between the target and the substrates is approximately 30 cm so there is no re-sputtering from the substrates. This large gap also ensures sufficient intermixing of sputtered material so multiple substrates can be sputtered simultaneously with identical material. This allows for sputtering on patterned resist, silicon and carbon-coated copper TEM grids excluding the need for sample thinning for structural characterisation. The large gap between the target and the substrates ensures a low temperature at the substrate surface <100° C.

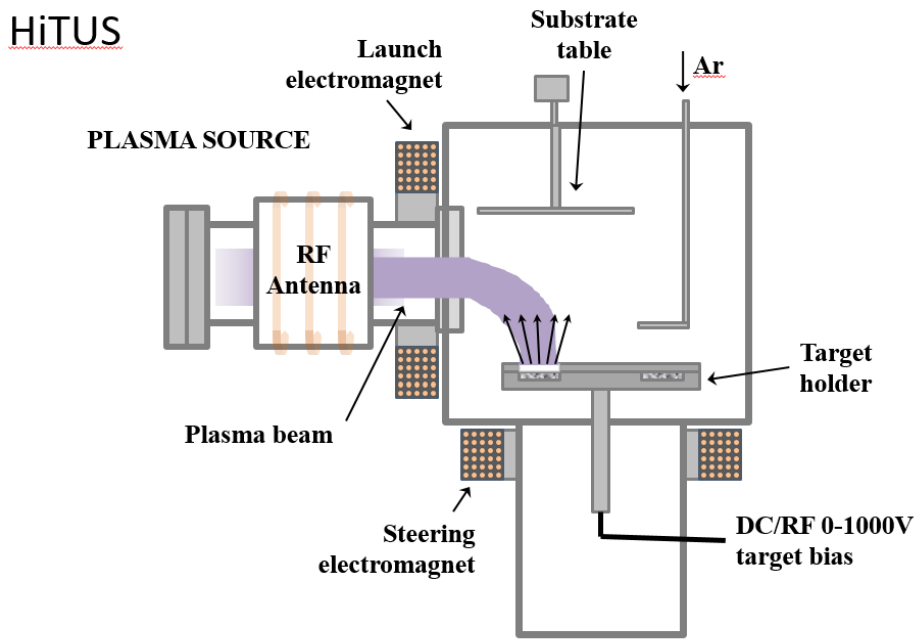

Figure 5.3 Schematic drawing of the High Target Utilisation Sputtering (HiTUS) system.

Other key features of the HiTUS are the target holder which can hold up to 8 different targets. This means that a variety of materials can be sputtered without breaking vacuum. The sample carousel can hold up to six substrates. An image of a sample holder designed to hold a 16 mm ×16 mm substrate and a TEM grid is shown in figure 5.4.

HiTUS has three pumping units which enables it to reach pressures as low as 5×10^{-8} mbar. The layer thickness is measured using a water cooled quartz crystal oscillator growth rate monitor and is placed within 5 cm of the substrate. The thickness is measured to an accuracy of 0.5% [73]. These thicknesses have been confirmed via X-ray Reflectivity (XRR) measurements along with measurements of the interfacial roughness [73].

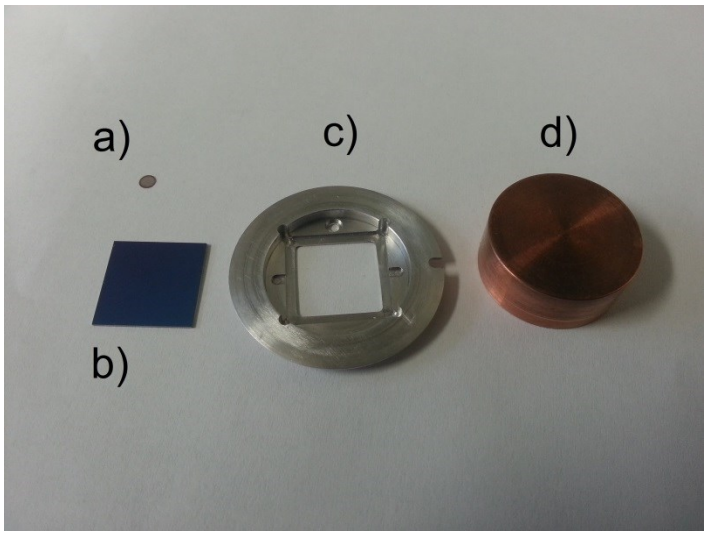

Figure 5.4 a) TEM grid; b) SiO2 substrate; c) sample holder; d) thermostatic Cu lid.

The preferred antiferromagnetic materials for applications in industry should have a high Néel temperature and anisotropy, hence materials like PtMn and IrMn are preferred [106]. CoFe/IrMn systems exhibit very good thermal stability [107], hence these were the materials chosen for the F and AF materials respectively in this study. CoFe has higher magnetocrystalline anisotropy than NiFe and the magnetisation values can be found in [108] so the samples were produced from a $Co_{40}Fe_{60}$ target. The AF layers were sputtered from an $Ir_{25}Mn_{75}$ target. Aley *et al* proved that the exchange field for IrMn/CoFe systems has a maximum plateau between Ir levels between 16 at.% and 20.5 at.% [77]. The exchange field decreases under 50% on either side of the max plateau. Because the Curie temperature of CoFe is much larger than the Néel temperature of IrMn, the properties of the ferromagnetic layer are temperature independent.

5.2. Nanofabrication

5.2.1. The Lithographic Process

Photolithography is an optical means for transferring patterns onto substrates. It is similar to the lithographic printing process and it is the most used patterning method in the semiconductor industry. The first step is the substrate preparation which implies removing any contaminants from its surface. Usual sources of contamination are dust from scribing, atmospheric dust, abrasive particles, lint, solvent stains and residues etc. The lithographic process is usually carried out in a clean room which has its environment well controlled in terms of particle size and density, temperature (±0.1°C), humidity (0.5%), air pressure, flow and composition and lighting spectrum. This work was carried out in two different clean rooms of classes 100 and 10.000 respectively. The numbers give the number of particles of diameter 0.5 μm or larger per cubic foot [109].

There are various methods for cleaning substrates. Contaminants are removed using ultrasonic agitation in different solvents such as acetone, IPA, deionised water etc. After this step substrates are usually dried by spinning, blown dry or baked on a hot plate at 190°C for up to one hour in order to remove any water bound to the substrate. To remove hydrocarbons the substrates are cleaned in hot solvent vapours, by immersion in a mixture of sulphuric acid and hydrogen peroxide or they are placed in an Ultraviolet Ozone (UVO) cleaner. In the UVO the atmospheric oxygen molecules are excited by the UV radiation of wavelength 184.9 nm producing ozone and the ozone is decomposed into atomic oxygen. The atomic oxygen then reacts with the hydrocarbons thus removing them from the substrate.

After the cleaning process the substrate is ready for the resist deposition. In the case of this work spin coating was used for the deposition of the various resist layers and adhesion promoters. In order to ensure best adhesion of the resist to the substrate the substrate receives a coat of primer. The primers or adhesion promoters form bonds with the surface and produce a polar surface. The one used for fabricating samples in this study uses siloxane links (Si-O-Si) and is called 1,1,1,3,3,3-hexamethyldisilizane (HMDS).

The substrate is fixed on the vacuum chuck of the spinner after which the primer is abundantly dispensed onto the substrate. Then the substrate is rotated at 4000 rpm for 30 s. The substrate is then placed on a hot plate at 190°C and baked for one minute. This solidifies the primer. Once the substrate has cooled it is ready for the various coats of resist. The substrate is placed on the vacuum chuck again and spun at 200-500 rpm. In this time the resist is being dispensed onto the substrate. Because it is spinning at a low frequency the liquid resist evenly coats the entire substrate. Once fully covered in resist, the substrate is accelerated to 1500-6000 rpm and spun from 10 s to 3 minutes, depending on the desired resist thickness. The polymer thickness after spinning t_{res} is given by the empirical formula

$$t_{res} = \frac{K_c C^{\beta} \eta^{\gamma}}{\omega^{\alpha}} \tag{5.3}$$

where C is the polymer concentration, η is the intrinsic viscosity and ω the rotation speed of the substrate.

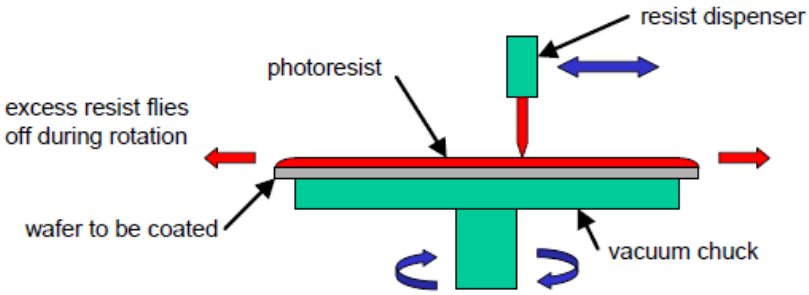

Figure 5.5 Schematic of the spin coating process

After spin coating the resist is "soft baked" at 75-150°C in order to remove solvents and stresses. Now the substrate is ready for the exposure system where the substrate is placed and aligned under a photomask. The mask is usually prepared out of fumed silica with chrome patterns, patterns which are to be transferred to the resist. The entire substrate-mask assembly is exposed with the desired radiation for a length of time required to produce a dose D_e (J/cm^2) which triggers one of two reactions: polymer chain scission or cross-linking. These reactions are the key difference between positive and negative type resists. These reactions are schematically shown in figure 5.6 [109] and will be discussed in the following section.

The next step is the development of the resist. In this step the unpolymerised resist is dissolved by the developer leaving an embossed image which will act as a mask for the following steps, etch or deposition. Positive and negative resists require different types of developer. For positive resists types the developer is usually an aqueous alkaline solution whilst an organic medium is required for the negative resist. Post-bake or hard bake is the final step of the lithography process and it is used to stabilise, harden and smooth the edges of the developed photo resist prior to the processing steps. Post-bake removes any remaining traces of the coating solvent or developer, eliminating the

solvent bubble effects in vacuum processing. A longer or hotter post-bake enhances the material adhesion to the resist.

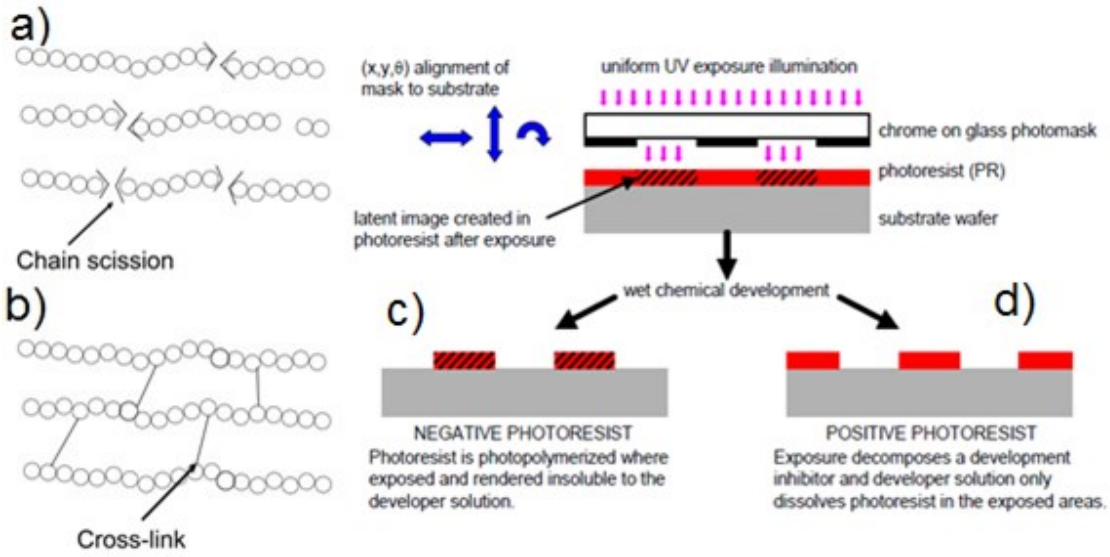

Figure 5.6 Schematic of a) polymer chain scission (positive resist) and b) cross-linking (negative resist) [107]. Schematic of the patterning process for c) negative resist and d) positive resist.

For sample fabrication processes which can be additive, such as deposition, or subtractive, such as etching, two primary techniques exist, lift-off or etch-back, respectively. In lift-off, a patterned layer is deposited on top of the resist and the unwanted material is "lifted off" when the resist is removed. For etching the resist is applied over the top of the layer to be patterned and the unwanted material is etched away.

Etching is the process by which material is removed from a surface. If the removal of material is done via chemical processes or dissolution in a bath of solvent the process is called wet etching. If the process is carried out in a reactive gas then the process is called dry etching. The material to be etched is removed via chemical reaction or via ion bombardment. The resulting material should be volatile so it can be carried out by the gas stream.

5.2.2. Resists

Resists are photosensitive materials that form a relief image after an imaging exposure to light or another radiation source and subsequent development. The resist, be it positive or negative, single layer or double layer, is a major factor in determining the lithographic performance. The name 'resist' comes from its function- it protects the substrate during etching.

The main components of a positive resist are a polymer and a casting solvent. The solvent aids for spreading the resist evenly on the surface of the substrate (spin coating). The polymer is insoluble in aqueous alkaline solutions but the photochemical reaction that occurs during exposure makes the exposed areas soluble in alkaline developers so metal films deposited in the cleared trenches will make the desired structures [109]. The material deposited on the remaining resist is removed during the lift-off process. Lift-off is part of the process when the resist is immersed in a solvent which will dissolve it. Dissolving the resist results in the removal of any material deposited on the resist leaving the desired structure. Figure 5.7 shows an example of failed lift-off.

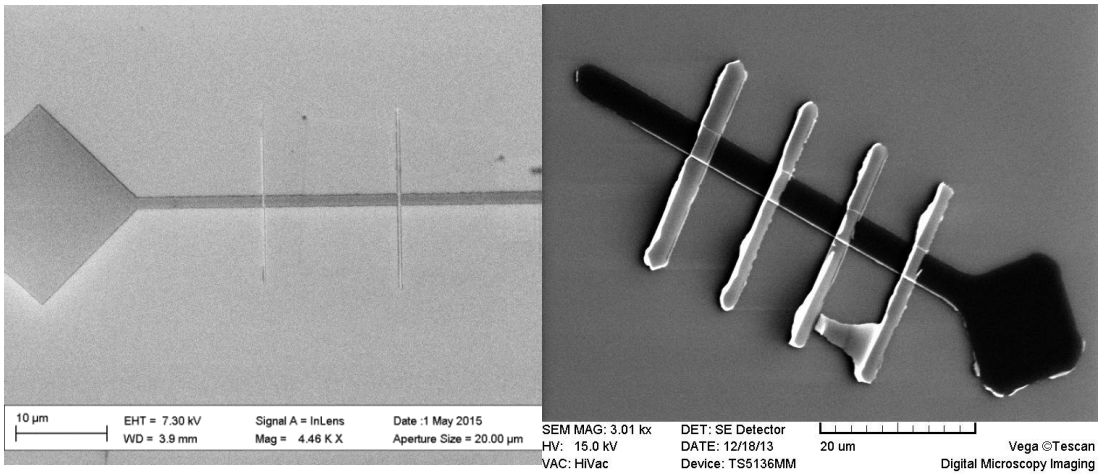

Figure 5.7 Example SEM image of good lift-off (left) on e-beam patterned device and poor lift-off (right) on photolithographically patterned device.

5.2.3. Optical Lithography

Optical lithography has been the most used technique for fabricating semiconductor devices for more than half a century. The principle of photolithography is the same as in photography: optical tools are used to expose patterns on wafers coated in resist.

One of the first optical lithography systems used for device fabrication was the contact mask aligner. As shown in figure 5.8, a resist-coated substrate is placed on a chuck under a 1× mask. A small gap is left between the substrate and the mask for aligning patterns on the mask with the ones on the wafer. After the alignment step, the mask and wafer are put in contact and exposed to light from a mercury lamp.

This system has a very high throughput due to the entire wafer being patterned in a single exposure cycle. Although nowadays resolution for such systems is very good (<50 nm for a SUSS-MJB4), defects may appear in the patterned figures due to the resist sticking to the mask. This type of mask aligner is important as some steps in the sample fabrication for this work have been carried out in such a system.

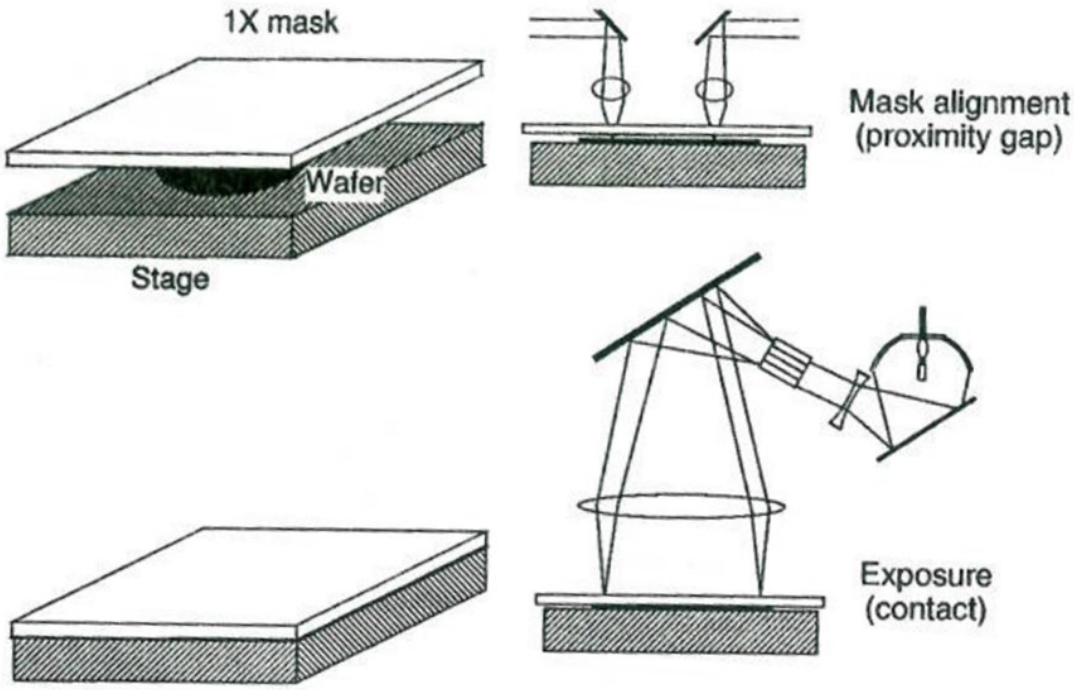

Figure 5.8 Schematic view of the contact mask aligner.

For fabricating samples in this work 16×16 mm silicone oxide substrates were sonicated in an acetone bath and in an isopropanol bath and blown dry with nitrogen. The substrates were then placed in hot acetone and isopropanol vapours. This cycle was repeated 10 times after which the substrates were rinsed in isopropanol and blown dry with nitrogen. The sonication and hot vapour cleaning are meant to remove any organic residues from the substrates. After all organics have been removed the substrates were rinsed in deionised water in order to remove any acetone or isopropanol residues, blown dry with nitrogen and placed on a hot plate at 190°C for 3 minutes in order to evaporate the water.

The substrates were spin coated with 1,1,1,3,3,3 hexamethyldisilazane which is an adhesion promoter at 4000 rpm for 30 s and baked on a hot plate at 190°C for 60 s. After removal from the

hot plate and cooling, the substrates were spin coated with S1805 positive photoresist at 5000 rpm for 60 s and baked at 110°C on a hot plate for 180 s. This gives a resist thickness between 300 and 400 nm.

The mask aligner used to pattern layers on samples which have been used in this work is a SUSS-Microtec MA750 Aligner. It uses a 405 nm Hg lamp and has a maximum resolution of 1 μm. Maximum wafer size is 3 in. and the contact is achieved by a vertical translation of the wafer chuck with a contact force which can be parametrised through the software up to 999 g.

Samples were exposed for times between 3 and 7 s depending on the layer to be patterned at a contact force of 500 g. After exposure, samples were hard baked for 60 s at 110°C and developed for 90s in MF-319 which contains 2.5% tetramethyl-ammonium hydroxide. After 90 s development time the patterned substrates were rinsed in deionised water and blown dry with nitrogen to be ready for deposition.

5.2.4. Electron Beam Lithography

Electron beam or e-beam lithography is a means of patterning resists using a beam of electrons. The apparatus used for e-beam lithography is very similar to a Scanning Electron Microscope (SEM) and consists of a beam of electrons with a given diameter and current being scanned in a raster across the resist to be patterned exposing areas as programmed in the computer aided design tool.

The most widely used e-beam lithography systems have a Gaussian profile beam. A Gaussian e-beam apparatus has a basic and simple optical column. It is mostly used for fine-pattern lithography (<100 nm), fabrication of small quantities of devices or in preproduction

and the development of quantum devices. The problems in the nanometre scale are to obtain the smallest spot size and to have a beam that is as stable as possible.

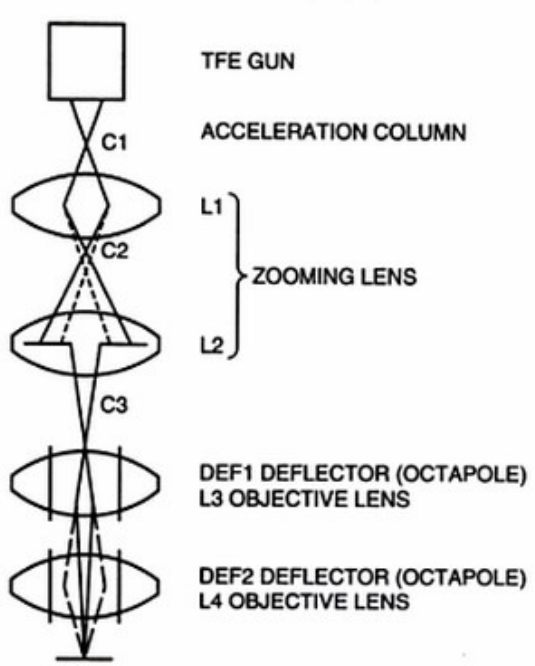

Figure 5.9 Schematic diagram of the electron optics of the JEOL JBX-6000FS.

In order to achieve the needs of a versatile e-beam system thermal field emitters (TFE) are used. They are composed of a tungsten needle covered in Zr/O to reduce the height of the Schottky barrier. They usually operate at around 1500 K in order to activate the emitter surface.

A diagram and a cross-section of a JEOL JBX-6000 series e-beam system are shown in figures 5.10 and 5.11 respectively. Devices fabricated for this work have been produced using a JEOL JBX-6300 series. Specifications of the 6300 model are listed in table 5.1.

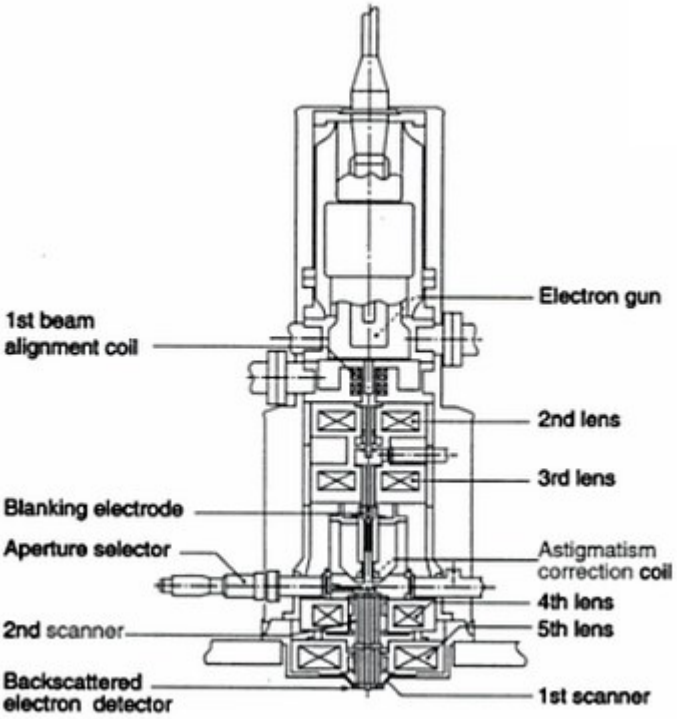

Figure 5.10 Schematic cross section of beam-optics column for JEOL JBX-6000FS.

Electron source	*ZrO/W (Schottky)*
Gun pressure	*~10^{-10} Torr*
Accelerating voltage	*100kV*
Spot size	*2nm*
Scan rate	*50MHz*
DAC resolution	*19bit*
Write field	*1µm*
Writing	*Step and scan writing*
Curved substrate writing capability	*Yes*
Stitching accuracy	*<10nm*
Overlay accuracy	*<10nm*
Maximum wafer diameter	*200mm (8in)*

Table 5.2 Specifications of electron-beam exposure system JEOL JBX-6300FS.

The total exposure time t_{exp} for a given area A_{exp} on the substrate is given by

$$t_{exp} = \frac{QA_{exp}}{I} \tag{5.4}$$

where I is the beam current and Q is the charge density or dose (D_e). Because scanning the exposed area is very time consuming the exposure time is required to be as short as possible so by knowing the half angle of the beam a_b and the spot size d_s the current I can be calculated using

$$I = \beta_s \frac{\pi d_s^2}{4} \pi \alpha_b^2 \tag{5.5}$$

where β_s is the brightness of the source. For a typical array of wire devices used in this work (3 devices/slot × 9 slots), the exposure time is of the order of one hour.

A unique feature of the e-beam lithography is the proximity effect. The proximity effect consists of exposure of the resist by the electrons backscattered from the substrate. This leads to an increase in the exposed area which then leads to larger features than expected. Corrections are being applied so that the centre of the feature will receive a maximum dose and it will decrease towards the edges. This is done by varying the beam current depending on the exposed area [109,110].

The exposure cycle of an e-beam lithography machine is intrinsically slow due to the scanning in a raster of the sample. Optical mask aligners with near field optics which are currently used in industry for mass production have much smaller exposure times (10 s-1 min). Another advantage is that in a single exposure cycle an entire wafer is exposed. The e-beam is a very powerful research tool because unlike the optical mask aligners it does not require a physical mask to

be made beforehand and so sample design alterations are much easier to make.

6. Experimental Techniques

6.1. Structural Characterisation

6.1.1. Transmission Electron Microscopy

Light microscopes have a maximum resolution limited to 200 nm even using near field optics due to the wavelength of the light. In order to image smaller structures, electrons have been the means of choice because of their considerably shorter wavelength. Electrons can also be used as an ionising radiation which can excite or remove tightly bound electrons from the inner shells of atoms. Electrons diffract due to wave-particle duality which makes them useful for evaluating crystallographic and elemental analysis.

Unlike optical microscopes, electron microscopes have two main sources of contrast: mass-thickness and diffraction [111,112]. Mass-thickness contrast is due to scattering of the electrons by the nuclei (Rutherford scattering) so sample thickness and proton number Z determine the number of electrons that are scattered. This type of contrast was dismissed for this work because the materials used in this work are *3d* metals and the thickness was under 10 nm. Iridium has an atomic number of 77 but its concentration in $IrMn_3$ is low at 20-25% so negligible in mass-thickness contrast [112].

In polycrystalline materials, the electrons can diffract and interfere constructively or destructively in certain directions [111,112]. The specific Bragg diffraction angle θ_B can then be expressed from the Bragg condition

$$n\lambda_e = 2dsin\theta_B \tag{6.1}$$

where λ_e is the wavelength of the incident electrons and d is the lattice spacing. The electrons are scattered by the electron clouds of the atoms and molecules of the sample in an elastic and inelastic manner. Energy

is lost in inelastic collisions depending on the atomic number of the atom which allows for elemental analysis. The elastically scattered electrons provide the two types of contrast. In the TEM the transmitted and elastically scattered electrons help form the image [111].

For this work a JEOL 2011 TEM was used. It creates electrons via thermionic emission from a LaB_6 filament in the form of a ~1 μm diameter tip. The electrons are in a 10^{-10} mbar vacuum and accelerated towards the sample via an electric field. A series of electric and magnetic fields form lenses which are used to focus the fascicle on the sample. After the electrons interact with the sample they are focused by the objective lenses to form an intermediate image and then pass a second lens system which forms the image on a fluorescent screen or a CCD camera. Figure 6.1 shows a schematic of a TEM.

Similar to optical microscopes, the TEM uses lenses and apertures to create an image. The lenses are electromagnetic and are usually a copper coil wound around the optical axis of the microscope. The field from the lenses is focused with iron yokes and pole pieces for the lenses to act as “thin lenses”. The force exerted on an electron can be expressed

$$F = evBsin\theta \tag{6.2}$$

where v is the velocity of the electron in the magnetic field B. This makes the lenses act as converging lenses so that electrons that travel through the optical axis will not feel a force. The force is perpendicular to both v and B and act to reduce the radius of the helical motion of the electron around the optical axis. This allows for the magnification and focus of the microscope to be easily adjusted by varying the current through the lenses.

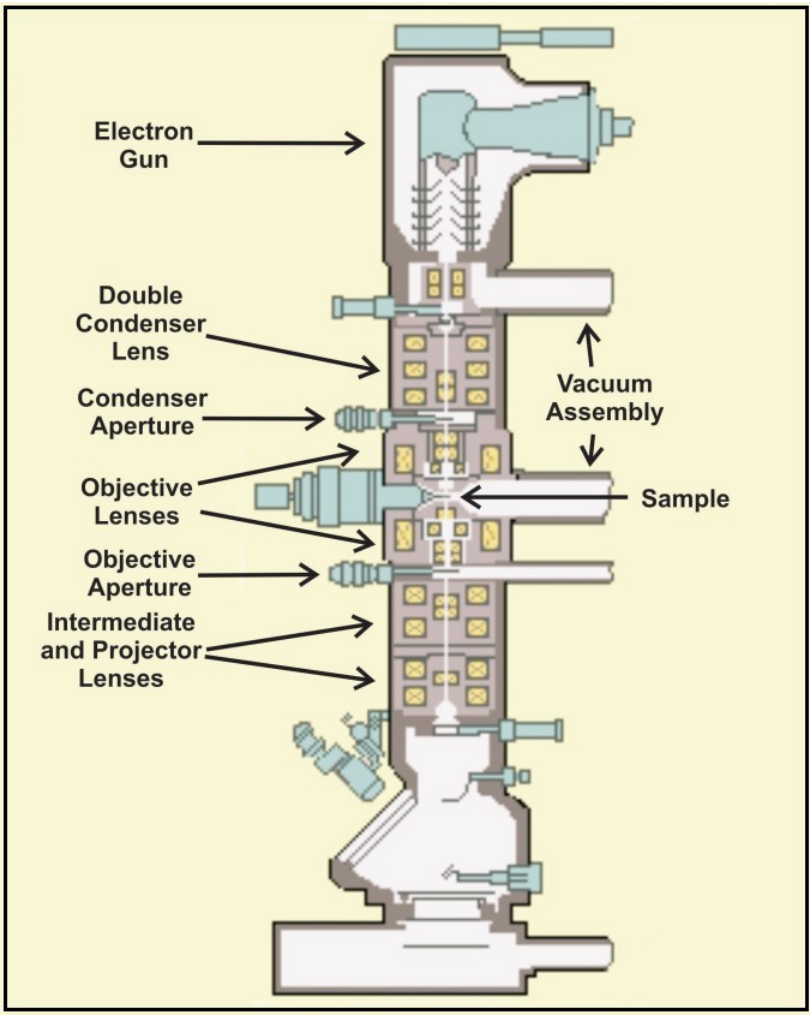

Figure 6.1 Schematic of a TEM column with optics.

The microscope can operate in two modes: selected area diffraction and imaging. The operating mode can be changed by changing the position of the objective aperture or by tilting the beam. A key example of this is Bright Field (BF) and Dark Field (DF) imaging. With the objective aperture, the imaged electrons can be either the ones transmitted or the ones diffracted by the sample. Figure 6.2 shows a schematic of the two operating modes as well as the difference in image between the two. The BF or DF operation mode allows for different information about the sample to be accessed as different electrons (transmitted or diffracted) allow for different crystal planes to be imaged [112].

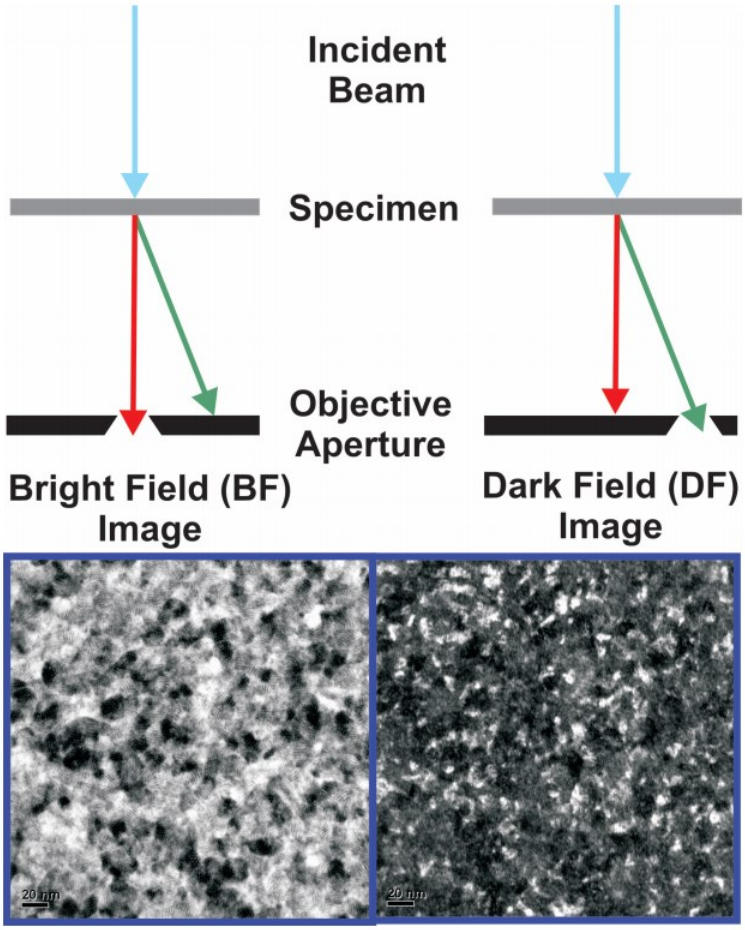

Figure 6.2 Schematic of the objective aperture setup for bright field and dark field imaging with example images of the same are in the respective modes [113].

For this study the JEOL 2011 TEM was used to obtain bright field images of the samples. Carbon-coated copper TEM grids were deposited at the same time as the magnetic samples as described in section 5.1 and the images were used to obtain the grain size distributions as described in section 6.1.3. Figure 6.3 shows an example of such an image. Several images from different areas of the sample were taken. Grains that appear black satisfy the Bragg condition and it is those grains which have been counted for the grain size distribution.

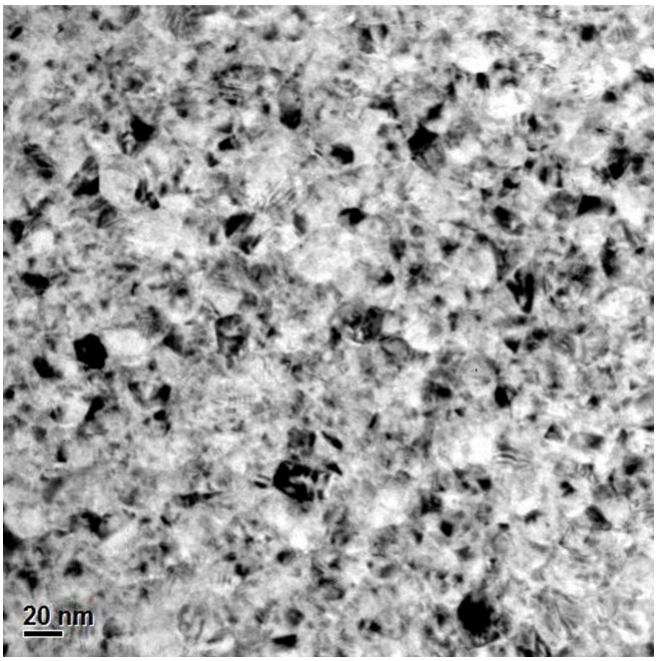

Figure 6.3 TEM bright field image.

6.1.2. Scanning Electron Microscope

In a Scanning Electron Microscope (SEM) the images are formed with the help of the inelastically scattered electrons. They are scattered from the sample surface generating secondary electrons, X-rays or photons, which is why several detectors can be found on a SEM.

The electrons are being produced and controlled as in a TEM column. Instead of passing through the sample they are focused into a spot which is scanned in a raster across the sample. Usually two sets of coils are being used to deflect the electrons with the pivot point contained on the optical axis to reduce lens aberrations. The resolution of the SEM is dictated by the size of the spot. The diameter of the incident electron fascicle is controlled with a double condenser lens system. The first condenser lens acts as a convergent lens with light and reduces the size of the beam. The second condenser lens or the focus lens is used to ensure that the minimum spot size is obtained at

the sample surface. Fine adjustments can be made using the sample height and the second condenser lens. For this study the working distance was 5 mm in order to obtain the smallest possible spot. A schematic of an SEM and the beam path are shown in figure 6.4 [111].

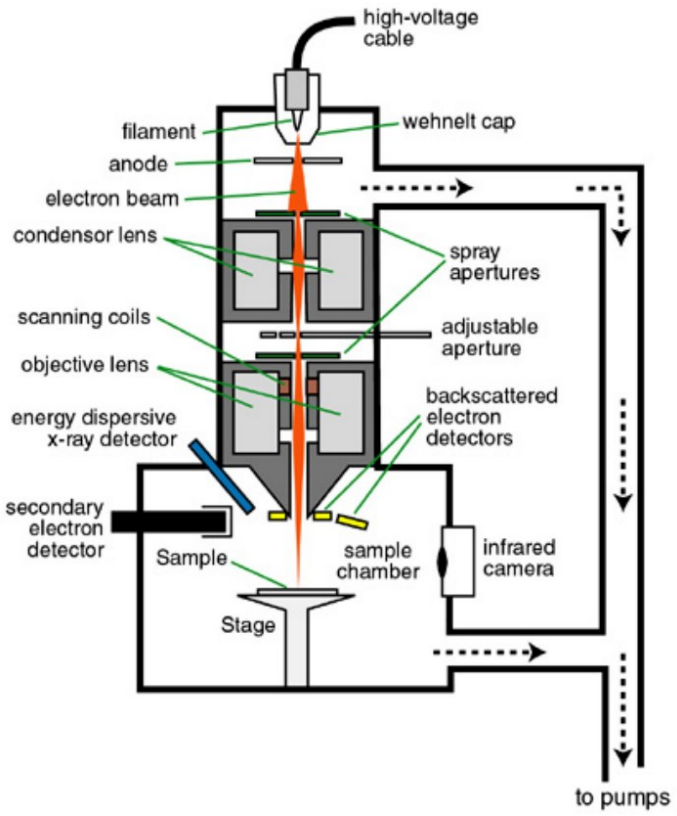

Figure 6.4 Schematic of the beam path in an SEM [114].

6.1.3. Measurement of the Grain Volume Distribution

As previously discussed, the materials used in this work are polycrystalline. The grain volume distribution is of great importance for magnetic systems as it dictates their behaviour [115]. Due to the deposition processes the grains follow a log-normal distribution defined as

$$f(D)dD = \frac{1}{(\sqrt{2\pi})\sigma D} exp\left[-\frac{(lnD-\mu)^2}{2\sigma^2}\right] dD \quad (6.3)$$

where D is the particle diameter and μ and σ are the mean and standard deviation of ln$D$ respectively [116]. For a given number n of measured diameters, σ is expressed as

$$\sigma = \sqrt{\frac{1}{n}\sum(lnD)^2 - \left(\frac{1}{n}\sum lnD\right)^2} \quad (6.4)$$

And the mean diameter D_m is

$$D_m = e^{\mu} \quad (6.5)$$

In order to measure the grain diameter bright field images of the sample are taken using the JEOL 2011 TEM described in section 6.1.1. After optimising the diffraction contrast, the grains that satisfy the Bragg condition appear black. It is these grains that are measured for the grain diameter. The measurement is performed by matching a circle of known diameter to the grain so that their areas are equal. The diameter of the circle is measured and the grain recorded to prevent a repeat measurement. The measured diameters are sorted in a 20-40 bin histogram depending on σ and then plotted. The lognormal distribution is calculated using equations 6.3, 6.4 and 6.5 and plotted against the measured diameters. For good statistics, a minimum of 500 grains are measured [116]. Figure 6.5 shows an example of this measurement with the calculated lognormal distribution and a bright field TEM image of the sample.

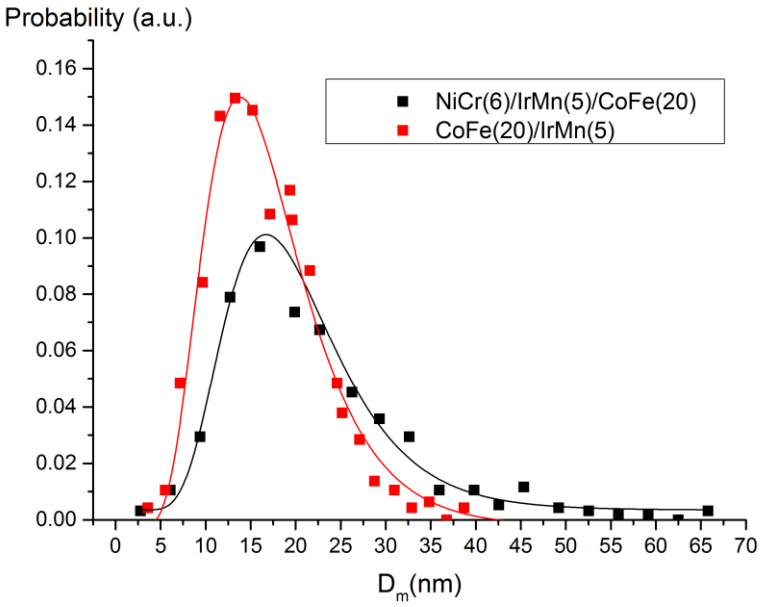

Figure 6.5 Grain size distributions with lines of best fit.

6.2 Magnetic Characterisation

6.2.1. Alternating Gradient Force Magnetometer

The Alternating Gradient Force Magnetometer (AGFM) is an apparatus which is sensitive to the force exerted (F_M) on a magnetic sample when it is placed in a uniform magnetic field gradient.

In an AGFM the sample is mounted on a sample probe in order to convert the force felt by the sample into an electrical signal. The AGFM sample is formed of a square quartz glass sample holder mounted on two parallel quartz rods. The quartz rods are fixed to opposing faces of a strip of piezoelectric bimorph. The force exerted on the magnetic sample will act to move the quartz rods and stress the piezoelectric bimorph transforming the mechanical movement of the sample into an electric signal and is expressed by

$$\bar{F}_M = \bar{m} \cdot \nabla \bar{H} \qquad (6.6)$$

where F_M is the force, m the moment and ∇H is the field gradient.

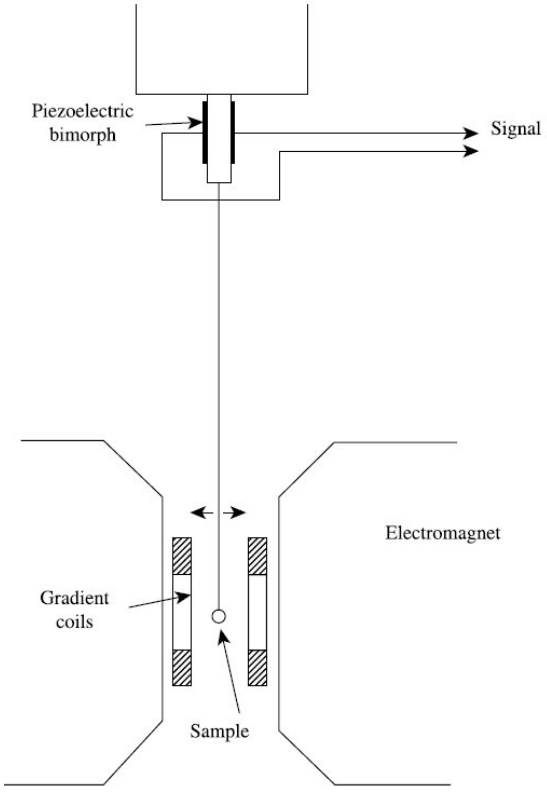

Figure 6.6 Schematic diagram of an alternating gradient force magnetometer.

The sample probe holds the sample between the two pairs of coils of the AGFM: the gradient coils and the electromagnet coils. The gradient coils are responsible for generating the magnetic field gradient that acts on the sample while the electromagnet applies a uniform magnetic field.

The amplitude of the movement of the sample can be enhanced if the field gradient is applied with a frequency as close to the resonant frequency of the sample-probe assembly as possible. This results in an increase of the amplitude by a factor Q (the quality factor of the oscillator)

$$Q \approx 0.3\left(\frac{d^3}{\eta l^2}\right)(\rho Y)^{\frac{1}{2}} \quad (6.7)$$

where η the dynamic viscosity of air, l the rod length, d the rod diameter, ρ the rod density, and Y is Young's modulus.

Using an alternating gradient is more advantageous not only for tuning to the resonant frequency of the system, usually between 100 Hz and 1000 Hz but also as it enables the use of lock-in detection. The noise base of such a magnetometer easily reaches 10^{-8} emu and has a very fast acquisition time of about 2 minutes for a hysteresis curve from 1000 to -1000 Oe in 10 Oe steps [117,118].

The AGFM also has limitations which arise from its design. Small movements of the sample on the probe cause a change in the resonant frequency of the system and drift in the measurement. This also limits the AGFM's capability to do temperature dependent measurements [118]. Because the sample vibrates in air, any acoustic signal can perturb the measurement and cause drift and spikes in the measured signal. The field gradient is also problematic when performing measurements with the AGFM as it leads to discrepancies in the coercive field. For a 5mm sample and a 1 Oe/mm field gradient there will be a 5Oe difference in applied field across the sample. These errors can be overcome by using a smaller field gradient 0.1 Oe/mm but this leads to a decrease in F_m so a decrease in measured signal. In this work, a 0.1 Oe/mm gradient was considered optimal. Overall the AGFM is a versatile and quick tool which can be used together with a VSM for in depth characterization.

6.2.2. Vibrating Sample Magnetometer

A vibrating sample magnetometer or VSM is an instrument which measures the magnetisation of a sample (***M***) as a function of an applied field (***H***). This is achieved by the use of Faraday's law of induction where

a sample magnetised by an external magnetic field is vibrated between a pair of detection coils and measured the induced voltage. This occurs due to the time variation of the magnetic flux through the coils. The total flux (φ_F) passing through the coils of area A_c at any time is given by

$$\varphi_F = B_m \cdot A_c = (H + M) \cdot A_c \tag{6.8}$$

where B_m is the flux density, H is the external applied field and M is the magnetisation of the sample. The emf (ε) induced by the flux variation is

$$\varepsilon = -N \frac{d\varphi_F}{dt} \tag{6.9}$$

where N is the number of turns in the detection coil and $d\varphi_F/dt$ is the rate of change of the flux in time. By substituting equation 6.8 in 6.9 and integrating over time the induced voltage becomes

$$\int \varepsilon \cdot dt = -NA_c \cdot M \tag{6.10}$$

As H does not vary with respect to the detection coils, only M will contribute to $\int \varepsilon \cdot dt$.

A particular characteristic of the VSM is that it measures the moment of the sample, *m.* For accurate measurements, both the applied field H and the moment m need to be calibrated on a regular basis. The field calibration is done by comparison with two reference points. The first point is in zero field. This is achieved by placing the gauss probe of the VSM in a zero field shield to establish the zero point. The second reference point is measured and corrected by comparison to a secondary standard Bell 9900 Gaussmeter.

For calibrating the moment (m) a material with a very well-known moment needs to be used which does not deteriorate and keeps its magnetic properties in time. The material of choice is palladium which is a Pauli paramagnet and has a defined moment at any applied field [119]. This allows for errors in m to be reduced to the error in the

applied field. Calibration is done by placing a calibration sample of the same shape and size as the samples to be measured because of the shape dependence of the demagnetising field and the geometric response from the coils. In the case of this work, a 5 mm x 5 mm square palladium foil of known mass is placed on the VSM probe. The VSM probe is a quartz glass rod which prior to the calibration has been cleaned for 30 minutes in 1% hydrochloric acid. The probe with the sample is then placed in the VSM and centred between the coils. The field is ramped up to 10 kOe and the moment of the palladium sample entered in the software of the VSM. For the measurements presented in this thesis a calibration sample of palladium with a calibration constant of 3.877×10^{-7} emu/Oe has been used.

The limitation in sensitivity of VSM measurements is electronic noise from induction effects detected by the coils. This can be increased by filtering, averaging and extending the time constant. Digital Signal Processing was used to obtain a signal hidden in noise. The detection coils are very sensitive to flux variations so any additional vibration of the coil or the sample has a detrimental effect on the measurement. This is firstly corrected by the use of coil pairs connected anti-parallel so that any flux change equally present in both coils will be removed. In order to eliminate other sources of noise the vibrating head contains another set of detection coils with a reference sample. This is used to reference the parameters of the vibrating head – frequency, phase, amplitude - and making the measurement independent of any other sources of vibration, variations in the frequency of the vibrating head and magnetic field non-uniformity.

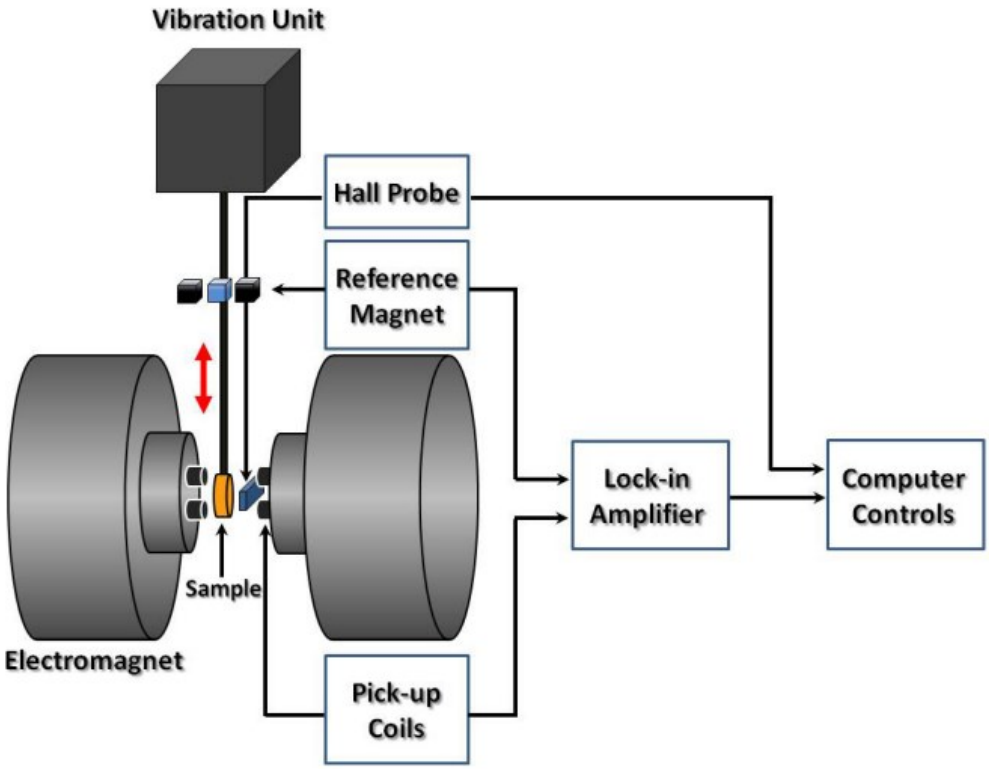

Figure 6.7 Schematic diagram of the vibrating sample magnetometer.

The VSM used in this study is an ADE Model 10. This is a vector magnetometer where the detection coils are linked to the position of the sample and the magnet is rotated around the detection coil setup [120]. Eight coils grouped in pairs are placed orthogonal to ensure equal sensitivity for the sets of coils. It enables vector measurements for up to 20 kOe and scalar measurements to up to 30 kOe. The noise resolution is 10^{-6} emu. Field resolution is 1% for 1 kOe and 0.1% for 10 kOe. The system is fitted with a continuous flow cryostat which allows for temperature control better than 0.5 K/hour for temperatures in the range 100 K to 500 K. For heating up the sample, a flow of heated nitrogen is used to prevent the sample from oxidising. Cooling is possible by passing the nitrogen through a transfer line submerged in liquid nitrogen.

6.2.3. The York Measurement Protocol

There are two ways for direct characterisation of antiferromagnets, one via Néel temperature measurements but the signal from antiferromagnetic materials disappears as the material is reduced to a thin film and a second method which uses neutron scattering but is a very long lasting measurement. The York measurement protocol is a measurement procedure developed by Fernandez-Outon *et al.* [81] in order to obtain reproducible measurements of hysteresis for exchange bias samples. In order to achieve relevant, comparable and reproducible results all samples need to be in a known state before every measurement.

The issues with characterising antiferromagnets arise from the fact that antiferromagnets cannot respond macroscopically to applied fields. However, an antiferromagnetic material can respond to the exchange field from a ferromagnet and because it is a corresponding interaction, any change occurring in the antiferromagnet can then be sensed and characterised by characterising the ferromagnet.

The York protocol uses the exchange interaction between the ferromagnet and antiferromagnet to erase the previous magnetic history of the samples and to set them in the same state prior to a measurement. During the setting process the antiferromagnet can be ordered by applying a magnetic field to saturate the ferromagnetic layer. This results in an exchange field acting on the antiferromagnet. Heating to a temperature in principle, close to the Néel temperature of the antiferromagnet, T_N, but below the Curie temperature of the ferromagnet, T_C, and cooling the sample in the presence of the field aligns the antiferromagnet in the direction of the ferromagnetic layer.

Below the Néel temperature the antiferromagnet is set with the spins exchange coupled across the interface.

However, the Néel temperature for some materials such as IrMn, which has been used in this work, is very high (~700 K) and heating to this temperature will result in morphological damage to the samples [121]. Hence the method used in practice is setting via thermal activation. During thermal activation the sample is heated to a temperature T_{SET} ($<T_N$) while applying a saturating magnetic field. Keeping the sample in these conditions for a period of time, t_{SET}, the antiferromagnet is ordered due to the exchange field from the ferromagnet.

Figure 6.8 shows the increase in exchange bias, H_{EX}, with increasing setting time. The measurement clearly shows a logarithmic relationship and the rate at which H_{EX} increases is reduced with the increase of the setting time. The vast majority of the antiferromagnetic grains are set after 90 minutes and no measureable increase in H_{EX} is observed after a further increase in setting time.

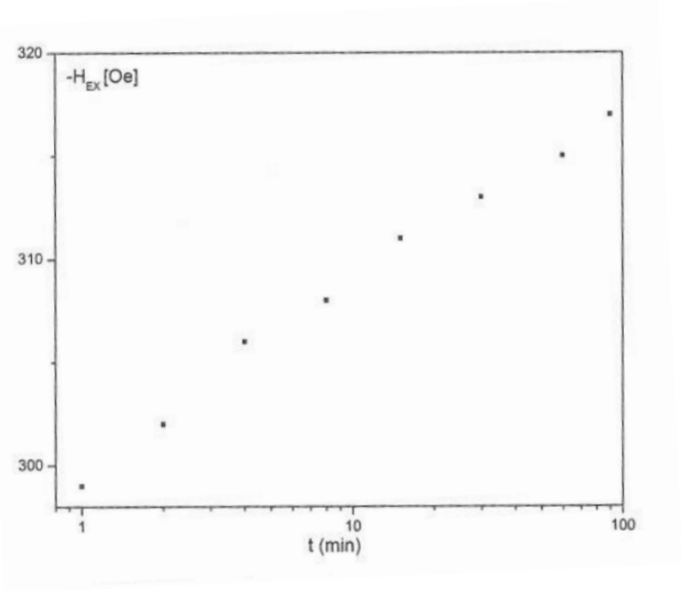

Figure 6.8 Setting time vs exchange bias on a logarithmic scale [33].

To determine the conditions at which a sample is set the following procedure is carried out: the sample is placed in a magnetic field to saturate the ferromagnetic layer and heated at systematically increased temperatures. The sample is kept at 225°C for 90 minutes after which the temperature is decreased to the measuring temperature. At the point where an increase in temperature does not result in an increase in the measured exchange bias, H_{EX}, the sample is considered to be fully set.

Another important parameter for samples in the York protocol is the temperature at which a sample is thermally stable. In order to determine this temperature the sample is set at T_{SET} as described above and cooled down to a specific temperature where the sample is measured. Then the sample is set again in the same conditions and cooled down to the same temperature as before. A negative saturating field is applied for 30 minutes and the sample is measured again. If the two curves superimpose then the antiferromagnet is thermally stable. If the two curves do not superimpose then the same procedure needs to be applied but T_{SET} needs to be lowered until the two measurements give the same hysteresis loop and the temperature at which the sample is thermally stable is found. This temperature is called temperature of no thermal activation, T_{NA}. A schematic of the York Protocol measurement sequence is shown in figure 6.9.

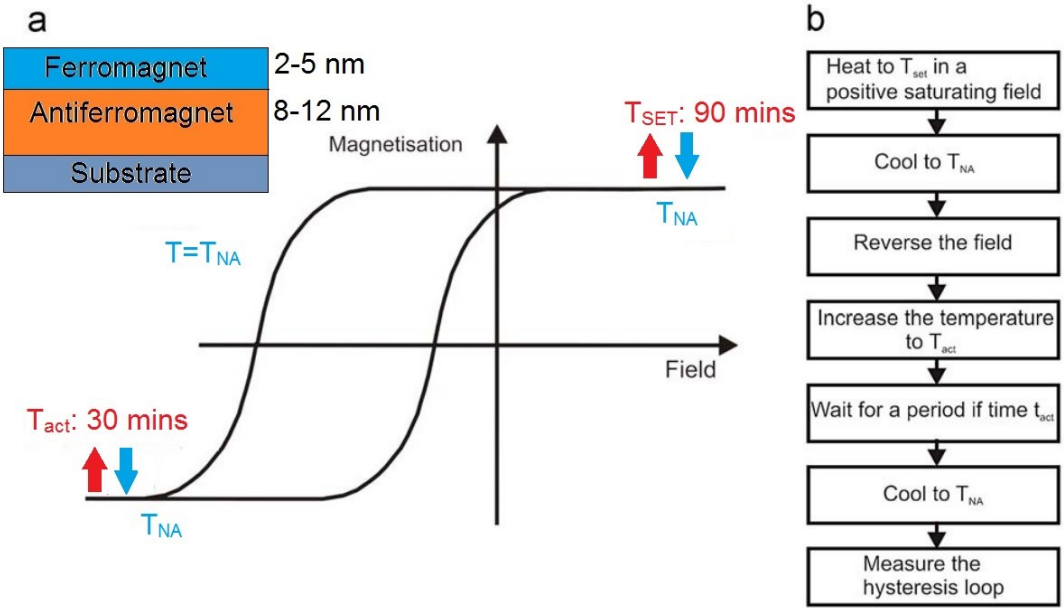

Figure 6.9 (a) Schematic diagram and (b) measurements steps of the York Protocol [13].

6.2.4. MOKE Magnetometer

The magneto-optic Kerr effect (MOKE) is a very useful technique for characterising magnetic materials at the "nano" scale and in thin films or nanostructures. It is a surface sensitive technique which does not require any special sample preparation.

The Kerr effect was discovered by John Kerr in 1877 [122,123]. It originates from the spin imbalance in the *3d* band of ferromagnetic materials. The spin imbalance is observed as a difference in absorption of opposite optical circular polarisations - magnetic circular dichroism (MCD). In practical terms, this means that circularly polarised light interacts more strongly with electrons in a solid with a spin along one direction of the optical axis than the other. Figure 6.10 illustrates this effect. A more in depth description of the Kerr effect theory and all the derivations have been published by Qiu *et.al* and Weinberger [124,125].

The full comprehensive description of the Kerr effect in ferromagnets can be found in an article by Argyres [126].

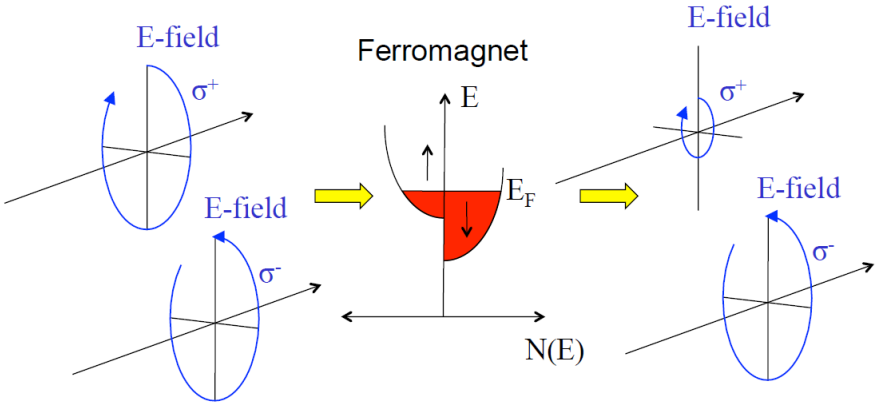

Figure 6.10 Illustration of the Kerr effect.

Depending on the orientation of the magnetisation there are three main types of MOKE magnetometer configurations: polar, longitudinal and transverse. The MOKE polar configuration is used for dealing with out-of-plane magnetisation, longitudinal configuration is used for dealing with magnetisation in the plane of the surface and in the optical plane of incidence and the transverse configuration is used for the in-plane magnetisation which is perpendicular to the plane of incidence. The MOKE magnetometer described and used in this work was set up in the longitudinal configuration.

The longitudinal Kerr effect uses either *s*- or *p*-polarised incident light. If the incident light is *p*-polarised then an *s*-polarised electric component is created post reflection in addition to the standard "Fresnel" reflection which results in a rotation of the overall polarisation. If the light is *s*-polarised then the electric field component created due to the reflection will be *p*-polarised. A schematic diagram of the longitudinal Kerr effect is presented in figure 6.11.

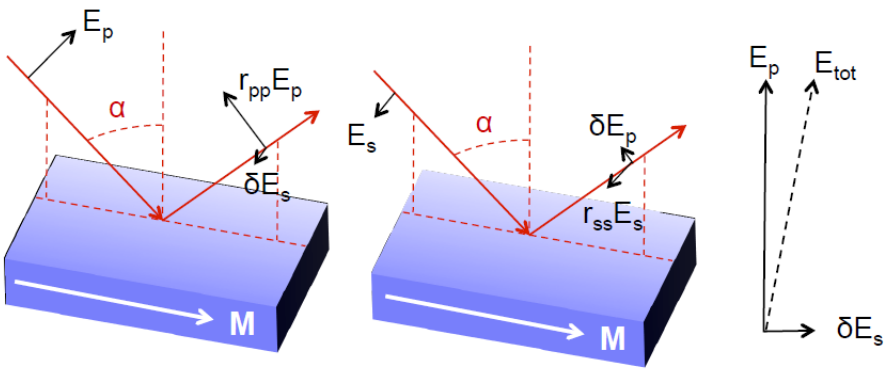

Figure 6.11 Schematic diagram of the longitudinal Kerr effect.

Figure 6.12 a) shows a schematic of a very simple MOKE system. Figure 6.12 b) shows a more detailed schematic of the system used for this work. The light source is a Coherent Verdi class 4 continuous wave laser with a wavelength of 532 nm and tuneable power up to 2.2 W. The optical path includes a quarter-wave plate (λ/4 plate) between the analyser and the detector to convert elliptical polarisation to linear polarisation thus maximizing the Kerr signal. This also aids in measuring the reflected linear and circularly polarised components. In order to focus the laser beam on the desired area of the sample and to localise nanostructures a white light source was also added to the system with a camera.

The sample is mounted at a 45° angle with the incident beam in the system on a 3 axis precision stage (x, y and θ) with a position resolution of 0.1 μm. The sample was carefully positioned using the stage in the centre of a cross-hair-shaped electromagnet capable of applying AC fields in the X and Y directions of the plane of the sample. Because the electromagnet cannot be cooled the maximum field it can generate is ~500 Oe at 27 Hz or at 270 Hz for short periods of time (<5min).

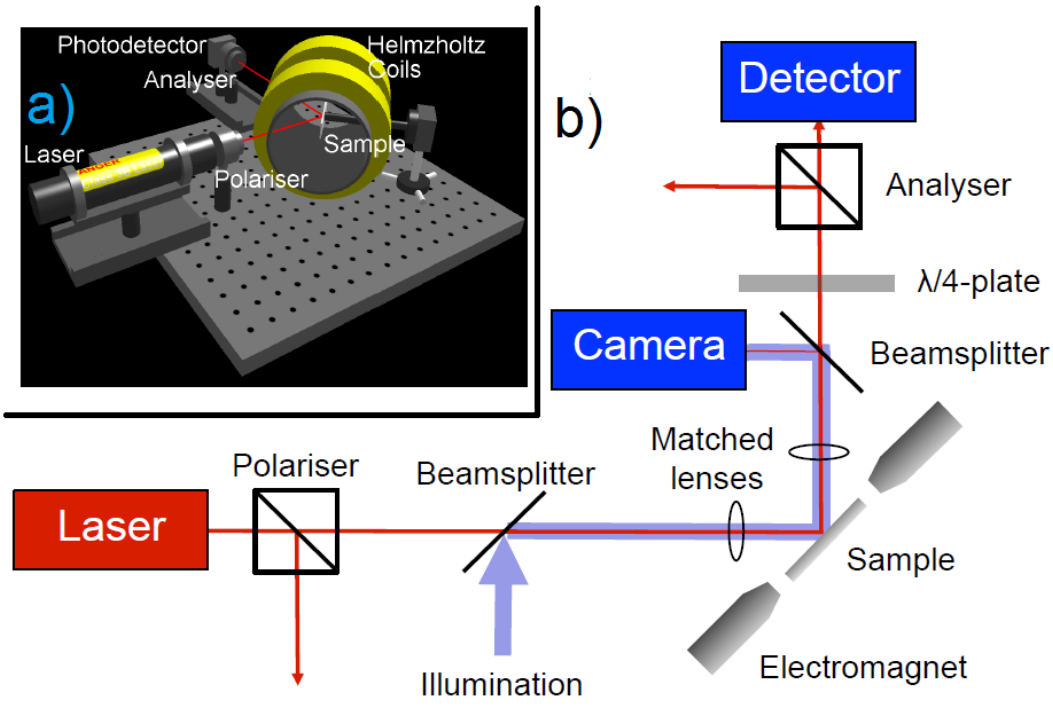

Figure 6.12 Schematic diagrams of a simple MOKE system for thin films (a) and a system suitable for nanostructures (b).

The spatial resolution of the MOKE is limited by the laser spot size which is <5μm. A unique feature of the MOKE is that it can measure structures which are smaller than the spot size. Magnetic maps of the samples can be traced by moving the sample stage in a raster. The MOKE is a very sensitive apparatus being able to detect changes in the signal intensity due to the rotation of the polarisation down to 1-5% for thin films and 0.01-0.05% for nanostructures. It is also capable of measuring single magnetisation reversal events in individual nanowires. Figure 6.13 shows the hysteresis curve of a single event and an average of the same event over 100 transitions.

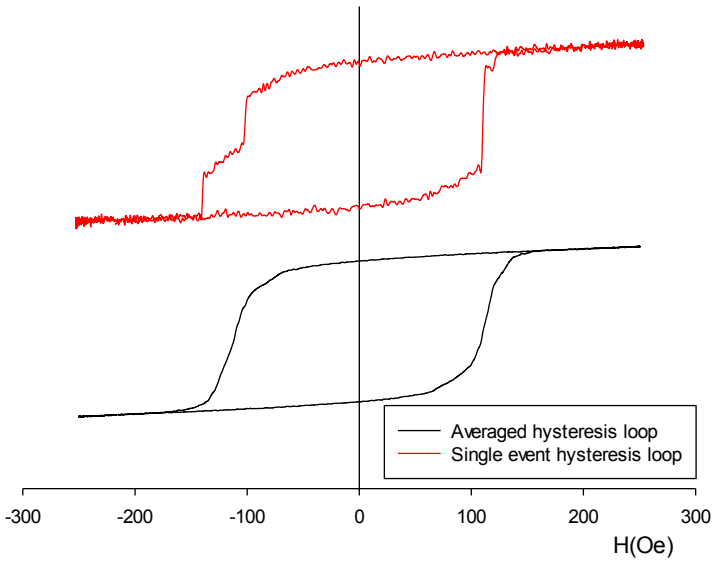

Figure 6.13 Single event and averaged hysteresis loops measured with the MOKE magnetometer on a 1µm wide CoFe wire.

MOKE signals are usually very low so the noise terms need to be reduced considerably. In addition to the physical contributions of the environment the MOKE used in this work uses multi-point signal averaging to reduce low frequency noise. It also uses signal modulation for lock-in detection in order to reduce the high frequency noise.

7. Exchange Bias Racetrack Memory

7.1. Preliminary Measurements

In 2008 Parkin proposed the first version of racetrack memory. As discussed in chapter 2, the domain wall pinning mechanism in this proposed racetrack used notches which were unreliable due to variations in shape which led to non-uniform pinning strengths. They were also complex to fabricate and hence, expensive to produce [2,45].

In order to address the issue of unreliable pinning of the notch system the alternative method presented in section 2.5 was used to pin domain walls. This involved the use of exchange bias pins. Two materials were considered for the ferromagnetic layer: CoFe and CoFeB. CoFe is known to have a high saturation magnetisation and can be engineered to be magnetically soft [58,127]. CoFe/IrMn stacks have been reported to give large exchange bias shifts, up to 3.6 kOe in plane [128]. The means of controlling the exchange bias in such systems are very well understood and have been discussed in depth in chapter 4 [13]. CoFeB was considered because of its similarities with $Co_{40}Fe_{60}$ in terms of magnetisation but also for its potential to be magnetically softer than CoFe due to the boron acting as a grain refiner. Previous knowledge of the material and its compatibility in exchange bias stacks was also an influential factor [129]. Typical values for the coercivity of CoFe films are of the order of 100 Oe and less than 20 Oe for CoFeB [58,130].

Jung *et al.* reported soft CoFe films with Cu, Ru seed layers. Their work concluded that the seed layers act to reduce the mean grain size of the films from 50-70 nm in the case of CoFe films deposited on Si substrates with or without a Ta seed layer to approximately 10 nm for the films grown on Cu and Ru seed layers [58]. Vopsaroiu *et al.* showed that soft CoFe can be prepared without the use of a seed layer and

deposited CoFe directly on a Si substrate. This was achieved by varying the deposition parameters of the material, in particular the growth rate by variation of the acceleration voltage of the system discussed in section 5.1.2 down to 120V [127]. The corresponding sputtering rate was 0.2 Å/s which gave a mean grain size of 14 nm; at 120V acceleration voltage the growth rate was 0.1 Å/s which gave a mean grain diameter of 7 nm [127]. This work also showed that CoFe can have soft properties as long as the mean grain size diameter is smaller than the exchange length which for CoFe was calculated to be L_{ex}=18.4 nm using equation 7.1 [127].

$$L_{ex} = \sqrt{A/K_u} \tag{7.1}$$

where K_u is the magnetocrystalline anisotropy (K_u= 2.7×10^5 ergs/cm^3) and A is the exchange constant which was calculated to be A=0.911 $\times10^{-8}$ ergs/cm using the Curie temperature approximation [127]. Furthermore, for 20 nm thick $Co_{35}Fe_{65}$ films sputtered in the same system the magnetisation was also reduced to 25% by reducing the acceleration voltage from 1000 V to 120 V [131]. The reduction in magnetisation was uncertain but two possible explanations were that the low M_S is due to poor crystallinity similar to amorphous Fe [132] or due to the fact that the amorphous material between the grains is more susceptible to oxidation [133].

The exchange length (L_{ex}) indicates the minimum distance over which the magnetisation may change direction without involving exchange energy. Frei *et al.* suggested that this distance was inversely proportional to the magnetisation (M_S) [134]. This is supported by the calculated values in the review of Abo *et al.* which indicated a grain size of the order of 10 nm for CoFe to be magnetically soft [135].

Figure 7.1 shows the hysteresis loops of 20 nm thick CoFe and CoFeB films deposited on circular Si substrates. Circular substrates were used in order to avoid the nucleation of domains at the corners of rectangular samples as the main mechanism of reversal in CoFe films is via domain wall nucleation and propagation.

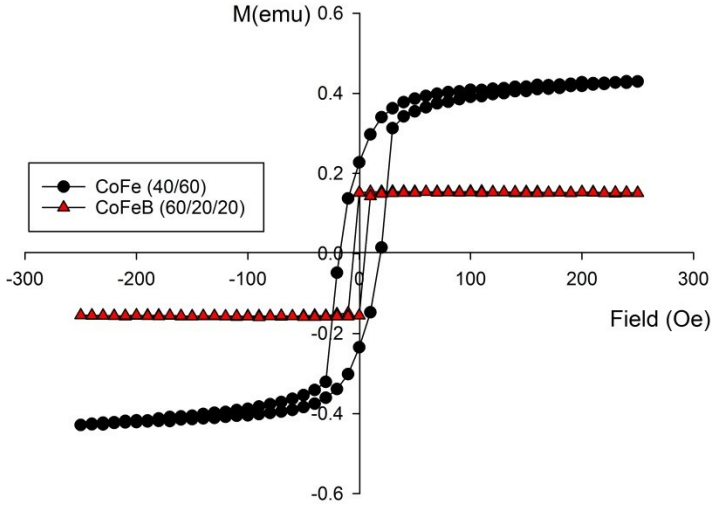

Figure 7.1 Magnetisation curves of CoFe and CoFeB films sputtered on circular Si substrates.

The measured coercivities are H_C=18 Oe for CoFe and H_C=5 Oe for $Co_{60}Fe_{20}B_{20}$, respectively. As predicted, the addition of boron to CoFe reduced the coercivity of the sample but also decreased the magnetisation to less than half of the undoped value as boron is non-magnetic and acts as a diluent. Since the magnetisation is reduced by more than 50% the reduction cannot be due to the boron diluting the magnetisation of the sample but instead it acts to break the exchange coupling. Both materials fulfilled the requirements for the ferromagnetic layer of the proposed pinning mechanism. The reason for the 20 nm film thickness will be put into context later in this section.

Two situations were considered to create exchange bias pins, one where the antiferromagnetic (AF) material is deposited under the ferromagnet (F) (bottom bias) and the other where it is deposited above

the ferromagnet (top bias). The bottom bias configuration allowed for the use of a seed layer under the antiferromagnet. In the top bias case the ferromagnetic layer acted as a seed for the antiferromagnet. Continuous films were deposited with these two configurations. The samples were set at T_{SET}=498 K for t_{SET}=90 min in a field of 20 kOe according to the method described in section 4.4.3 with the training removed and the hysteresis loops measured with the VSM are shown in figure 7.2 together with the corresponding sample structure.

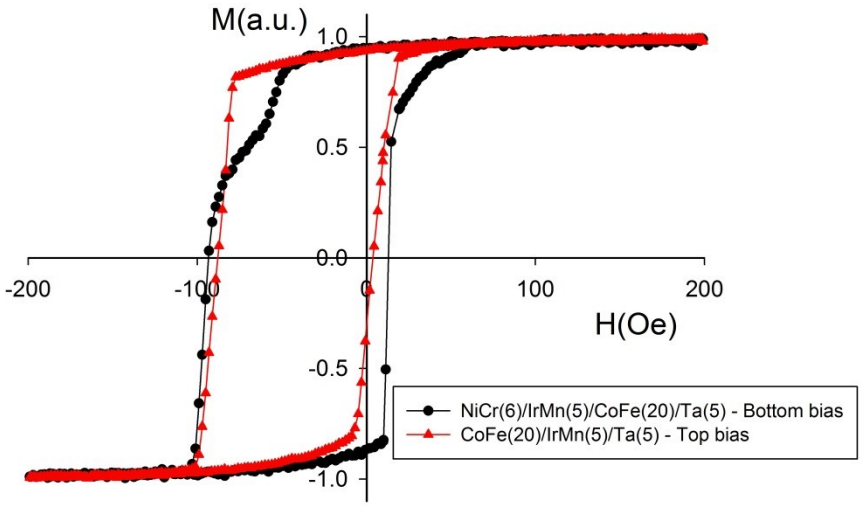

Figure 7.2 Magnetisation curves of unpatterned top bias and bottom bias films.

Both curves exhibit a loop shift of H_{ex}=46 Oe induced by the exchange bias at the F/AF interface. This result is unexpected as the presence of the seed layer under the antiferromagnetic layer should improve the (111) in-plane texture of the IrMn which should result in a larger shift (H_{ex}) [84]. Vallejo-Fernandez *et al.* studied the effect of the thickness of the ferromagnetic layer (t_F) in IrMn/CoFe stacks and showed that the value of the exchange bias decreases according to equation 7.2 [98]:

$$H_{ex} \propto {}^{1}/_{t_F} \qquad (7.2)$$

Hence, this accounts for the reduced value of the exchange bias in the systems for which data is shown in figure 7.2. The exchange field from the ferromagnetic layer reduces the value of the energy barrier distribution within the antiferromagnetic layer which promotes thermally activated transitions of the direction of order in the antiferromagnet and a lower value for the exchange bias, as discussed in section 4.4. Equation 7.3 is reproduced from section 4.4 and shows the energy barrier of the antiferromagnetic grains.

$$\Delta E = K_{AF} V_{AF} \left(1 - \frac{H^*}{H_K^*}\right)^2 \tag{7.3}$$

where H^* is the exchange field from the ferromagnetic layer and H_K^* is a pseudo-anisotropy field similar to the anisotropy field in ferromagnets. Hence, increasing the thickness of the ferromagnetic layer results in an increase of the exchange field which reduces the energy barrier, reducing the value of the exchange bias.

A peculiarity occurs in the magnetisation of the bottom bias sample as the field is reduced. If when increasing the field the change in direction of magnetisation is sharp, when reversing the field the reversal is in two steps which is an apparent bimodal switching. Between -50 and -70 Oe the normalised magnetisation is reduced to a half. From -70 to -95 the magnetisation is fully reversed. As discussed in section 4.4 the anisotropy of the IrMn layer is magnetocrystalline so it is uniform for the layer at a value of $(5.5\pm0.5)\times10^6$ ergs/cc [82]. When grown on a NiCr seed layer IrMn was shown to have an anisotropy up to 4.5×10^7 ergs/cc [85]. Hence, the energy barrier ΔE for each grain is dictated by its volume. Since the entire grain size distribution cannot be set via thermal activation, grains with $V>V_{SET}$ will not contribute to the exchange bias. The abnormality in the switching of the bottom bias film results from the partial setting of the grains with $V\approx V_{SET}$. The grain size

distributions and the limit values for the grain size diameters and their associated volumes are shown in figure 7.3

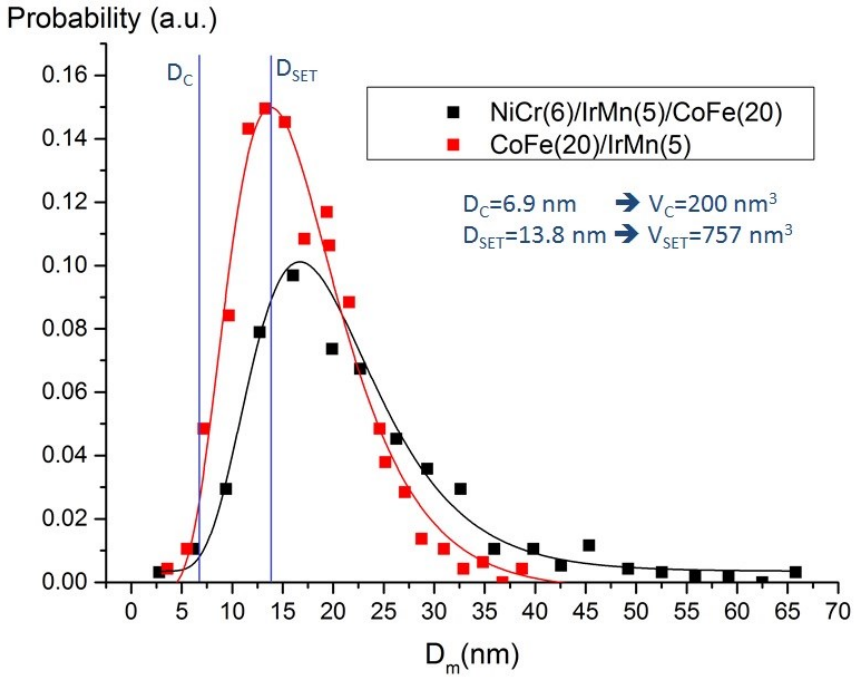

Figure 7.3 Grain size distributions with lines of best fit.

7.2. Coercivity Dependence in Ferromagnetic Nanowires

This section looks into how the patterning of the ferromagnetic layer affects the domain wall formation and propagation within the proposed devices. It also assesses the structural influence on the sample behaviour. The way sample parameters influence its properties allow for a net appreciation of the effect of the proposed method of pinning via exchange bias. In other words, it allows the identification of the sole contribution of the pinning from the antiferromagnetic layer in the samples.

Samples were grown according to the protocols described in chapter 5. A schematic of the sample shape is shown in figure 7.4. This

shape allows for a single domain wall to be introduced from the square pad into the wire. This sample shape was used by Yamaguchi *et al.* to demonstrate current driven domain wall motion in 10 nm thick $Ni_{81}Fe_{19}$ wires [53,136]. At the opposite end from the pad the wire is sharply pointed to prevent domain wall nucleation [137,138]. The nucleation of reversed domains occurs near the corners of the elements where a transverse demagnetising field occurs. The demagnetising field which arises on the two inclined sides of the apex in the sharp end cancel each other out resulting in a zero transverse field [137].

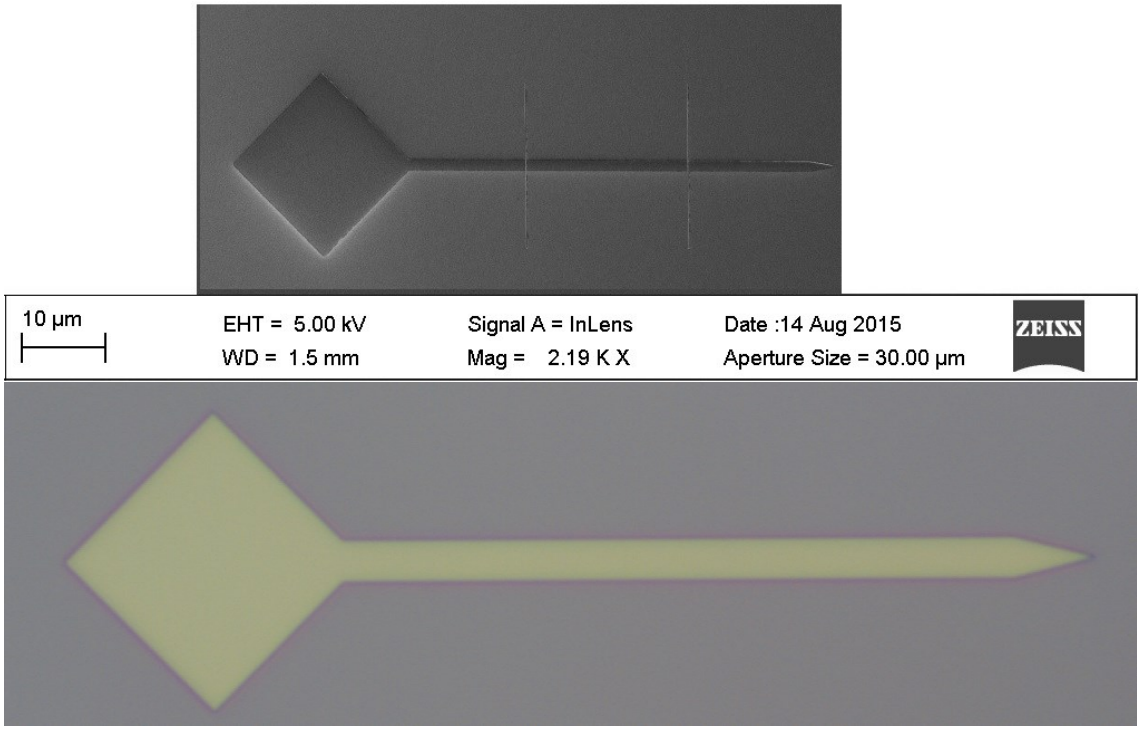

Figure 7.4 SEM image of a device with two antiferromagnetic wires (top). The patterned resist for a ferromagnetic layer of a racetrack memory device (bottom).

The magnetic characterisation of the samples was done using the MOKE described in section 6.2. The measurements shown in this section are changes in the voltage produced by the photodetector of the MOKE. The voltages corresponding to saturation have been normalised,

hence the notation for the ordinate axes of graphs shown in this work is M/M_S.

7.2.1. Wire Width Dependence

Domain wall widths are a result of the balance of exchange energy and magnetocrystalline or anisotropy energy. For the purpose of the work presented in this thesis, an assessment of the fields required to move domain walls through CoFe wires was needed. The majority of related publications are on wires fabricated of NiFe alloys which have very low crystalline anisotropy meaning that the size and shape of the wire have a greater influence on the formation and movement of domain walls because of the shape anisotropy. However, the samples used for the work presented in this thesis were fabricated of CoFe which has anisotropy values of the order of 10^4 ergs/cc [58].

Two sets of samples, S1 and S2, were fabricated out of the same $Co_{40}Fe_{60}$ alloy as discussed in section 7.1 on Si substrates patterned via e-beam lithography in the shape shown in figure 7.4. Wires with a thickness of 20 nm and with widths of 500 nm, 1 μm and 3 μm were considered for this experiment. The three wires were deposited on the same Si substrate. Hysteresis loops were measured using the MOKE magnetometer and the values for the coercivity (H_C) were extracted from the loops. The magnetic field was applied parallel to the direction of the wire and the MOKE probe was placed in the centre of the pad for the nucleation measurement and 20 μm from the pad edge along the wire for the injection measurement. The results are shown in table 7.1.

No significant differences can be observed for the nucleation of reverse domains in the pad. All events occurred at (90±5) Oe apart from the device on sample S1 with the 500 nm wide wire which required a 30% reduced field to nucleate domains. This is probably due to a lift-off

artefact, such as that shown in figure 5.7, which enabled the nucleation at a much smaller field. Larger fields were required to reverse the magnetisation in the wires which was expected. Similar injection fields were required for reversal in the wires with the same width on both samples S1 and S2. The injection fields appear to increase with the wire width but for sample S1 no significant increase in the field appears between the 1 μm and the 3 μm wire. On sample S2 the increase in the width from 1 to 3 μm results in a ~30 Oe increase in the injection field. These results show that a 600% increase in wire width only contributes to an increase in the injection field of ~30 Oe showing that the wire shape makes a small contribution to the switching but the magnetocrystalline anisotropy dominates the reversal.

	Wire width (μm)	Pad nucleation field (Oe)	Wire injection field (Oe)
S1	0.5	62	110
	1	90	130
	3	85	134
S2	0.5	84	100
	1	89	100
	3	95	136

Table 7.1 Nucleation and injection field values for CoFe wires.

7.2.2. Position Dependence

It is important for the proposed racetrack memory to asses the unimpaired motion of the domain walls within the ferromagnetic wires. The samples studied consisted of ferromagnetic wires with shapes as shown in figure 7.4, patterned via e-beam lithography. The sides of the square pad were 15μm long and the wire was 100 μm long and 20 nm thick. Different wire widths were considered. Details on the fabrication process have been presented in chapter 5. Due to long exposure to the

plasma in the deposition chamber when the HiTUS acceleration voltage was less than 200 V (>30 min at 100 V with a sputtering rate of 0.1 Å/s and >15 min at 200 V with a sputtering rate of 0.2 Å/s) the substrates reached temperatures of over 100°C and the patterned resist on the substrates would deteriorate and make lift-off impossible. Hence, the samples were sputtered at 900 V which led to temperatures not greater than 50°C and deposition times of approximately 3 minutes.

The sample consisting of CoFe wires was mounted on a stepper motor X-Y stage which allowed the laser probe to be placed with submicron precision at different points along the sample. This allowed for local measurements of the hysteresis loops.

Figure 7.5 shows a series of hysteresis loops measured along the 300nm wide wire at different positions from the center of the pad. The loops are averaged over 100 cycles. This was done for a better signal to noise ratio in the measured Kerr voltage. For this sample the coercivity of the loops appears to increase slightly as the laser probe gets closer to the sharp end of the wire. The coercivity ranges between 105 and 120 Oe.

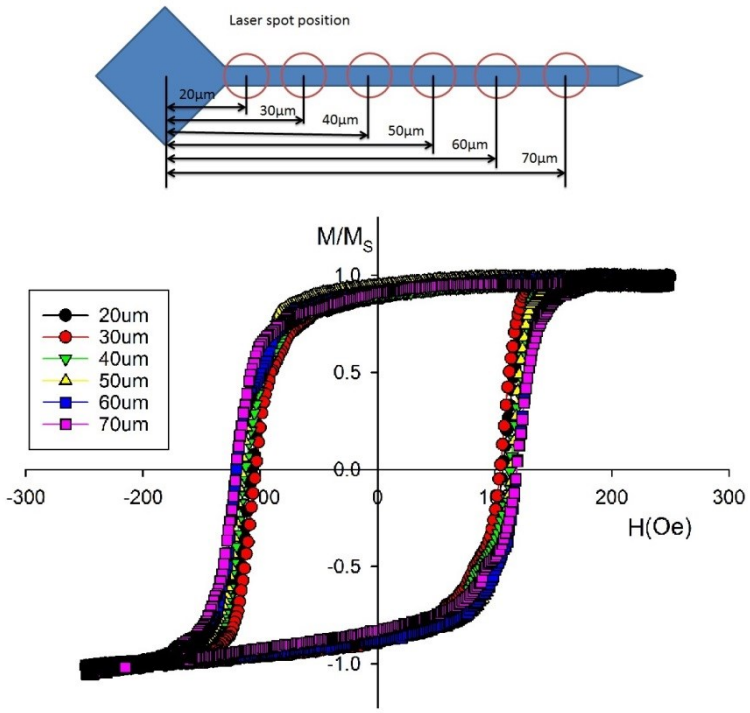

Figure 7.5 Hysteresis loops measured along a 20 nm thick and 300 nm wide CoFe wire.

The data shows that domain wall nucleation is a highly reproducible event in these wires. The events occur within a range of fields 15 Oe wide. Although not as precise as the events reported by Cowburn *et al.* for 100nm wide, 5nm thick $Ni_{80}Fe_{20}$ wires which occurred exactly at 180 Oe everywhere along the wire, this still presents usability as the range of the switching fields is narrow compared to the average fields required for the switching [139,140].

However, Chapman *et al.* reported that small elements may have a distribution of switching fields which is not problematic as long as the switching field range is only a fraction of the average switching field [140]. This is confirmed for the devices used in this study and figure 7.6 shows the averaged loops of three different wires. The MOKE probe for these devices was positioned 20 µm from the end of the wire on the side with the injection pad. The smallest switching field measured was 106 Oe and the largest 113 Oe, giving a range of coercivity of 7 Oe with an average of 110 Oe.

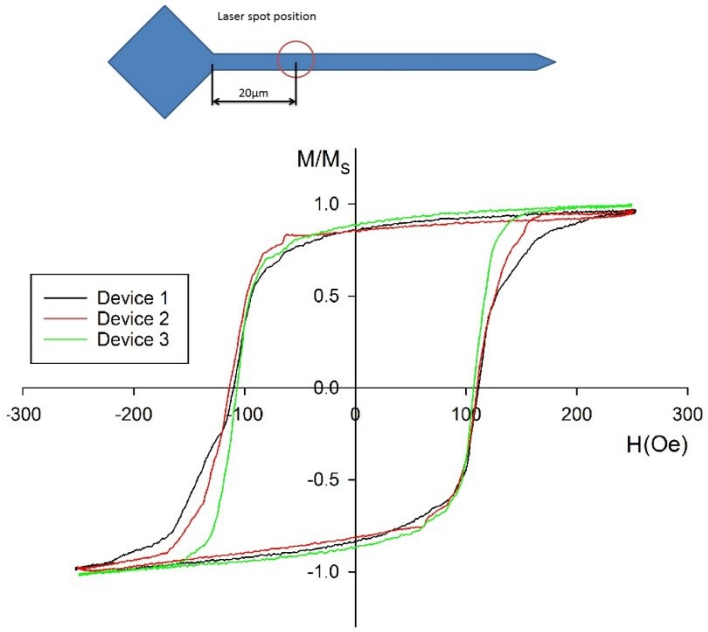

Figure 7.6 Hysteresis loops measured along 20 nm thick and 300 nm wide CoFe wires 20 µm from the pad.

Figure 7.6 shows that for the devices studied the remanent magnetisation is ~10% smaller than the saturation. This is due to domain wall relaxation after the removal of the field in order to reduce the magnetostatic energy. The direction of magnetisation is maintained until a reverse field of approximately -80 Oe is applied. At these values of the applied field the domain wall quickly nucleates and propagates through the wire switching the net direction of magnetisation, but not fully saturating the sample. This is due to domain wall pinning due to shape factors within the wire: steps on the Si substrate, surface roughness on the CoFe wires or lithographical artefacts. Confirmation of pinning introduced as a result of the fabrication process is shown in figure 7.7. This shows a single shot hysteresis loop of Device 1. The domain wall relaxation is present in the absence of field as it is in the averaged loops and generates a 10% decrease in magnetisation. Reversal due to domain wall motion occurs at 103 Oe but in order to

fully move the domain wall across the probed area of the sample a 25 Oe pin needs to be overcome.

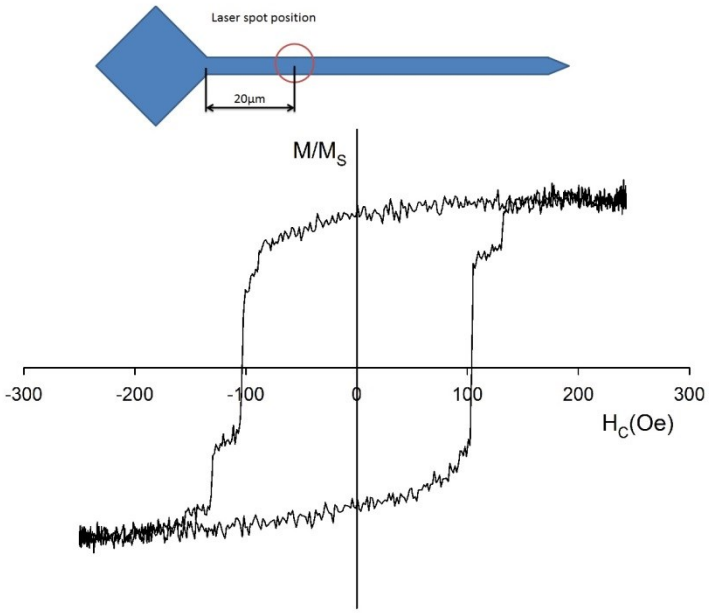

Figure 7.7 Single shot loop of Device 1 measured 20 µm from the pad.

Figure 7.8 shows the hysteresis loops for a CoFe device with the structure shown in figure 7.4. The MOKE probe was positioned on the wire 20 µm from its end on the side with the injection pad. The sides of the square pad were kept at 15 µm long and the wire was 100 µm long, 20 nm thick and 500nm wide. The loops are averaged over 100 cycles and were taken at moments t1, t2… t10 which were 60s apart. This time interval was chosen so that no loops from previous measurements were included in the 100 cycle average. The frequency of the applied field in the MOKE is 27 Hz which is equivalent to just under 0.04 s per loop. By performing the measurements at time intervals 60 seconds apart the events are monitored on a time scale three orders of magnitude greater in order to show the reproducibility of the events which occur within the wire.

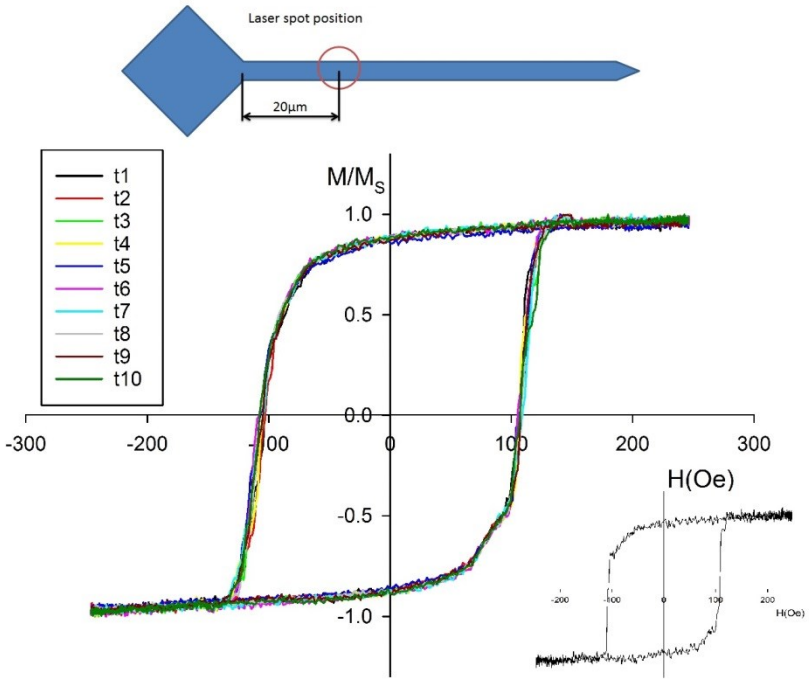

Figure 7.8 Averaged hysteresis loops for of a 500 nm wide CoFe device. Inset- single shot loop of the same device.

The switching range for this device is within 5% of the switching field. The measurements of these 500 nm wide wires do not show any significant pinning effects due to wire imperfections, unlike the 300 nm wide devices shown in figure 7.6. In the absence of a field the wires exhibit domain wall relaxation similar to those seen in figures 7.6 and 7.7 which result in a decrease in magnetisation by 10%. The single shot loop shown in the inset of figure 7.8 shows the same behaviour with no other artefacts. Between 60 Oe and the coercive field the magnetisation is reduced by 50%, but not reversed. This can be explained by a domain wall relaxation in order to reduce the magnetostatic energy before it quickly propagates through the wire at approximately 105 Oe.

Similar studies were carried on CoFeB devices. These devices are of identical shape to those fabricated out of CoFe. Figure 7.9 shows hysteresis loops measured with the MOKE probe at the same spot on

the device at 60 s intervals. The MOKE probe was positioned on the wire 20 μm from its end on the side with the injection pad.

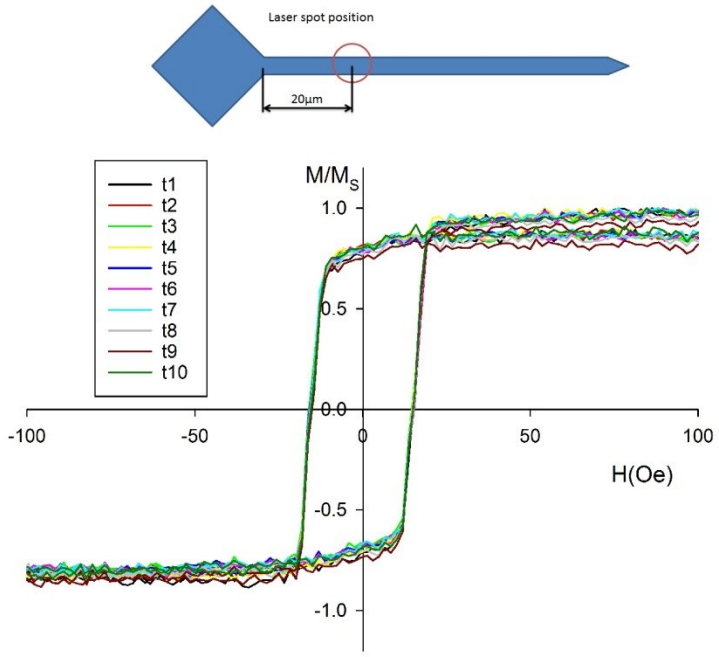

Figure 7.9 Averaged hysteresis loops for a 500 nm wide CoFeB device 20 μm from the injection pad.

For all the events monitored the switching occurs at 15 Oe. The loops present near perfect squareness. Because of the lack of crystalline anisotropy in CoFeB, the domain walls travel unhindered through the wires unlike the CoFe wires which exhibit domain wall relaxation which accounts for the reduced squareness in the hysteresis loops. Domain walls have been shown to reduce their width when a field acts upon them in order to unpin them from a notch [141]. The crystalline anisotropy of the CoFe wires leads to narrower domain walls but most importantly inhibits the nucleation of reverse domains which accounts for the switching at field values approximately seven times larger.

Pinning due to fabrication artefacts has less of an effect on the CoFeB wires as this leads to a switching range of 1 Oe for an average switching field of 16 Oe. This is shown in figure 7.10 which shows averaged hysteresis loops measured along the wire. The loops are

square indicating that the domain walls travelling through the wire do not suffer changes or pinning.

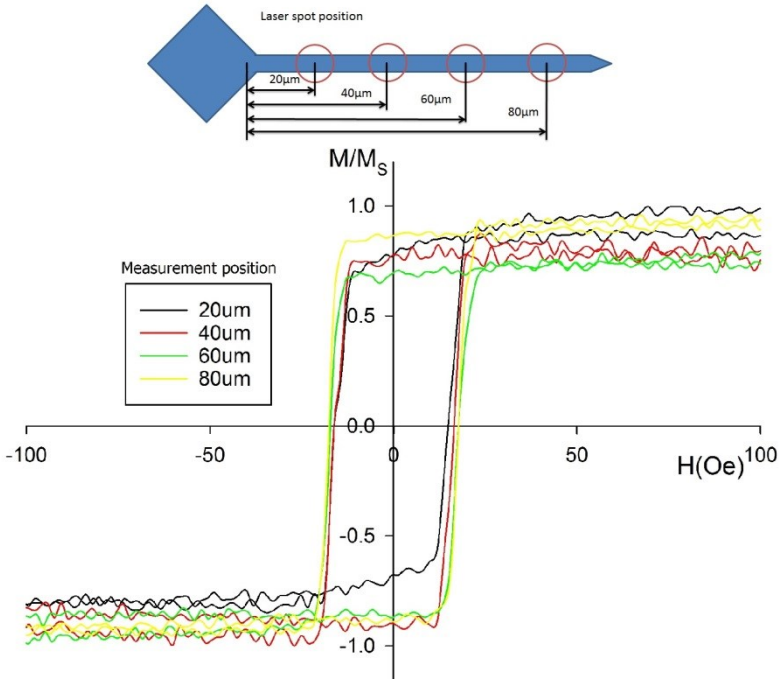

Figure 7.10 Averaged hysteresis loops measured along a 20 nm thick and 500 nm wide CoFeB wire.

7.3. Coercivity Dependence in Exchange Biased Ferromagnetic Wires

7.3.1. Pinning Field Dependence

As discussed in chapter 2 pinning domain walls in racetrack memory is essential for its functionality. It is the reliability and control of the pins which affect the parameters for racetrack memory, such as the spacing between domain walls which affects the memory density, threshold current densities to move the domain walls typically of the order of 10^8 A/cm^2, pulse length of the order of tens of nanoseconds and shape which influence memory speed and power consumption [2,43,45,49,52,142,143]. Even though Parkin managed to improve his version of the racetrack memory [2,4,43,45,49,51,52,143,144] the

method for pinning domain walls presented in the work described in this thesis offers a high degree of control over the pins [145].

In this work samples were fabricated in a multi-step process that involved lithographic patterning of resist via optical lithography, material deposition using HiTUS and lift-off for each layer. The samples considered for this experiment consist of two layers: a ferromagnetic layer of the same shape as that shown in figure 7.4 and a pinning layer. The pinning layer consists of antiferromagnetic wires which lie perpendicular to the ferromagnetic wire. Figure 7.11 shows a schematic together with an optical image of the device.

Figure 7.2 shows two possibilities of exchange biasing the ferromagnetic layer depending on the relative position of the ferromagnetic and antiferromagnetic layers. The bottom bias configuration allows for the use of a seed layer whereas the top bias configuration uses the ferromagnet as a seed layer. In the case of the devices a bottom pinned configuration does not allow for a flat ferromagnetic wire. In this configuration the ferromagnetic wire must form a step over the antiferromagnetic wires in order to maintain its continuity. The thickness of the antiferromagnetic wires in the bottom pin configuration is 11 nm including the seed layer. In order to maintain a continuous ferromagnetic wire, its thickness was set to 20 nm. For the comparison between the two configurations to be relevant, the CoFe layer thickness was kept at 20 nm for both top and bottom biased devices.

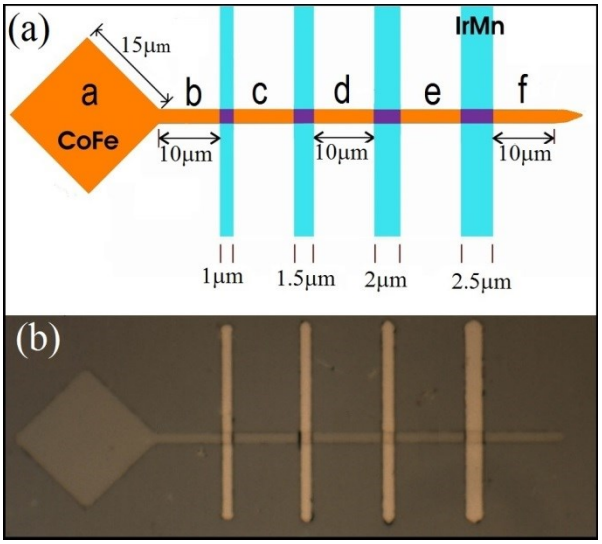

Figure 7.11 Schematic diagram and a microscope image of the device.

The samples were field cooled from 500 K to room temperature in a field of 20 kOe. The field was applied along the direction of the antiferromagnetic wires to set the order in the grains and thereby induce the exchange bias. The antiferromagnetic material used to pin the CoFe device was IrMn which has a Néel temperature of 690 K [121]. Setting at or above this value will result in film damage so the setting process is by thermal activation [84]. The setting process is discussed in detail in section 4.4.3.

The MOKE magnetometer described in section 6.2.4 was used for measurements of the magnetic behaviour of the exchange biased samples. The sample was placed on the magnetometer stage under the probe and moved under the probe along the direction of the CoFe wire. The magnetic field was applied along the direction of the wire. Figure 7.12 shows the dependence of the pinning strength with antiferromagnetic wire width of a 3 µm wide ferromagnetic wire. The diagram is made to show the values of the coercivity for the corresponding points on the wire where the magnetometer probe was placed.

The data shown in figure 7.12 clearly shows an increase in coercivity with increasing width of the antiferromagnetic wires. This indicates that the domain wall pinning strength is dependent on the width of the antiferromagnetic wire. An identical device with antiferromagnetic wires which were not set exhibited very small domain wall pinning at the ferromagnet-antiferromagnet crossing points. Typically, this was of the order of 5 Oe which is almost within error of the field measurement. This confirms that it is the exchange bias effect which gives rise to the domain wall pin and not just the presence of the antiferromagnetic wire. Any domain wall pinning due to the unset antiferromagnetic wire would therefore be of a similar strength to the inherent domain wall pinning strength in the wire.

For the case of the bottom bias configuration the domain wall nucleation field in the square pad was 107 Oe and the domain wall injection field into the wire was 110 Oe. The coercivity (H_C) of the ferromagnetic wire adjacent to the 1 μm wide antiferromagnetic wire (point c in figure 7.11) was measured to be (113±5) Oe giving a pinning strength for the 1 μm wide antiferromagnetic wire of 3 Oe. The pinning fields for the 1.5, 2 and 2.5 μm wide antiferromagnetic wires were measured to be 6, 9 and 12 Oe, respectively.

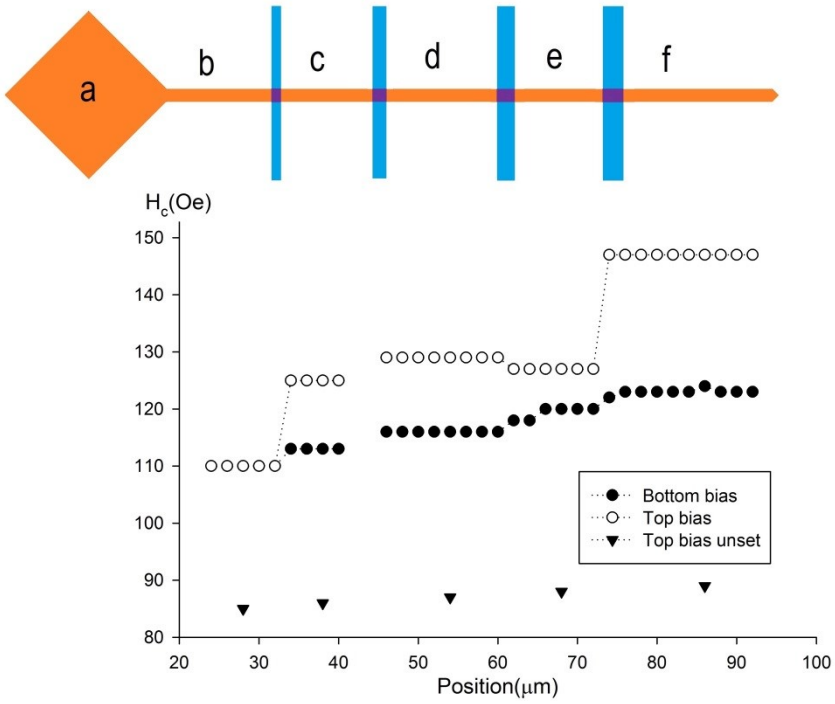

Figure 7.12 Reproducibility of the coercivity at the points labelled in the racetrack memory with bottom bias (full circles) and top bias (empty circles) configurations. Also shown is data (triangles) for a device where the AF wires were not set.

In order to remove any domain wall pinning effects due to the ferromagnetic wire crossing the antiferromagnetic wires and therefore not being fully planar, a top-bias device was also measured with identical layer and wire dimensions. The domain wall nucleation and injection fields were measured to be 65 and 110 Oe, respectively, which agrees with the values for the bottom bias device. The pinning fields in this device for 1, 1.5, 2 and 2.5 μm wide antiferromagnetic wires were measured to be 15, 19, 17 and 37 Oe, respectively. These values are significantly larger than those for the bottom bias device. Again, these results verify that such a structure is capable of producing domain wall pins of controlled strength. The value for the 2.5 μm wide antiferromagnetic wire is particularly significant as it is comparable to the values achieved by Parkin *et al.* for a notched system of up to 30 Oe for a 30 nm thick $Ni_{81}Fe_{19}$ wire and 15 Oe for a 10 nm thick $Ni_{81}Fe_{19}$

wire [2]. This is significant for device development as it shows that the strength of pins can be controlled via the antiferromagnetic wire width.

Figure 7.12 shows the values of the coercivity (H_C) measured repeatedly at the points on the ferromagnetic wire indicated in the schematic diagram included in the figure. Each point on the graph is a separate measurement of H_C and is that from 100 averaged loops measured with the MOKE magnetometer. The data shown in figure 7.12 show that the measured values of H_C are remarkably consistent. This indicates that the strength of the induced domain wall pins is reproducible.

The strength of the domain wall pins is modest, but, importantly, controllable. The strength of the exchange bias effect (H_{ex}) varies as the inverse of the thickness of the ferromagnetic layer t_F ($H_{ex} \sim 1/t_F$) [13]. Hence stronger pinning is expected in thinner ferromagnetic wires.

7.3.2 Effect of Setting Angle

It is known that, in general, domain walls in narrow wires lie at an angle to the direction of the wire. With the method of pinning domain walls using exchange bias it is possible to vary the direction of the exchange bias at the crossing points of the ferromagnetic-antiferromagnetic junctions.

Only samples with 1 μm wide ferromagnetic wires have been considered for this study in both configurations, with top and bottom bias. This was due to the resist being hardened (hard bake) in the deposition system after patterning due to the exposure to temperatures of the order of 50°C for periods of time of approximately 30 minutes after the sputtering had finished. The waiting period of 30 minutes is a requirement for the sputtering machine (HiTUS) as it allows for the

system to cool down in order to be vented. This caused severe difficulties during lift-off and only the samples with a 1 μm wide ferromagnetic wire were consistent in this experiment and could be compared.

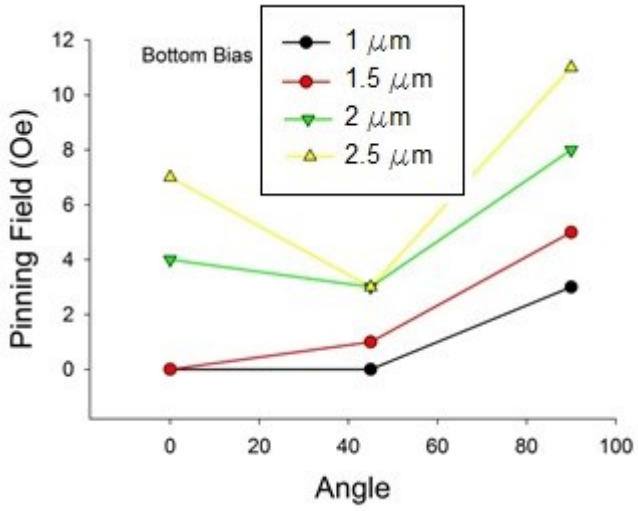

Figure 7.13 Dependence of pinning strength with direction of the exchange bias in a bottom bias device.

The antiferromagnetic wires were 1, 1.5, 2 and 2.5 μm wide. Figure 7.13 shows the strength of the pinning field in bottom bias devices with respect to the angle between the direction of the setting field and the ferromagnetic wire. The same device was used for all measurements. The data clearly show that when the antiferromagnetic wire is set in a direction perpendicular to the ferromagnetic wire the pinning is the greatest, regardless of the width of the pin. The requirement for the ferromagnetic wire to step over the antiferromagnetic wire introduces great complexity to the pinning mechanism, hence the coercivity measurements are only able to show proof of principle and do not provide any explanation for the pinning mechanism.

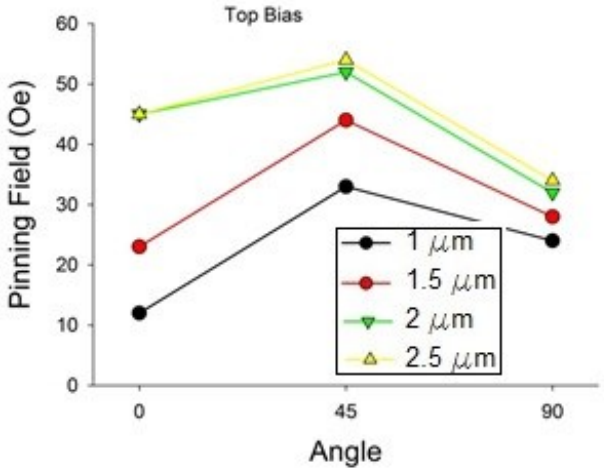

Figure 7.14 Dependence of pinning strength with direction of the exchange bias in a top bias device.

Figure 7.14 shows the same measurement but on a top bias device. In this case a clear trend is observed, where for all antiferromagnetic wire widths the strongest pinning occurs when the setting direction is at 45° to the ferromagnetic wire. The ferromagnet is coupled to the antiferromagnet at the junctions. The considerably stronger pinning which occurs at the 45° angle can be explained by having a greater number of spins within the domain wall which are parallel to the setting direction. The angle resolution for the measurement was limited by the sample holder for the cryostat of the VSM where the samples were set.

Recent studies based on this work enabled viewing the shape of domain walls within the wire. Figure 7.15 shows the image of a domain wall within a more recently fabricated CoFe wire with the same parameters of the wires studied in this work: 15μm×15μm injection pad and 20 nm thick. Figure 7.15 shows that in this particular case the domain wall does not sit strictly at 45° but rather at a distribution of angles. This indicates that pinning domain walls in nanowires using exchange bias is complex and cannot be characterised by coercivity measurements only. For a full explanation of the pinning mechanism

domain walls should be imaged in real time while crossing the exchange bias pins. Furthermore, the geometrical complexity of the bottom bias device may allow for imaging the domain walls as they cross the pin, whereas the top bias configuration does not allow the same characterisation due to the ferromagnetic wire being covered by the antiferromagnetic wire at the pin location. Hence, atomistic scale modelling would also be required to further the understanding of this pinning mechanism and correlate with experimental results.

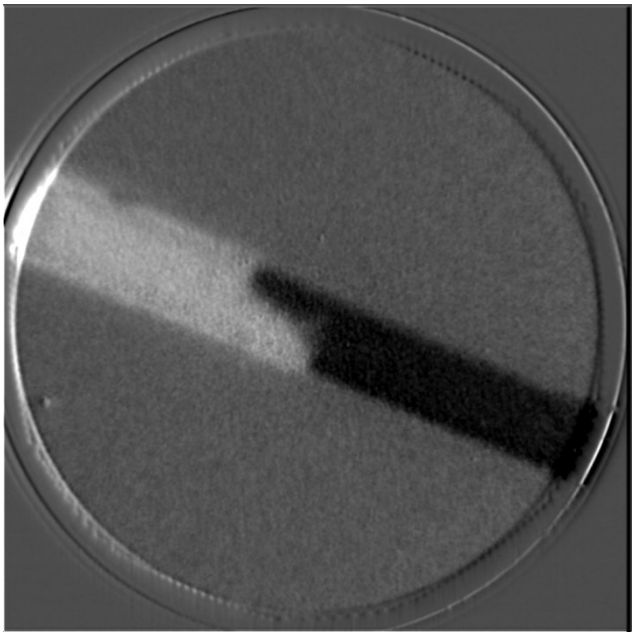

Figure 7.15 PEEM image of a domain wall in a 20 nm thick 1 µm wide CoFe wire [Acknowledgement to Joseph Gompertz].

The measurements shown in figures 7.13 and 7.14 are another confirmation that the method of pinning domain walls described in this work has a high degree of control over the pins. The data also proves that pinning strength can be controlled via the width of the antiferromagnetic pin, regardless of the setting angle.

To date the development of racetrack memory has been limited by the inability to produce controllable domain wall pinning sites in the

nanowires. Using the method presented in this work, domain wall pins of well-defined and reproducible strength can be created and controlled.

8. Conclusions and Future Work

8.1. Conclusions

This study is a proof of concept for a method of pinning domain walls in nanowires using exchange bias. The method for pinning consists of depositing antiferromagnetic wires perpendicular to ferromagnetic wires and inducing exchange bias at the crossing points. The material used for the ferromagnetic layer was CoFe and for the antiferromagnetic layer IrMn. Sputtered polycrystalline CoFe/IrMn bilayers produce the largest values of exchange bias at room temperature. CoFeB was also considered because of its intrinsically low coercivity and high magnetisation. However, CoFeB/IrMn bilayers did not exhibit exchange bias at room temperature. Because of this, only films and devices consisting only of single layer CoFeB were studied.

Films and wires with the same layer structure were sputtered on Si substrates. For wire fabrication, the substrates were covered with a lithographically patterned mask. The mask was removed via lift-off after deposition revealing the wires. Two pinning configurations were considered for the exchange bias stacks depending on the order in which the materials were sputtered. The bottom bias configuration had the IrMn (5 nm) deposited first on top of a NiCr (6 nm) seed layer and the CoFe (20 nm) layer deposited on top of the IrMn. The thickness of the CoFe was set to 20 nm in order for the nanowires to be continuous in the bottom bias configuration, as the wire stepped over the antiferromagnetic wire. A consequence to the 20 nm thickness of the CoFe was the reduced value of exchange bias of the order of 40 Oe. In the top bias configuration the CoFe (20 nm) was deposited on the Si substrate and acted as a seed layer for the IrMn (5 nm) which was deposited last. For the bottom bias configuration the NiCr seed layer

was used to improve the (111) texture of IrMn. These two configurations were considered for both films and wires.

The single layer films of CoFe and CoFeB were measured in the VSM. The CoFe film had a coercivity of 18 Oe and the CoFeB had a coercivity of 5 Oe. The CoFeB film had a saturation magnetisation 50% smaller than the CoFe film. This measurement showed that these two materials can be engineered to be soft which is important for racetrack memory applications. In order to measure the value of the exchange bias films in both top and bottom bias configurations were sputtered. Samples were set in the VSM cryostat to induce order in the antiferromagnet. Hysteresis loops were measured in the same VSM and both CoFe samples showed a loop shift of 46 Oe. The CoFeB samples did not exhibit any exchange bias.

The patterned wires were studied initially without any antiferromagnetic wire in contact. The coercivity of these wires was measured using a focussed MOKE magnetometer. CoFe wires with widths of 0.5, 1 and 3 μm were measured and the coercivity varied by only 30 Oe for a 600% increase in wire width. This indicates that there is a large contribution to the reversal process from the magnetocrystalline anisotropy. Reproducibility measurements were also performed on the wires. The laser probe of the magnetometer was held in the same place and coercivity was measured over a time interval large enough for more than 1000 reversals to occur. No change in the loops was observed.

The coercivity was also measured along the wires to evaluate the changes in coercivity due to wire defects, fabrication artefacts or roughness. The range in which the coercivity varied was measured to be 7 Oe for a 110 Oe average switching field. The same measurement was

performed on CoFeB wires which gave a range 1 Oe wide for an average switching field of 16 Oe.

The pinning induced in the nanowires by antiferromagnetic wires deposited perpendicular to the ferromagnetic wires was measured for CoFe wires in both bottom and top bias configurations. Both configurations showed an increase in the pinning field with increasing antiferromagnetic wire width. However, much stronger pinning occurred in the top bias configuration because of the step created in the path of the domain wall in the bottom bias configuration. This experiment proved that the pinning strength of an exchange bias pin is dependent on the size of the pin. The setting angle of the exchange bias was also shown to have an effect on the strength of the pin showing that a minimum in pinning is found in the bottom bias configuration when the antiferromagnetic wires are set to 45° to the ferromagnetic wire direction. At the same angle in the top bias devices a maximum in pinning strength was observed for all antiferromagnetic wire widths. The maximum value for an exchange bias domain wall pin was measured to be 55 Oe for the top bias configuration at a setting angle of 45° and antiferromagnetic wire width of 2.5 μm.

The work presented in this thesis shows that domain walls can be pinned in nanowires using exchange bias. Only a limited number of strategies to control the pinning strength have been investigated and the results showed modest values for pinning. This was partially due to the thick layer of CoFe which leads to a decrease in exchange bias ($H_{ex} \propto 1/t_F$). Another reason was the necessity to place the antiferromagnetic layer on top of the ferromagnetic layer which led to a decrease in the anisotropy of the IrMn and so a decrease in the exchange bias. Other materials such as NiFeCr which is used in write-

head shields can be used as a ferromagnetic layer which can improve the (111) texture of the IrMn.

8.2. Future Work

The work presented in this thesis opens a new possible mechanism for domain wall pinning in racetrack memory. Proof of principle of the proposed mechanism was clearly demonstrated but only a few means of control have been investigated. Other means for control of the strength of the domain wall pins still need to be investigated and furthermore there are a number of features of the present work which need to be optimised.

Understanding of the pinning mechanism is very important for the development of the racetrack memory based on this pinning method. Hence, this study would make use of imaging the domain walls in various positions along the wire, before the pin, whilst pinned and after the pin. Real time domain wall observation via Lorentz TEM or Kerr microscopy would provide a great insight on the behaviour of the domain wall as it passes through the pin. Should the pin have any influence on the shape or type of the domain wall a correlation with micromagnetic simulations can be made.

Domain walls may be difficult to image at the pinning site in the top bias configuration. Hence, fabrication of a bottom bias device where the ferromagnetic layer remains flat as it crosses the antiferromagnetic wire may be required. As a continuation of this work domain walls have been imaged in unbiased ferromagnetic wires by PhotoEmission Electron Microscopy (PEEM) at Diamond Light Source.

A great degree of control for exchange bias comes from the anisotropy of the IrMn which can be controlled via seed layers. If a

cheap and easy method of fabricating bottom bias devices where the ferromagnetic wire remains flat as it crosses the antiferromagnetic wire is found then known seed layers, such as NiCr or Ru can be used. As the top bias configuration is still the easiest to fabricate, the ferromagnetic wire must also act as a seed layer for the antiferromagnet. NiFeCr can be used as a ferromagnetic material or potential candidates can be sought in the Heusler alloys.

The thickness of the ferromagnetic wire has a significant effect on the magnitude of the exchange bias. In this study a 20nm thick ferromagnetic layer was used because of the need to maintain wire continuity at the pin in the bottom bias devices. With the current fabrication techniques the top bias configuration shows the greatest values for the pinning strength and comparable to those initially showed by Parkin [2]. Hence, the thickness of the ferromagnetic wire can be reduced and a systematic study on ferromagnetic wires with different thicknesses may help design devices with much larger pinning strengths. Also the width and thickness of the wire contribute to the size and type of the domain wall so systematic studies where the thickness and width of the ferromagnetic wires are varied will contribute to finding the optimum dimensions for a racetrack memory device.

The resists used for the lithography in combination with the limitations of the sputtering system and the need for 20nm thick ferromagnetic layers meant that a certain sputtering rate was required in order to successfully obtain devices. Improving the fabrication method via use of easier to clear resists or by means of maintaining a low temperature of the substrate in the deposition chamber will allow for reducing the sputtering rate. This will provide control over the grain

size of the deposited materials and with it control of the pinning strength and of the coercivity of the ferromagnetic wires.

There is also a requirement to drive the devices via electric current. Even if an attempt at initial four point measurements for current-driven domain wall motion in exchange biased wires has been tried, because of device failure a complete set of data was not obtained. Devices with attached spin tunnel junctions should be designed in order to perform investigations on the movement of domain walls.

List of Abbreviations

RAM- Random Access Memory

MRAM- Magnetic Random Access Memory

HDD- Hard Disk Drive

SSD- Solid State Drive

NAND- Negative AND (logical operation)

DRAM- Dynamic Random Access Memory

GMR- Giant Magneto Resistance

TMR- Tunnelling Magneto Resistance

F- Ferromagnetic

AF- Antiferromagnetic

DW(s)- Domain wall(s)

RM- Racetrack Memory

STT- Spin Transfer Torque

TEM- Transmission Electron Microscope

SEM- Scanning Electron Microscope

MOKE- Magneto Optical Kerr Effect

AGFM- Alternating Gradient Field Magnetometer

VSM- Vibrating Sample Magnetometer

MBE- Molecular beam epitaxy

PLD- Pulsed laser deposition

IBD- Ion beam deposition

UHV- Ultra high vacuum

RF- Radio frequency

HiTUS- High target utilisation sputtering

List of Symbols

$\mathbf{H_D}$- Demagnetising field

N_D- Demagnetising factor

$\mathbf{M}$- Magnetisation

M_S- Saturation magnetisation

K- Anisotropy constant

E_K-Anisotropy energy

V- Volume

U- Potential energy

J_{ex}- Exchange integral

$\mathbf{S}$- Spin

m- Magnetic moment

h_g- Intergranular exchange coupling

A_{grain}- Effective exchange energy between neighbouring grains

c_g- distance between the centres of neighbouring grains

$\mathbf{H}$- Magnetic Field

E_{ms}- Magnetostatic energy

D_T- Domain thickness

E_{ex}- Exchange energy

A_{es}- Exchange stiffness

n_A- Atoms per unit cell

L_P- Lattice parameter

T_N- Néel temperature

H^*- Exchange field

H_K^*-Pseudo anisotropy field

BCC- Body centred cubic

FCC- Face centred cubic

τ –Relaxation time

f_0- Attempt frequency

k_B- Boltzmann constant

H_K- Anisotropy field

S- Magnetic viscosity

P- Order of the antiferromagnet

P_S- Saturation value of the order of the antiferromagnet

E_C- Critical Energy

H_{EX}- Exchange field

V_{SET}- Largest grain volume which can be set

V_C- Volume for the smallest stable grain

T_{SET}- Setting temperature

t_{SET}- Setting time

T_{meas}- Measurement temperature

t_{meas}- Measurement time

T_{ACT}-Activation temperature

t_{ACT}- Activation time

C*- Interfacial coupling constant

T_{NA}- Temperature of non-activation

T_B- Blocking temperature

V_m- Mean grain volume

R_{dep}- Deposition rate

W_0- number of sputtered particles

t_{res}- Resist thickness

ω- Substrate rotation speed

D_e- Dose

Q- Charge density

t_{exp}- Exposure time

A_{exp}- Exposed area

β_s- Source brightness

λ_e- Wavelength of incident electrons

υ – Electron velocity

B- Magnetic flux density

D_m- Mean grain diameter

φ- Magnetic flux

L_{ex}- Exchange length

H_C- Coercive field

t_F- Ferromagnet thickness

References

[1] M. Hayashi, L. Thomas, R. Moriya, C. Rettner, and S. S. P. Parkin, Science **320**, 209 (2008).
[2] S. S. P. Parkin, M. Hayashi, and L. Thomas, Science **320**, 190 (2008).
[3] http://www.seagate.com/gb/en/about-seagate/seagate-history/.
[4] S. S. P. Parkin, Scientific American **300**, 76 (2009).
[5] http://www.seagate.com/gb/en/internal-hard-drives/enterprise-hard-drives/hdd/enterprise-performance-15k-hdd/.
[6] Y. T. Chiu, IEEE Spectrum **49**, 11 (2012).
[7] http://www.explainthatstuff.com/flashmemory.html.
[8] http://www.ts.avnet.com/uk/.
[9] M. Yamanouchi, D. Chiba, F. Matsukura, and H. Ohno, Nature **428**, 539 (2004).
[10] W. H. Meiklejohn and C. P. Bean, Physical Review **102**, 1413 (1956).
[11] J. Sort, V. Langlais, S. Doppiu, B. Dieny, S. Surinach, J. S. Munoz, M. D. Baro, C. Laurent, and J. Nogues, Nanotechnology **15**, S211, Pii s0957-4484(04)69051-9 (2004).
[12] H. Brown, E. D. Dahlberg, and C. Hou, Journal of Applied Physics **89**, 7543 (2001).
[13] K. O'Grady, L. E. Fernandez-Outon, and G. Vallejo-Fernandez, Journal of Magnetism and Magnetic Materials **322**, 883 (2010).
[14] L. Wee, R. L. Stamps, L. Malkinski, and Z. Celinski, Physical Review B **69**, 134426 (2004).
[15] L. Wee, R. L. Stamps, L. Malkinski, Z. Celinski, and D. Skrzypek, Physical Review B **69**, 134425 (2004).
[16] J. Keller, P. Miltenyi, B. Beschoten, G. Guntherodt, U. Nowak, and K. D. Usadel, Physical Review B **66**, 014431 (2002).
[17] M. T. Sarah, Journal of Physics D: Applied Physics **41**, 093001 (2008).
[18] G. Binasch, P. Grünberg, F. Saurenbach, and W. Zinn, Physical Review B **39**, 4828 (1989).
[19] M. N. Baibich, J. M. Broto, A. Fert, F. N. Van Dau, F. Petroff, P. Etienne, G. Creuzet, A. Friederich, and J. Chazelas, Physical review letters **61**, 2472 (1988).
[20] J. R. Childress and R. E. Fontana, Comptes Rendus Physique **6**, 997 (2005).
[21] J. M. Hu, Z. Li, L. Q. Chen, and C. W. Nan, Nature Communications **2**, 553 (2011).
[22] https://www.micron.com/products/dram/ddr4-sdram.
[23] http://www.hitachi.com/corporate/about/history/2001.html.
[24] Timeline: 50 Years of Hard Drives, http://www.pcworld.com/article/127105/article.html (Accessed Sep 13 2006).
[25] NAND Flash Technology and Solid State Drives (SSDs), https://www.kingston.com/en/community/articledetail/articleid/29541?Title=NAND%20Flash%20Technology%20and%20Solid%20State%20Drives%20(SSDs).
[26] VERSASTACK + IBM FLASHSYSTEM =UNPARALLELED VALUE, http://www-01.ibm.com/common/ssi/cgi-bin/ssialias?subtype=WH&infotype=SA&htmlfid=TSL03235USEN&attachment=TSL03235USEN.PDF.
[27] Freescale's MRAM–a new kind of memory chip, http://www.nxp.com/files/microcontrollers/doc/train_ref_material/MRAMWC.pdf.
[28] https://www.everspin.com/file/965/download.

[29] C. Chappert, A. Fert, and F. N. Van Dau, Nat Mater **6**, 813 (2007).
[30] H. Numata, T. Suzuki, N. Ohshima, S. Fukami, K. Nagahara, N. Ishiwata, N. Kasai, and P. Japan Soc Appl, *Scalable cell technology utilizing domain wall motion for high-speed MRAM* 2007), 2007 Symposium on VLSI Technology, Digest of Technical Papers.
[31] S. Fukami *et al.*, 2009 Symposium on Vlsi Technology, Digest of Technical Papers, 230 (2009).
[32] N. F. Mott, Proceedings of the Royal Society of London A: Mathematical, Physical and Engineering Sciences **153**, 699 (1936).
[33] B. Kaeswurm, University of York, 2011 PhD Thesis.
[34] A. Hirohata and K. Takanashi, Journal of Physics D-Applied Physics **47**, 193001 (2014).
[35] S. S. P. Parkin, Physical Review Letters **67**, 3598 (1991).
[36] A. Hirohata, J. Sagar, L. Lari, L. R. Fleet, and V. K. Lazarov, Applied Physics a-Materials Science & Processing **111**, 423 (2013).
[37] M. Julliere, Physics letters a **54**, 225 (1975).
[38] S. Maekawa and U. Gafvert, IEEE Transactions on Magnetics **18**, 707 (1982).
[39] T. Miyazaki and N. Tezuka, Journal of Magnetism and Magnetic Materials **139**, L231 (1995).
[40] S. Yuasa, T. Nagahama, A. Fukushima, Y. Suzuki, and K. Ando, Nat Mater **3**, 868 (2004).
[41] S. S. P. Parkin, C. Kaiser, A. Panchula, P. M. Rice, B. Hughes, M. Samant, and S.-H. Yang, Nat Mater **3**, 862 (2004).
[42] J. Bass, Journal of Magnetism and Magnetic Materials **408**, 244 (2016).
[43] S. Parkin and S.-H. Yang, Nature nanotechnology **10**, 195 (2015).
[44] L. Thomas, R. Moriya, C. Rettner, and S. S. P. Parkin, Science **330**, 1810 (2010).
[45] M. Hayashi, L. Thomas, R. Moriya, C. Rettner, and S. S. Parkin, Science **320**, 209 (2008).
[46] M. T. Hayashi, L ; Rettner, C ; Moriya, R ; Bazaliy, YB ; Parkin, SSP, Physical review letters **98**, 037204 (2007).
[47] V. Vlaminck and M. Bailleul, Science **322**, 410 (2008).
[48] D. Chiba *et al.*, Applied Physics Express **3** (2010).
[49] L. Thomas *et al.*, 2011 IEEE International Electron Devices Meeting (Iedm) (2011).
[50] I. M. Miron *et al.*, Nature Materials **10**, 419 (2011).
[51] K. S. Ryu, L. Thomas, S. H. Yang, and S. Parkin, Nature nanotechnology **8**, 527 (2013).
[52] S. H. Yang, K. S. Ryu, and S. Parkin, Nature nanotechnology **10**, 221 (2015).
[53] A. Yamaguchi, T. Ono, S. Nasu, K. Miyake, K. Mibu, and T. Shinjo, Physical review letters **92**, 077205 (2004).
[54] S. S. P. Parkin, (Google Patents, 2005).
[55] E. R. Lewis, D. Petit, L. O'Brien, A. Fernandez-Pacheco, J. Sampaio, A. V. Jausovec, H. T. Zeng, D. E. Read, and R. P. Cowburn, Nature Materials **9**, 980 (2010).
[56] K. O'Grady, G. V. Fernandez, and A. Hirohata, (Google Patents, 2014).
[57] M. Vopsaroiu, G. V. Fernandez, M. J. Thwaites, J. Anguita, P. J. Grundy, and K. O'Grady, Journal of Physics D-Applied Physics **38**, 490 (2005).
[58] H. S. Jung, W. D. Doyle, and S. Matsunuma, Journal of Applied Physics **93**, 6462 (2003).
[59] K. O'Grady, 2016).
[60] B. D. Cullity and C. D. Graham, *Introduction to magnetic materials* (John Wiley & Sons, 2011).
[61] H. S. Jung, W. D. Doyle, J. E. Wittig, J. F. Al-Sharab, and J. Bentley, Applied Physics Letters **81**, 2415 (2002).
[62] W. Heisenberg, Zeitschrift Fur Physik **49**, 619 (1928).

[63] R. C. O'handley, *Modern magnetic materials* (Wiley, 2000).
[64] M. A. Ruderman and C. Kittel, Physical Review **96**, 99 (1954).
[65] E. D. Daniel, and C. D. Mee, *Magnetic Recording Technology* (McGraw-Hill, New York ; London, 1996), 2nd ed. edn.
[66] M. Futamoto, N. Inaba, Y. Hirayama, K. Ito, and Y. Honda, in *Symposium L on Materials for High-Density Magnetic Recording / Symposium M on Integrated Magneto-Optics at the MRS Spring Meeting*San Francisco, Ca, 1998), pp. 243.
[67] J. G. Zhu and H. N. Bertram, Journal of Applied Physics **66**, 1291 (1989).
[68] E. Fulcomer and S. H. Charap, Journal of Applied Physics **43**, 4190 (1972).
[69] P. Weiss, J. de Phys. et Rad **6**, 661 (1907).
[70] S. Iwasaki and K. Ouchi, IEEE Transactions on Magnetics **14**, 849 (1978).
[71] R. F. C. Marques, P. R. Abernethy, J. A. D. Matthew, C. O. Paiva-Santosa, L. Perazolli, M. Jafelicci, and S. M. Thompson, Journal of Magnetism and Magnetic Materials **272**, 1740 (2004).
[72] P. Grunberg, 1989).
[73] R. Carpenter, University of York, 2015.
[74] A. Kohn, A. Kovacs, R. Fan, G. J. McIntyre, R. C. C. Ward, and J. P. Goff, Scientific Reports **3**, 2412 (2013).
[75] I. Tomeno, H. N. Fuke, H. Iwasaki, M. Sahashi, and Y. Tsunoda, Journal of Applied Physics **86**, 3853 (1999).
[76] M. Tsunoda, K. Imakita, M. Naka, and M. Takahashi, Journal of Magnetism and Magnetic Materials **304**, 55 (2006).
[77] N. P. Aley and K. O'Grady, Journal of Applied Physics **109**, 07d719 (2011).
[78] A. E. Berkowitz and K. Takano, Journal of Magnetism and Magnetic Materials **200**, 552 (1999).
[79] J. Sagar, University of York, 2013.
[80] T. Ambrose, R. L. Sommer, and C. L. Chien, Physical Review B **56**, 83 (1997).
[81] L. E. Fernandez-Outon, K. O'Grady, and M. J. Carey, Journal of Applied Physics **95**, 6852 (2004).
[82] G. Vallejo-Fernandez, L. E. Fernandez-Outon, and K. O'Grady, Applied Physics Letters **91**, 212503 (2007).
[83] G. Anderson, Y. M. Huai, and L. Miloslawsky, Journal of Applied Physics **87**, 6989 (2000).
[84] N. P. Aley, G. Vallejo-Fernandez, R. Kroeger, B. Lafferty, J. Agnew, Y. Lu, and K. O'Grady, IEEE Transactions on Magnetics **44**, 2820 (2008).
[85] N. P. Aley, R. Kroeger, B. Lafferty, J. Agnew, Y. Lu, and K. O'Grady, IEEE Transactions on Magnetics **45**, 3869 (2009).
[86] N. P. Aley, M. Bowes, R. Kroger, and K. O'Grady, Journal of Applied Physics **107**, 09d722 (2010).
[87] N. P. Aley, C. Bonet, B. Lafferty, and K. O'Grady, IEEE Transactions on Magnetics **45**, 3858 (2009).
[88] W. F. Brown, Physical Review **130**, 1677 (1963).
[89] L. Néel, Annales de Géophysique **5**, 99 (1949).
[90] D. P. E. Dickson, N. M. K. Reid, C. Hunt, H. D. Williams, M. Elhilo, and K. Ogrady, Journal of Magnetism and Magnetic Materials **125**, 345 (1993).
[91] P. Gaunt, Journal of Applied Physics **59**, 4129 (1986).
[92] M. Elhilo, K. Ogrady, and R. W. Chantrell, Journal of Magnetism and Magnetic Materials **109**, L164 (1992).

[93] R. V. Chamberlin, G. Mozurkewich, and R. Orbach, Physical review letters **53**, 1025 (1984).
[94] R. V. Chamberlin, G. Mozurkewich, and R. Orbach, Physical review letters **52**, 867 (1984).
[95] T. Hughes, H. Laidler, and K. O'Grady, Journal of Applied Physics **89**, 5585 (2001).
[96] G. Vallejo-Fernandez, N. P. Aley, L. E. Fernandez-Outon, and K. O'Grady, Journal of Applied Physics **104**, 033906 (2008).
[97] R. A. Buhrman and C. G. Granqvist, Bulletin of the American Physical Society **21**, 229 (1976).
[98] G. Vallejo-Fernandez, B. Kaeswurm, L. E. Fernandez-Outon, and K. O'Grady, IEEE Transactions on Magnetics **44**, 2835 (2008).
[99] M. Pakala, Y. Huai, G. Anderson, and L. Miloslavsky, Journal of Applied Physics **87**, 6653 (2000).
[100] H. Uyama, Y. Otani, K. Fukamichi, O. Kitakami, Y. Shimada, and J. I. Echigoya, Applied Physics Letters **71**, 1258 (1997).
[101] G. Vallejo-Fernandez, L. E. Fernandez-Outon, and K. O'Grady, Journal of Physics D: Applied Physics **41**, 112001 (2008).
[102] M. N. R. Ashfold, F. Claeyssens, G. M. Fuge, and S. J. Henley, Chemical Society Reviews **33**, 23 (2004).
[103] K. Wasa, *Handbook of Sputter Deposition Technology* 2012), 2nd edn.
[104] P. J. Hockley and M. Thwaites, (Google Patents, 2009).
[105] M. J. Thwaites, (Google Patents, 2002).
[106] M. Lederman, IEEE Transactions on Magnetics **35**, 794 (1999).
[107] H. N. Fuke, K. Saito, Y. Kamiguchi, H. Iwasaki, and M. Sahashi, Journal of Applied Physics **81**, 4004 (1997).
[108] R. M. Bozorth, *Ferromagnetism* (Wiley, 1993).
[109] M. J. Madou, *Fundamentalks of Microfabrication and Nanotechnology: Volume 2* (CRC Press, 2012), 3 edn., Vol. 2.
[110] K. S. a. B. W. Smith, *Microlithography-Science and Technology* (CRC Press, 2007), 2 edn.
[111] P. J. G. D. Chescoe, *The Operation of the Transmission and Scanning Electron Microscopes* (oxford University Press, 1990), 1 edn.
[112] C. B. C. D. B. Williams, *Transmission Electron Microscopy: A textbook for Materials Science* (Springer Science & Business Media, 2013).
[113] Introduction to Electron Microscopes, http://www.materials.ac.uk/elearning/matter/introductiontoelectronmicroscopes/tem/introduction.html/.
[114] Introduction to Scanning Electron Microscopes, http://www4.nau.edu/microanalysis/microprobe-sem/instrumentation.html/.
[115] C. G. Granqvist and R. A. Buhrman, Journal of Applied Physics **47**, 2200 (1976).
[116] G. R. Jones, M. Jackson, and K. O'Grady, Journal of Magnetism and Magnetic Materials **193**, 75 (1999).
[117] P. J. Flanders, Journal of Applied Physics **63**, 3940 (1988).
[118] K. O'Grady, V. G. Lewis, and D. P. E. Dickson, Journal of Applied Physics **73**, 5608 (1993).
[119] K. Ogrady, R. W. Chantrell, and I. L. Sanders, IEEE Transactions on Magnetics **29**, 286 (1993).

[120] E. O. Samwel, T. Bolhuis, and J. C. Lodder, Review of Scientific Instruments **69**, 3204 (1998).
[121] J. Nogues and I. K. Schuller, Journal of Magnetism and Magnetic Materials **192**, 203 (1999).
[122] J. Kerr, Philos. Mag. **5**, 161 (1878).
[123] J. Kerr, Philos. Mag. **3**, 321 (1877).
[124] P. Weinberger, Philosophical Magazine Letters **88**, 897, Pii 905064790 (2008).
[125] Z. Q. Qiu and S. D. Bader, Review of Scientific Instruments **71**, 1243 (2000).
[126] P. N. Argyres, Physical Review **97**, 334 (1955).
[127] M. Vopsaroiu, M. Georgieva, P. J. Grundy, G. V. Fernandez, S. Manzoor, M. J. Thwaites, and K. O'Grady, Journal of Applied Physics **97**, 10n303 (2005).
[128] Z. Y. Zhu, Y. C. Cheng, and U. Schwingenschlogl, Physical Review B **85**, 235401 (2012).
[129] G. Vallejo-Fernandez, T. Dimopoulos, M. Ruehrig, and K. O'Grady, Journal of Magnetism and Magnetic Materials **310**, E769 (2007).
[130] S. U. Jen, Y. D. Yao, Y. T. Chen, J. M. Wu, C. C. Lee, T. L. Tsai, and Y. C. Chang, Journal of Applied Physics **99**, 053701 (2006).
[131] M. Vopsaroiu, K. O'Grady, M. T. Georgieva, P. J. Grundy, and M. J. Thwaites, IEEE Transactions on Magnetics **41**, 3253 (2005).
[132] P. J. Grundy, Journal of Magnetism and Magnetic Materials **21**, 1 (1980).
[133] W. N. Yu, J. A. Bain, Y. G. Peng, and D. E. Laughlin, IEEE Transactions on Magnetics **38**, 3030 (2002).
[134] E. H. Frei, S. Shtrikman, and D. Treves, Physical Review **106**, 446 (1957).
[135] G. S. Abo, Y. K. Hong, J. Park, J. Lee, W. Lee, and B. C. Choi, IEEE Transactions on Magnetics **49**, 4937 (2013).
[136] A. Yamaguchi, K. Yano, H. Tanigawa, S. Kasai, and T. Ono, Japanese Journal of Applied Physics **45**, 3850 (2006).
[137] T. Schrefl, J. Fidler, K. J. Kirk, and J. N. Chapman, Journal of Magnetism and Magnetic Materials **175**, 193 (1997).
[138] K. J. Kirk, J. N. Chapman, and C. D. W. Wilkinson, Journal of Applied Physics **85**, 5237 (1999).
[139] R. P. Cowburn, D. A. Allwood, G. Xiong, and M. D. Cooke, Journal of Applied Physics **91**, 6949 (2002).
[140] K. J. Kirk, J. N. Chapman, S. McVitie, P. R. Aitchison, and C. D. W. Wilkinson, Applied Physics Letters **75**, 3683 (1999).
[141] L. K. Bogart, D. Atkinson, K. O'Shea, D. McGrouther, and S. McVitie, Physical Review B **79**, 054414 (2009).
[142] K.-S. Ryu, L. Thomas, S.-H. Yang, and S. Parkin, Nature nanotechnology **8**, 527 (2013).
[143] K.-S. Ryu, L. Thomas, S.-H. Yang, and S. S. P. Parkin, Applied Physics Express **5**, 093006 (2012).
[144] A. J. Annunziata *et al.*, 2011 IEEE International Electron Devices Meeting (Iedm) (2011).
[145] I. Polenciuc, A. J. Vick, D. A. Allwood, T. J. Hayward, G. Vallejo-Fernandez, K. O'Grady, and A. Hirohata, Applied Physics Letters **105**, 162406 (2014).